공학박사 학위논문

Investigation of surface charge effects on biomolecule transport in solid-state nanopores

2019 년 2 월

서울대학교 대학원

재료공학부

김 형 준

INVESTIGATION OF SURFACE CHARGE EFFECTS ON BIOMOLECULE TRANSPORT IN SOLID-STATE NANOPORES

지도 교수: 김 기 범

이 논문을 공학박사 학위논문으로 제출함
2019 년 2 월

서울대학교 대학원
재료공학부
김 형 준

김형준의 공학박사 학위논문을 인준함
2019 년 2 월

위원장	안철희	(인)
부위원장	김기범	(인)
위원	선정윤	(인)
위원	이진석	(인)
위원	지승욱	(인)

Investigation of surface charge effects on biomolecule transport in solid-state nanopores

A DISSERTATION SUBMITTED TO
DEPARTMENT OF MATERIALS SCIENCE AND ENGINEERING
SEOUL NATIONAL UNIVERSITY

FOR THE DEGREE OF
DOCTOR OF PHILOSOPHY

HYUNG–JUN KIM

February 2019

ABSTRACT

INVESTIRATION OF SURFACE CHARGE EFFECTS ON BIOMOLECULE TRANSPORT IN SOLID−STATE NANOPORES

Hyung-Jun Kim
Department of Materials Science and Engineering
The Graduate School
Seoul National University

Nanopores have emerged as a biomolecule sensing platform for label-free detection with single molecule accuracy. Here, molecules that translocate through a nanometer-size holes in a thin membrane can be detected by measurable changes in ion current, which can be associated with the structural features of molecules, such as physical size and charge state. Traditionally, nanopore research has been divided into two areas: (1) biological nanopore using pore-forming protein, embedded in a lipid bilayer membrane, such as alpha-hemolysin and MspA, (2) solid-state nanopore employing fabrication technologies such as electron beam drilling of thin membranes or laser assisted pulling of glass capillaries. The biological nanopores are attracting much attention in the field of DNA sequencing because of their relatively high sensitivity from the fixed dimension of 1.4 nm. In contrast to biological nanopore, solid-state nanopore is better suited for wide range of analytes, for instances, dsDNA, proteins, and DNA-protein complexes, based on its

advantages of mechanical and chemical durability, flexibility in the pore size. Currently, a key issue for advancing solid-state nanopore technology is a sensitivity issue and a translocation behavior issue. In this dissertation, surface charge characteristics of nanopore have been utilized to control and optimize the translocation behavior of molecule, such as, capture, transport, and clogging. The surface charge of nanopore could affect translocation behavior through electro-osmotic flow or electrostatic interaction, and the previous studies that have been conducted in this point of view are summarized in chapter 2. In addition, the strategies used in this dissertation to modify the surface charge of nanopore were discussed.

In chapter 3, surface charge induced by light illumination in silicon nitride nanopore and the influence on DNA translocation were investigated. In order to detect the DNA translocation with sufficient signal-to-noise ratio, the strong increase of ionic noise upon laser illumination in commonly used Si substrate based nanopore had to be solved. At first, we analyzed the noise characteristics of Si substrate and glass substrate based nanopore, and suggested that the origin of noise is photo-reduction of hydrogen at the Si/electrolyte interfaces. The increase of negative surface charge as a function of laser power in the glass substrate based nanopore was calculated from ion current. The electro-osmotic flow, which is generated in the direction opposite to the direction of DNA translocation, reduced the capture frequency, but had no influence on the translocation speed. In addition, we proposed a platform device using a low-noise glass substrate and metal-integrated membrane, and demonstrated the synchronized optical and electronic detection of fluorescence labelled DNA with high signal-to-noise ratio. Our low noise nanopore platform is of great value in combine the advantages of both detection methods and in further confirming the molecule translocation.

In chapter 4, polyurea nanopore was fabricated by using molecular layer deposition, and the translocation behavior of DNA and protein was

investigated. The polyurea membrane was chosen due to its high mechanical stability and chemical resistance, which is responsible for reducing the pore volume of several-nanometers in all dimensions. Furthermore, the polyurea nanopore exhibited a high negative surface charge density more than four times that of the conventional silicon nitride nanopore. A highly developed electro-osmotic flow in polyurea nanopore resulted in the inhibition of electrophoretic capture of negatively charged DNA, and the increase of electrophoretic capture of positively charged MDM2 protein. The translocation speed of biomolecules was not affected by electro-osmotic flow, but rather the enhanced electrostatic interaction slows down the MDM2.

In this dissertation, we discuss the surface charge effect on biomolecule transport in nanopore. We have shown that the electro-osmotic flow is the major driving force for capture of biomolecules, and the influence of electrostatic interaction on protein translocation for the first time. We have suggested that the use of nanopore, which exhibit opposite charge to that of the analyte, could improve the detection efficiency in the following aspects: 1) by increasing the capture frequency, the analysis efficiency and throughput are enhanced, 2) by slowing down the translocation speed, the required temporal resolution is lowered.

Keyword : nanopore sensing, solid-state nanopore, single molecule sensing, surface charge, electro-osmotic flow, optical detection, polyurea

Student Number : 2012-24159

Table of Contents

LIST OF TABLES

LIST OF FIGURES

Chapter 1

Figure 1-5 Diagnosis: detection of SNPs. (a) Schematics of experimental scheme; identifying the symmetric/asymmetric binding location of ZFP in DNA by additional current drop in blockade current. (b) Position of additional current drop indicates location (symmetric/asymmetric) of binding site.

Figure 1-6 Drug screening: detection of PPI. (a) Schematics of experimental scheme; identifying the binding of MDM2/GST-p53TAD and detaching by drug molecule (Nutlin-3) through event frequency. (b) Traces of ion current versus time indicate that the low event frequency is caused by molecular binding.

Figure 1-7 Functionalization of molecular specific sensing. (a) Sketch of experimental scheme. (b) Schematics of interaction between His-tagged protein and Ni-NTA receptor on SC15EG3/gold-coated SiN nanopore (c) Trace of current versus time indicates the stochastic sensing of protein. Adapted from Ref. 14.

Figure 1-8 Biomimetic functionalized nanopore. (a) Schematics of opening and closing of nanopore by external stimuli using K^+ ion and G4 DNA. (b) Current-concentration properties of functionalized nanopore before G4 DNA modification (blue), after G4 DNA modification (red), addition of the complementary DNA strands.

Figure 1-9 Biological nanopores and strategy for DNA sequencing. (a) The geometry of representative biological nanopores α-haemolysin and MspA. (b) Schematics of nanopore sequencing using lipid-embedded MspA with ssDNA bound to the motor enzyme (polymerase). Adapted from refs. 28 and 33.

Figure 1-10 Fabrication of solid-state nanopores in Si-based membranes. (a) Ion-beam sculpting method developed by the Golovchenko group at Harvard

University and TEM image of nanopore. (b) A focused electron-beam method developed by the Dekker group at Delft and TEM image of nanopore. Adapted from refs. 34 and 1.

Figure 1-11 Noise on solid-state nanopore. (a) Noise analysis with fitting on power spectral density. The flicker, thermal, dielectric, and amplifier noise sources exhibit different dependencies on frequency. (b) Current traces for noise comparison between Si-based and Pyrex-based nanopores. PSD curves corresponding to current traces show the reduced dielectric noise in Pyrex-based nanopore. Adapted from ref. 45.

Figure 1-12 Spatial resolution and signal-to-noise ratio. (a) Comparison of the dimensions of α-haemolysin, MspA, SiN (solid-state), and graphene nanopores. The MspA and graphene nanopore exhibit excellent spatial resolution comparable to the base-pair interval of DNA. (b) Ion current traces for 40 nt ssDNA translocation shows the membrane thickness effect on signal-to-noise ratio. Adapted from refs. 48 and 45.

Figure 1-13 Temporal resolution and signal-to-noise ratio. (a) Signal-to-noise ratio as a function of measurement bandwidth for two nanopores using low-noise-amplifier system (CNP). (b) Maximum bandwidth defined by minimum signal-to-noise ratio of 5 as a function of amplitudes of blockade current. Adapted from ref. 52.

Figure 1-14 Translocation behavior to be controlled in nanopore sensing. (a) Capture of molecules on the nanopore and the capture signal on the current trace. (b) Molecular translocation speed required for temporal resolution of the measurement system; examples of too fast event (red) and sufficiently slow event (black) in current trace. (c) Clogging of molecule to nanopore and the clogging signal on the current trace.

Chapter 2

Figure 2-1 Electro-osmotic flow. The electrophoretic drift of positive ions in the diffuse part of electric double layer produces drag on the fluid and hence an electro-osmotic flow.

Figure 2-2 Control of DNA motion by electro-osmotic flow. Schematics of gate manipulation of DNA capture and transport with ion-current feedback system. Anionic electro-osmotic flow enhances the DNA capture and thus alters cationic electro-osmotic flow so as to slow down DNA transport. Adapted from ref. 2.

Figure 2-3 Electrostatic retardation of DNA transport in field-effect transistor. (a) Slowing of DNA transport with +0.5 V gate bias and dwell time distribution indicates events with electrostatic interaction with pore surface. (b), (c) Increase of mean dwell time with increase of positive gate voltage. Adapted from refs. 18, 16 and 7.

Figure 2-4 Driving and drag forces on DNA with electrostatic interaction. (a) The surface frictional force from electrostatic interaction between DNA and pore (F_{in}), hydrodynamic drag force (F_{drag}) and electrophoretic driving force (F_{el}) (b) experimentally extracted friction coefficient of electrostatic interaction between DNA and positively charged ZnO nanopore. Adapted from ref. 12.

Figure 2-5 Optoelectronic control of surface charge in nanopores. (a) Schematics of light-induced modulation of ion current and DNA translocation. (b) Ion current enhancement as a function of laser power. (c) Retardation factor (RF) indicating the reduction in dwell time as a function of laser power.

Figure 2-6 Relationship between surface charge and hydrophilicity. (a) The zeta potential of SiO_2 as a function of pH and (b) the contact angle at the corresponding pH. (c) The zeta potential of Teflon as a function of pH and (d) the contact angle at the corresponding pH. Adapted from refs. 19, 20 and 21.

Figure 2-7 Surface charge characteristic of polyurea. The zeta potential as a function of pH for polyurea of various structures, compositions and end groups. Adapted from ref. 33.

Chapter 3

Figure 3-1. Schematics of (a) Si and (b) Pyrex substrate based silicon nitride nanopore platforms. (c) Optical image of a Pyrex substrate (Py-SiN_x) platform (scale bar = 10 µm). Two circular features are present. The larger feature (diameter: ~19 µm) corresponds to the aperture within the pyrex substrate and the smaller feature (diameter: ~2.1 µm) to the free standing silicon nitride membrane. (d) TEM image of a 7 nm diameter nanopore within the free-standing silicon nitride membrane of a Py-SiN_x platform (scale bar = 10 nm).

Figure 3-2. The experimental set-up: an epifluorescence optical configuration employing a 488 nm continuous-wave laser; a 60x water immersion objective (Obj.) and avalanche photodiode (APD) is used to probe a SiN_x nanopore (Materials and Methods). When electrical data acquisition is initiated, a TTL pulse is generated by the electrical data acquisition (DAQ) card which subsequently triggers optical acquisition.

Figure 3-3. (a) Baseline ionic current at 0 mV, under laser illumination, for a ~27 nm diameter nanopore in a Si-SiN_x (yellow background) and Py-SiN_x

platform. Different colour traces correspond to different laser powers, as indicated by the number (in µW units) beneath each trace. The inset is an expanded view of data for the Py-SiN$_x$ device. (b) Power Spectral Densities at 0mV for the Si-SiN$_x$ platform with the laser off (blue) and at ~578 µW laser power (red). (c) Power Spectral Densities at 0mV for the Py-SiN$_x$ platform with the laser off (blue) and at ~583 µW laser power (red).

Figure 3-4. Standard deviation of ionic current as a function of laser power, at 0 mV bias, for a ~27 nm diameter nanopore within a A) Si-SiN (conductance: 25.4 nS) and B) Py-SiN platform (conductance: 25.5 nS). Data collected using a 0.1M KCl, 10mM Tris.HCl, 1mM EDTA (pH 7) buffer.

Figure 1-5. (a) Current–Voltage trace for a ~7 nm diameter (conductance: 4.0 nS at 0 mV) Py-SiN$_x$ nanopore with the laser off (blue) and at ~17 µW (blue), ~201 µW (orange) and ~596 µW (red) power. The inset shows pore conductance at 0 mV as a function of laser power. (b) Standard deviation of ionic current versus laser power with a bias of 0mV (blue), -100mV (green) and -200mV (red).

Figure 3-6. The relative reduction in translocation frequency of 5 kbp DNA at ~74 µW (O) and ~204 µW (Δ) laser power, w.r.t. the translocation frequency with the laser off. Fits reveal an average reduction of 25.8 ± 1.5% and 60.4 ± 5.6% at ~74 µW and ~204 µW laser power respectively. Data collected using a ~7 nm diameter pore (conductance: 4.0 nS at 0 mV) and a 0.1M KCl, 10mM Tris.HCl, 1mM EDTA (pH 7) buffer.

Fig. 3-7 Power Spectral Densities at 0 mV (blue) & -200mV (red) with the laser power at ~596 µW. Black lines indicate fits of $S(f) = Af^{\alpha-}$ and $S(f) = B + Cf + Df^2$ (where A–D are fitting parameters and $0 < \alpha < 2$, with exponent α typically close to 1) for data collected at -200mV and 0mV respectively.

Figure 3-8. Dependence of (a) Thermal and (b) Flicker noise on laser power. The inset of panel (a) shows pore conductance at 0 mV and (b) the normalised flicker noise amplitude (w.r.t. $<I>^2$) as a function of laser power. Data collected using a ~7 nm diameter pore (conductance: 4.0 nS at 0 mV) and 0.1M KCl, 10mM Tris.HCl, 1mM EDTA (pH 7) buffer.

Figure 3-9. Dependence of dielectric and input capacitance noise on laser power. The average amplitude of dielectric noise and input capacitance noise are $2.22\times10^{-14} \pm 1.14\times10^{-20}$ and $9.51\times10^{-8} \pm 1.75\times10^{-9}$ respectively. The data was collected using an ~10 nm diameter pore (conductance: 6.8 nS), 0.1M KCl, 10mM Tris.HCl, 1mM EDTA (pH 7) buffer and was low pass filtered at 20 kHz.

Figure 3-10. Power spectral densities at -200 mV, normalised with respect to the square of the ionic current, for a ~27 nm diameter nanopore in a Si-SiN_x and Py-SiN_x platform. (a) Power Spectral Densities for the Si-SiN_x platform with the laser off (blue) and at ~578 μW power (red). (b) Power spectral densities for the Py-SiN_x platform with the laser off (blue) and at ~583 μW power (red).

Figure 3-11. (a) Baseline-adjusted ionic current trace for electrical 5 kbp DNA translocation detection at 100 mV using a ~19 nm diameter pore (conductance: 49.6 nS) and 1M KCl electrolyte. (b) Corresponding contour plot of event amplitude versus duration for 100 mV electrical detection data. (c) Photon trace (0.5 ms resolution) for optical Yoyo® -1 labelled 5 kbp DNA (7.5bp’s : 1 dye) translocation detection at 300 mV bias and ~17 μW laser power using a 30 nm diameter pore (conductance: 25.7 nS) and 0.1 M KCl electrolyte. Data corresponds to 500-580 nm wavelength fluorescence. (d) Corresponding contour plot of event amplitude (photons per 0.5ms) versus duration for 300 mV optical detection data.

Figure 3-12. (a) The top and bottom trace correspond to ionic current and photon counts within the red channel of the optical set-up (λ~ 640- 800 nm) at -200 mV bias respectively. Electrical data was sampled at 100 kHz and low pass filtered to 10 kHz, whilst optical data was sampled at 100 kHz. Increases in the magnitude of both signals correspond to illumination of the pore with a 1.87 mW, 488 nm wavelength laser. (b) Cross-correlation of the data shown in panel A. The electronic signal trailed the optical signal by an average of 0.18 ± 0.02 ms. Data collected using a ~14 nm diameter (conductance: 9.1 nS) nanopore and a 0.1M KCl, 10mM Tris.HCl, 1mM EDTA (pH7) buffer.

Figure 3-13. (a) and (b) Baseline adjusted ionic current and photon trace for Yoyo®-1 labelled 5 kbp DNA (7.5bp's : 1 dye) translocation detection at 400 mV bias and ~17 µW laser power using two pores (~10 nm and 6 nm diameter, total conductance: 9.1 nS) and a 0.1 M KCl electrolyte. Data within the optical channel has been re-binned at 2 ms resolution. (c) Corresponding electrical data histograms of event duration and amplitude (inset) fit with Ling *et al* and Gaussian probability distribution functions, respectively.[48] (d) Corresponding optical data histograms of event duration and amplitude (inset) fit with log-normal probability distribution functions.

Figure 3-14. Cross-correlation of the optical events within the green channel (λ ~ 500- 580 nm) and the associated peaks in ionic current for the data set shown in Panel A and B in Fig. 3-12.

Chapter 4

Figure 4-1. A schematic representation of DNA and MDM2 translocation through polyurea nanopore on a pyrex substrate

Figure 4-2. Schematics diagram of homemade MLD set up, equipped with in situ FTIR spectroscopy and hot wall viscous flow vacuum chamber.

Figure 4-3. (a) Illustration for surface reaction of polyurea film fabricated by molecular layer deposition (MLD). The *p*-phenylenediisocyanate (PDI) and *p*-phenylenediamine (PDA) are alternately bonded on SiO_2 (100) substrate. (b) In-situ FTIR spectra of the SiO_2 substrate after the first and second exposure of PDI and PDA. (c) Thickness profiles of $(PDI/PDA)_n$ polyurea MLD films as a function of the number of MLD cycles using ellipsometry.

Figure 4-4 (a) Fabrication process of polyurea nanopore with pyrex substrate. A 10-nm-thick polyurea is deposited by MLD on SiO_2 substrate. The free-standing polyurea membrane is fabricated by wet-transfer method using PMMA supporting layer and HF-wet etching. (b) TEM image of 2 μm free-standing polyurea membrane with a-Si supporting layer (scale bar: 0.5 μm). (c) TEM images of polyurea nanopores with 5, 7, and 10-nm diameter (scale bar: 10 nm).

Figure 4-5 (a) Two-dimensional AFM image and the height profiles (along with red line in AFM image) of the $(PDI/PDA)_{25}$ polyurea MLD film transferred to a-Si layer on pyrex substrate. The blue arrow indicates the polyurea film and the right is the a-Si layer. The scan area is 10 μm × 10 μm.

Figure 4-6 Ionic current *vs* applied voltage characteristics for (a) polyurea nanopore (h_{eff}=8nm) and (b) SiN nanopore (h_{eff}=9nm) at 1 M KCl electrolyte with TE buffer (pH=8).

Figure 4-7 The experimental conductance value in Fig. 4-6 were fitted with the conductance equation. The conductance of five polyurea nanopores (a) and SiN nanopores (b) were used to characterize the surface charge density at 1 M KCl. The solid line indicates the surface charge density value with 10 mC/m2s intervals. The surface charge of polyurea nanopore is in -51 ± 8 mC/m2 and SiN nanopore is in -14 ± 5 mC/m2.

Figure 4-8 Power spectral densities (PSD) of 7-nm pores at 0 and 100 mV applied voltages in buffered 1 M KCl solution (pH 8.0), filtered at 100 kHz. Each red line results from fitting of the data to: $S = Af^{-\beta} + B + Cf + Df^2$.

Figure 4-8 (a) TEM images of 7 nm polyurea nanopores with 25 nm thick 2μm opening membrane (Top) and 10 nm thick 0.15 μm opening membrane (Bottom) (b) Power spectral densities (PSD) for 3 kinds of 7 nm pores under 100 mV voltages in 1 M KCl electrolyte solution with TE buffer (pH 8.0), filtered at 100kHz. Each line results from fitting of the data to $S = Af^{-\beta} + B + Cf + Df^2$.

Figure 4-9 Ionic current traces with 2nM 1kbp dsDNA in cis-chamber for polyurea nanopore and SiN nanopore at 300 mV applied voltage, filtered at 100 kHz in 1 M KCl with TE buffer (pH 8.0).

Figure 4-10 (a) Continuous 10-s ionic current traces for 1-kbp DNA translocation through polyurea nanopore (Φ 7.2 nm, 8 nm thick) in buffered 2.5 M KCl solution (pH 8.0) at 200 mV (black), 250 mV (red), 300 mV (blue) (scale bar: 1 nA, 2 s). (b) Representative events extracted from the current traces in (a) (scale bar: 1 nA, 0.5 ms). (c) Scatter plots of ΔI *vs* t_D for 1-kbp DNA translocation through Φ 7.2 nm polyurea nanopore in the range V = 200–300 mV. (d) Histograms of ΔI corresponding to panel c in the range V = 200–300 mV. Solid lines indicate the Gaussian distribution fits and the inset shows the mean values of ΔI with respect to applied voltage. The dashed line represents the linear fit of data. (e) Histograms of log t_D in the range V = 200–300 mV. Solid lines indicate the Gaussian distribution fits.

Figure 4-11 (a) I-V plots on a. polyurea nanopore (a, d=8nm, h=9nm) and b. SiN nanopore (d=8nm, h=10nm) at 0.1, 1, 10, 100, 1000, 2000 and 2500 mM KCl electrolyte with TE buffer (pH=8). The experimental conductance value were fitted with the conductance equation. (c, d) The point is experimental conductance and blue line is calculated total conductance, which is a sum of geometry term and surface charge density term. The surface charge of polyurea nanopore (c) is in -50 ± 5 mC/m^2 and SiN nanopore (d) is ranging from -5.2 to -13 mC/m^2 at 0.1mM ~ 2.5 M KCl electrolyte.

Figure 4-12 (a) Continuous 30-s ionic current traces for 100 nM MDM2 translocation at –100, –125, and –150 mV voltage through polyurea nanopore (Φ 10 nm, 8 nm thick) and SiN nanopore (Φ 9.5 nm, 9 nm thick) in buffered 1 M KCl (pH 7.4) (scale bar: 0.5 nA, 2 s). (b) Selected translocation events of MDM2 from (top) 150 mV current trace on SiN and polyurea pores (scale bar: 0.2 nA, 250 μs). (c) Event frequency versus voltage for SiN and polyurea pores. Each event frequency was fitted to y = Ax.

Figure 4-13 (a) Scatter plots of $\Delta I/I_0$ *vs* t_D for MDM2 translocation events over 5 min through polyurea and SiN nanopores in the range V = –100 to –150 mV. Due to the difference in translocation throughput, the number of total events at each applied voltage was 248 (–100 mV), 303 (–125 mV), and 347 (–150 mV) on SiN nanopore and 1096 (–100 mV), 1301 (–125 mV), and

1928 (−150 mV) on polyurea nanopore, respectively. (b) Histograms of t_D in the range $V = -100$ to -150 mV. The data were fitted to a 1D diffusion-drift model. (c) Histograms of $\Delta I/I_0$ in the range $V = -100$ to -150 mV. The data were fitted to Gaussian distribution. The inset shows the mean values of $\Delta I/I_0$ with respect to applied voltage. The dashed line represents the linear fit of data

Figure 4-14 Diffusion coefficients (D) and drift velocities (v) for MDM2 transport through polyurea and SiN nanopore used in Fig. 4-13, obtained from fitting dwell times to 1D diffusion-drift model treating D and v as free parameters.

Chapter 1.

Introduction

1.1 Concept of nanopore sensing

The biological cell contains various types of pores that control the passage of ions and molecules through the cell. This passage involves cellular processes, such as communication between cells or subcellular structures. Examples include the selective ion channels that govern ion flow through the cell surface, the nuclear pore complexes that regulate the passage of messenger RNA from the cell nucleus into the cell cytosol, proteins that are secreted across pores in the membranes of cell organelles, and viruses that dump their genomes into cells via pores in the cell membrane.[1] Inspired by these molecular passages through biological pores and the Coulter counter method, there has been a tremendous amount of recent research into using nanopores as single-molecule sensors.

The principle of nanopore sensing is summarized in Fig. 1-1. A thin membrane containing a nanometer-scale pore is placed between two chambers filled with conductive electrolyte, and a voltage bias is applied across the membrane using two Ag/AgCl electrodes. In this state, a constant current is generated by steady ion flow through the pore, as shown in Fig. 1-1a. The charged biomolecules are then introduced into one chamber and an applied electric field guides the molecules into the pore by electrophoresis. This molecular transport, which partially blocks ion flow through the pore, causes the transient current blockades shown in Fig. 1-1b. These perturbations involve valuable information about the analytes from parameters such as amplitude of current blockades (δI), dwell time (t_d), and the interval between successive events (δt).

The concept of nanopore sensing, which utilizes electrophoretic DNA transport through the nanopores, was first proposed by David Deamer (University of California) in 1989, suggesting that sequences of single-stranded DNA (ssDNA) can be distinguished by the difference in ion-current readout between each base pair.[2] A 1996 study by Kasianowicz (NIST) first showed that transport of biomolecules across a lipid embedded α-haemolysin protein nanopore could actually be detected by ion current drop.[3] The smallest diameter of α-haemolysin pore (~1.5 nm) is slightly larger than the diameters of ssDNA and ribonucleic acid (RNA), allowing the passage of these molecules through the pores. In addition, a distinction between bouncing events and successive translocation events was demonstrated by dwell-time distribution, which differ depending on molecular length (Fig. 1-1). Since the successive detection of molecular passages, nanopore sensing techniques have been studied with a wide range of analytes, such as ions, DNA, RNA, peptides, proteins, synthesized nanoparticles, drug molecules, and their complexes.[4-7]

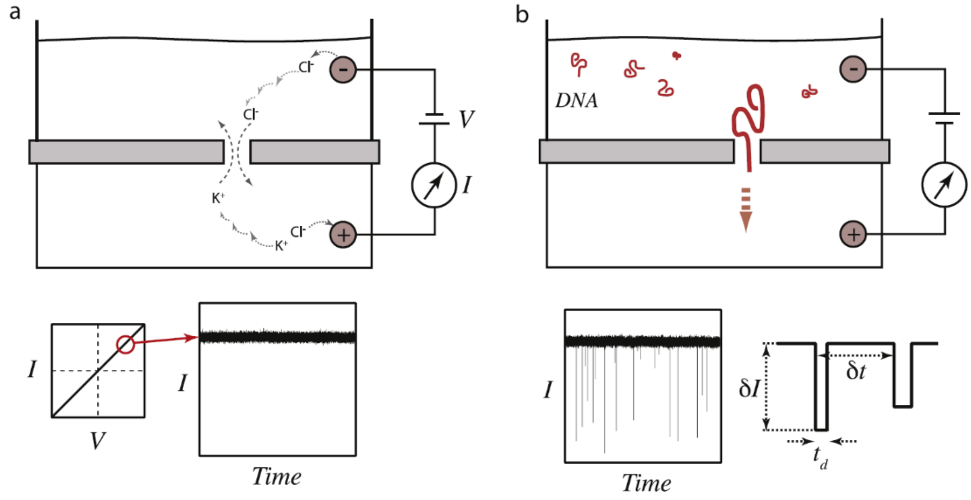

Figure 1-1 The principle of nanopore sensing. (a) The membrane with nanopores divides cis- and trans-chambers containing electrolytes. An ion current flows through the nanopore by applied voltage across the membrane. (b) Translocation of molecules through the nanopores generates transient current blockades. Adapted from ref. 1.

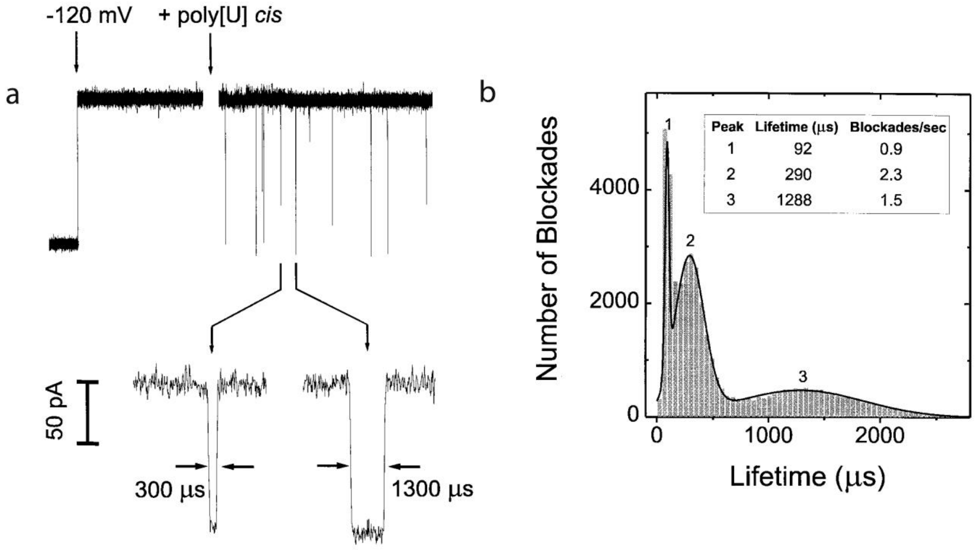

Figure 1-2 The first reports of biomolecule detection using nanopores. (a) Translocation of poly[U] through α-haemolysin pore *s* detected by transient current blockades. (b) The dwell-time distribution of poly[U] shows bouncing events (peak 1) and translocation events (peaks 2, 3). Adapted from ref. 3.

1.2 Applications

1.2.1 DNA sequencing

From the earliest days of nanopore technology, studies of nanopore sensing have focused on the development of next-generation DNA sequencing technology. DNA is composed of four types of nucleotides (adenine, thymine, Guanine, and cytosine) attached to the backbone of phosphate groups and sugars. The genetic information that expresses all known living organisms is coded in the sequence of nucleotides. Thus, the demand for and value of DNA- sequencing techniques continues to increase in such scientific fields as genetics, computational biology, biomedical science, clinical diagnostics and molecular biology.[8] The first successful sequencing technology is the Sanger method, which has been improved and utilized with the advantages including parallelization and automation[9] (Fig. 1-3). However, the limitations in time and cost arising from the short read-lengths of the Sanger method have triggered the need for next generation sequencing technologies. Direct analyses of single DNA molecules has become a next-generation sequencing method because it lacks the time- and cost-consuming PCR amplification and labeling work. Among these, the nanopore technique, involving taking the DNA apart one nucleotide at a time by electrophoretic capture into the pore and detecting the nucleotide sequentially by measuring the ion current, is a prominent candidate.[10] Indeed, in 2014 this scheme was implemented as

‘MiniION’ by Oxford Nanopore Technologies in the United Kingdom. The flow cell of MiniION can analyze long DNA strands (thousands of nucleotides) molecules in parallel by fast electrical reading of its hundreds of nanopores, and the cost of the device is only US$500~900 each.[11] Although the MiniION still needs improvements in accuracy and stability, its advantages have attracted a great deal of attention.

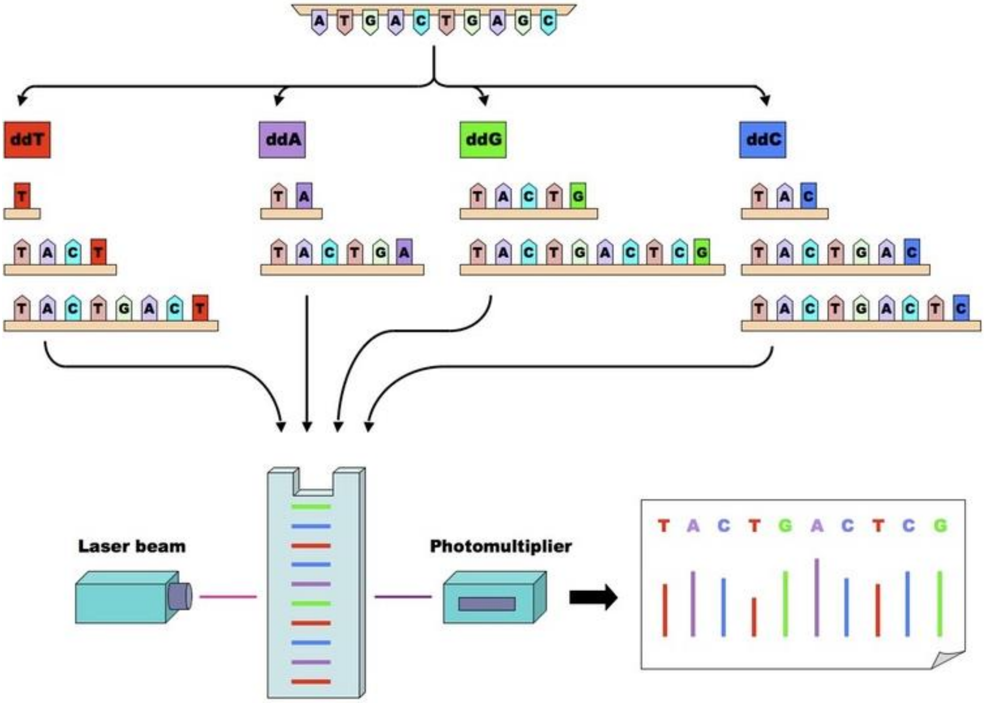

Figure 1-3 Procedure for DNA sequencing based on the Sanger method. At first, PCR amplification is conducted in the presence of fluorescent chain-terminating nucleotides. Labeled fragments are extracted separately through gel electrophoresis. Fluorescent fragments are detected by laser and represented on a chromatogram. Adapted from © www.vce.bioninja.com.au.

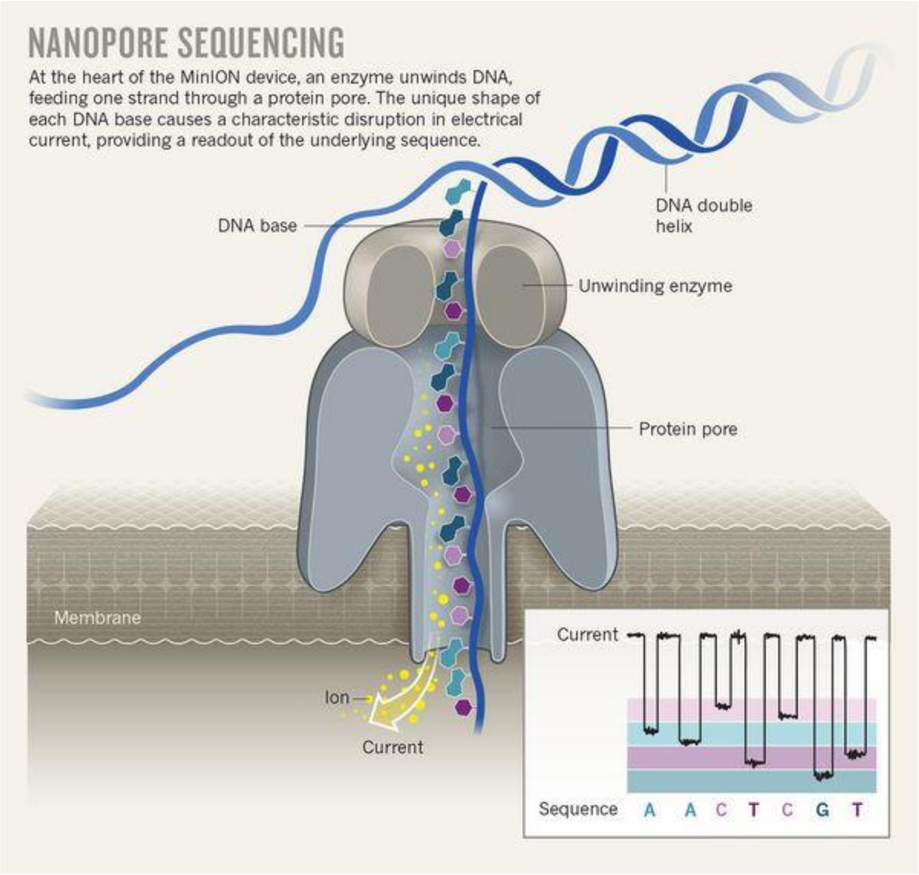

Figure 1-4 In nanopore sequencing the ion current is reduced over time by the differing sizes of each nucleotide in the strand that passes through the pore. From ref. 11.

1.2.2 Biomedical applications

The structural features of biomolecules with biomedical significance can be characterized by nanopore sensing. The diagnostic applications are based on the detection of RNA interference or structural modification in DNA. Studies on RNA interference are closely related to the RNA-mediated diseases and the early diagnosis of cancer by specific RNA sequence, and involve the analysis of RNA/Antibiotic complexes[12] and aptamers.[13] Nanopores have emerged as a valuable tool to detect the local conformational difference in DNA, and DNA methylation is a useful biomarker for tumor metastasis. It has been reported that the voltage threshold of nanopore capture differs depending on the methylation level. Shim et al. demonstrated the larger current drop and longer dwell time of methylated parts than unmethylated parts of DNA.[14-15] The relationship between single-nucleotide polymorphisms (SNPs) and tumor is of great interest in the early diagnosis of cancer. The demonstrated threshold voltage dependence of sequence/enzyme indicates that the mutation site for the restriction enzyme can be recognized.[16] Yu et al. have demonstrated that the binding position of zinc finger protein in DNA is characterized by the location of the additional current drop in the blockade current signal (Fig. 1-5).[17]

A drug-screening application of nanopore sensing has also recently attracted attention. The drug screening is based on the detection of drug-bounded DNA locations and of protein-protein interactions (PPI). The interaction between p53TAD and MDM2 was monitored by translocation frequency changes and the effect of the drug molecule, nutlin-3, on the interaction was shown by Kwak et al. (Fig 1-6).[18] The heterogeneous properties of protein, such as structure, charge, and hydrophobic groups, complicate the analysis of nanopore transport. Hence, it is important to use the electro-osmotic driving force properly, due to the decreasing role of the electrophoretic force. Nanopore sensing exhibits clear advantages over conventional methods in biomedical applications in that it requires only small sample amounts and can perform rapid single-molecule detection.

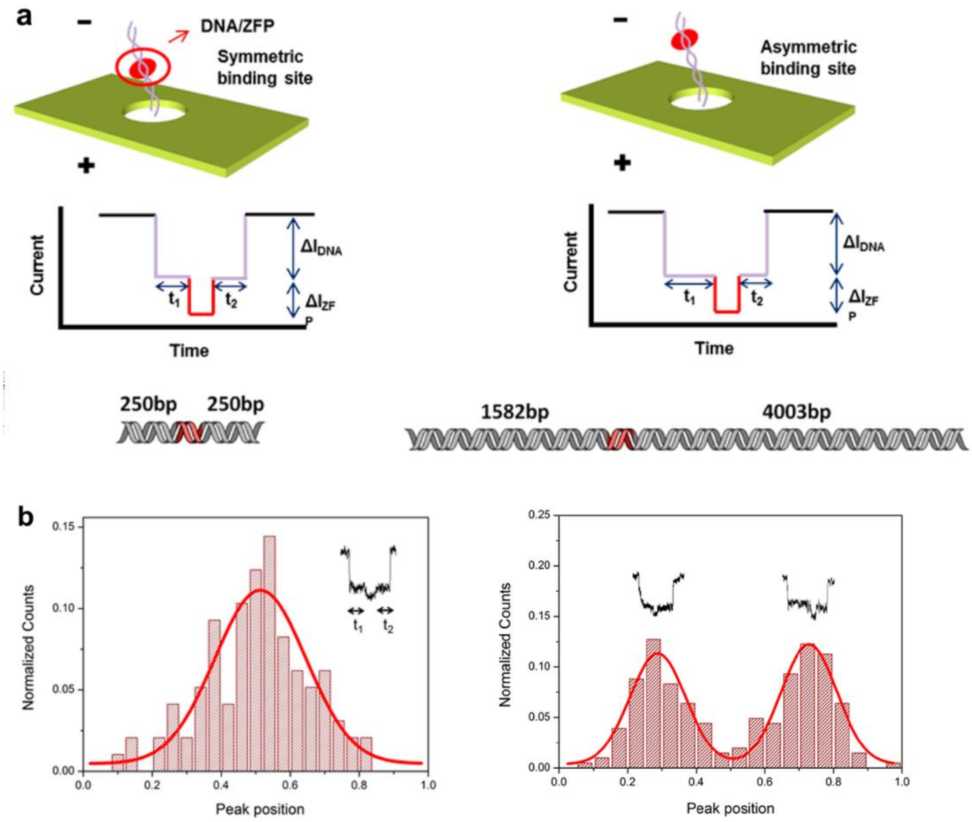

Figure 1-5 Diagnosis: detection of SNPs. (a) Schematics of experimental scheme; identifying the symmetric/asymmetric binding location of ZFP in DNA by additional current drop in blockade current. (b) Position of additional current drop indicates location (symmetric/asymmetric) of binding site.

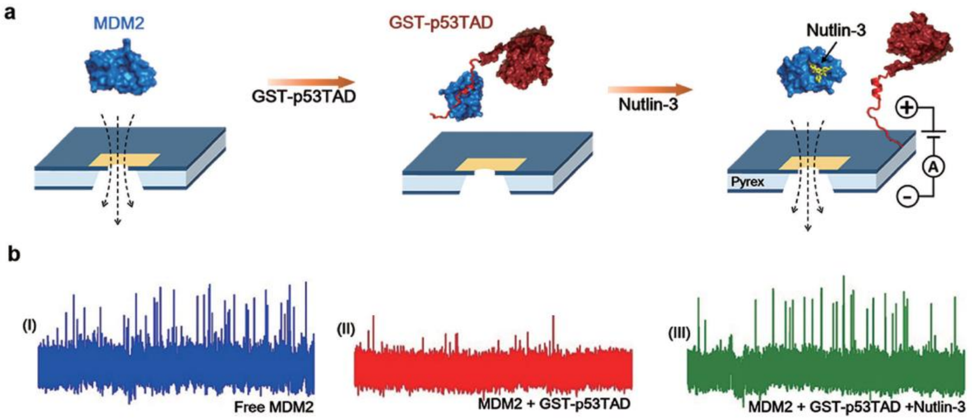

Figure 1-6 Drug screening: detection of PPI. (a) Schematics of experimental scheme; identifying the binding of MDM2/GST-p53TAD and detaching by drug molecule (Nutlin-3) through event frequency. (b) Traces of ion current versus time indicate that the low event frequency is caused by molecular binding.

1.2.3 Biological applications with functionalized nanopore

The greatest feature of nanopore is the “confinement effect”: that single molecules can be analyzed through molecule-comparable pore dimension. This feature has led to studies on surface functionalization of nanopores for specific target molecules. The analyte receptor has been integrated on the pore surface to observe molecule-molecule interaction in real time with changes in ion current, a technique that can be applied further to explore single-molecule dynamics in the interaction.[19-20] For instances, His-tagged Protein A was selectively bounded onto nitrilotriacetic acid (NTA) functional groups on the surface of ethylene glycol/gold/SiN nanopores and rejected interaction with the other antibodies (Fig. 1-7).[21] Interaction between RNA-binding ARPase P4 and oligoribonucleotides was detected by genetically modulated α-haemolysin protein pores.[22] These approaches require complex preparation in that the appropriate adapter must be selected and immobilized on the pore surface, but nanopores offer a solution to the limitation in sensitivity when the analyte is of low concentration or impurities exist at high levels.

The direction of nanopore surface modification includes functionality that shows conformational changes in response to external environmental stimuli. This idea is inspired by the ion channel embedded within the cell membrane, and has been implemented to control the physical process, as reviewed in Kowalczyk et al.[23] For instance, the G4 DNA, decorated in the nanopore surface, formed a closely packed structure to reduce the pore diameter in the presence of K^+ ion (Fig. 1-8).[24] The nucleoporin protein-coated nanopores allow the transport only of importin-β via specific interaction that opens the nanopore, and restrict the other non-specific proteins.[25]

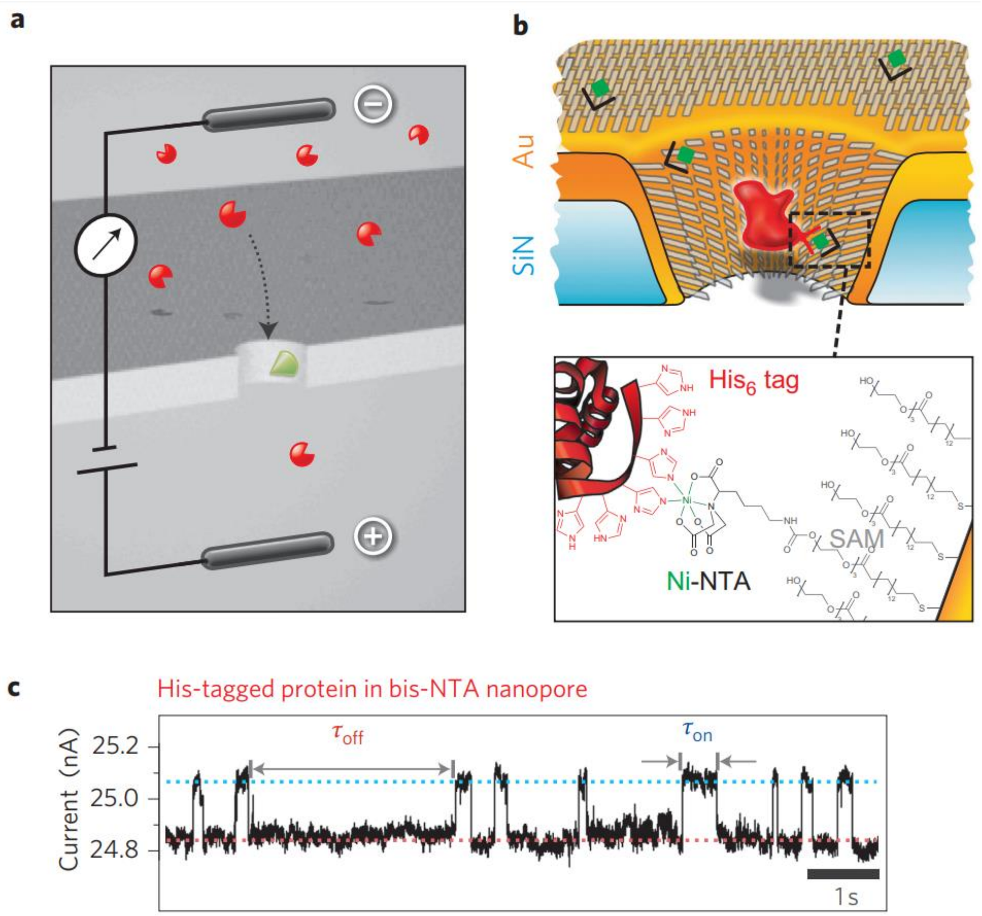

Figure 1-7 Functionalization of molecular specific sensing. (a) Sketch of experimental scheme. (b) Schematics of interaction between His-tagged protein and Ni-NTA receptor on SC15EG3/gold-coated SiN nanopore (c) Trace of current versus time indicates the stochastic sensing of protein. Adapted from Ref. 14.

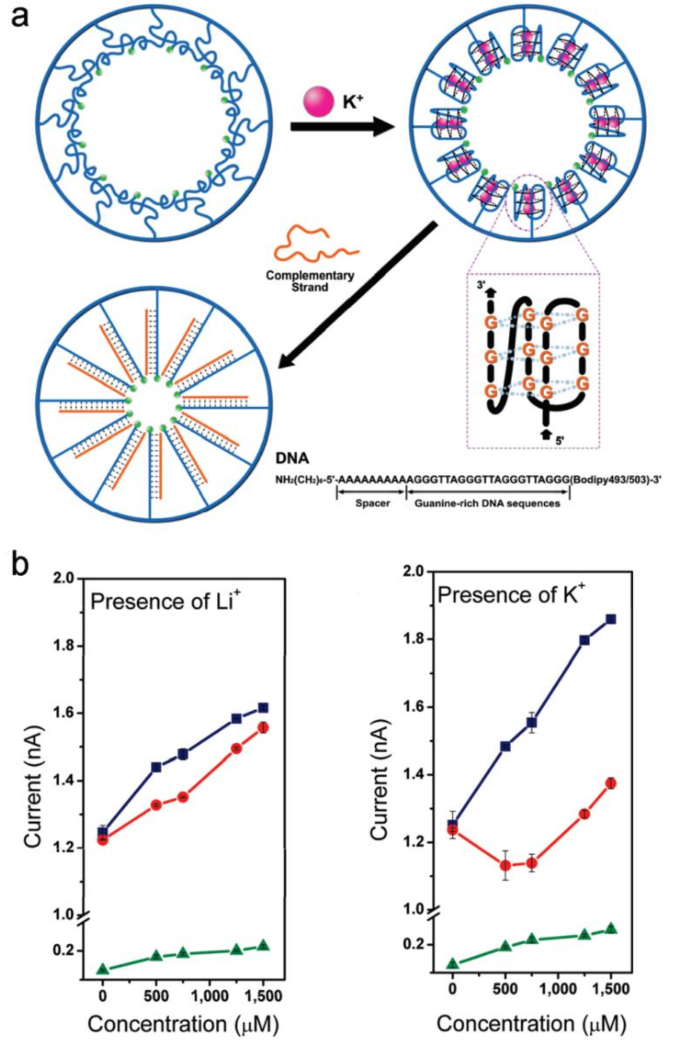

Figure 1-8 Biomimetic functionalized nanopore. (a) Schematics of opening and closing of nanopore by external stimuli using K^+ ion and G4 DNA. (b) Current-concentration properties of functionalized nanopore before G4 DNA modification (blue), after G4 DNA modification (red), addition of the complementary DNA strands.

1.3 Types of nanopore

Nanopores are classified into biological nanopores and solid-state nanopores according to the formation process, and recently studies have been carried out on the strengths and weaknesses of each. The biological nanopore utilizes the protein pores embedded in the lipid bilayer that formed on the teflon aperture.[26] The impaction of protein pores is monitored by ion current, and after the formation of a single pore, the experimental setup is prepared before additional pores form. The representative biological nanopore of α-haemolysin, extracted from the bacteria *Staphylococcus aureus*, appeared in the earliest stage of nanopore sensing since the process exhibits high reliability with sufficient yield.[3] The α-haemolysin has been extensively studied with the aim of DNA sequencing since its smallest diameter of 1.4 nm is comparable to the 1.1 nm of ssDNA.[19, 27-28] In particular, the protein genetic engineering technique led the development of the nanopore sensing field by exploring the molecular transport phenomena with the modulation of internal charge distribution and various functional groups.[27, 29-30] Another widely used biological nanopore, *mycobacterium smegmatis porin a* (MspA), improved spatial resolution by lowering the thickness of sensing zone to 1 nm from α-haemolysin's 5 nm.[31] In addition, the employment of phi 29 polymerase, which allows the reaction of dsDNA unzipping to a rate-determining step, is an important breakthrough in DNA sequencing applications, while slowing the translocation speed to the level required by the measurement system.[32-33] The fixed geometry of biological nanopores is valuable in ensuring reproducibility of data but limits application to other analytes. Although the use of various other protein pores has been explored, the yield of pore formation remains an issue to be solved in these pores, with poor lifetimes due to the instable lipid membrane.

Solid-state nanopores made in robust silicon materials or polymer film have emerged with advances in nanotechnology. The first solid-state nanopore was fabricated into silicon nitride by an ion beam.[34] This sub-3 nm-diameter nanopore was obtained by perforating the 50-100 nm pore first with a focused ion beam, and then narrowing it to a diffused ion beam. Since then, focused electron beams have made possible more precise control of pore dimension in silicon-based membranes, and have been widely used for various types of thin films, in particular 2D materials of thickness below 1 nm, with diameters of minimum 1 to tens of nm.[20, 35-36] In addition, a track-etch method for forming a conical pore in a polymer film,[37] a glass nanopipette with great advantages in terms of cost and mass production,[38] and a dielectric breakdown technique that is formed in an aqueous solution under the conditions of nanopore experiments by applying a strong voltage[39] have been used for pore formation. The surface characteristics of these pores have also been chemically modified by additional coating processes.[40] Although these top-down processes can control the pore dimension at the nm level, there are limitations in ensuring geometric reproducibility at the atomic level. Hence, many studies have worked on combining the protein pores or DNA origami with solid-state membranes.[41-42]

Solid-state nanopores have excelled in applications that have the following obvious advantages over biological nanopores: 1) The mechanical and chemical robustness allows long lifetime over a wide range of experimental conditions. 2) The adjustable pore dimensions allows a wide range of analytes. 3) Alternative detection methods, such as optical detection and tunneling current, can be integrated to obtain additional information.

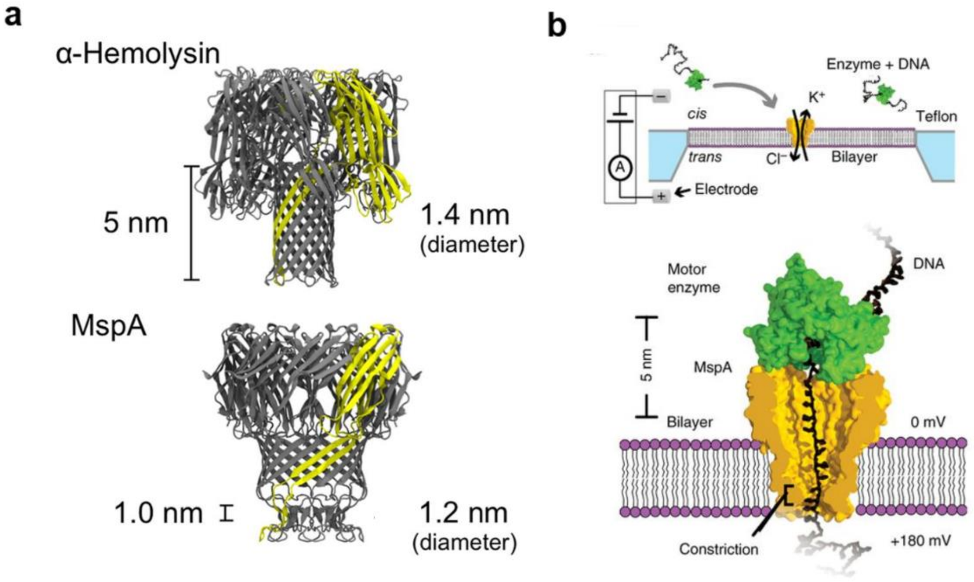

Figure 1-9 Biological nanopores and strategy for DNA sequencing. (a) The geometry of representative biological nanopores α-haemolysin and MspA. (b) Schematics of nanopore sequencing using lipid-embedded MspA with ssDNA bound to the motor enzyme (polymerase). Adapted from refs. 28 and 33.

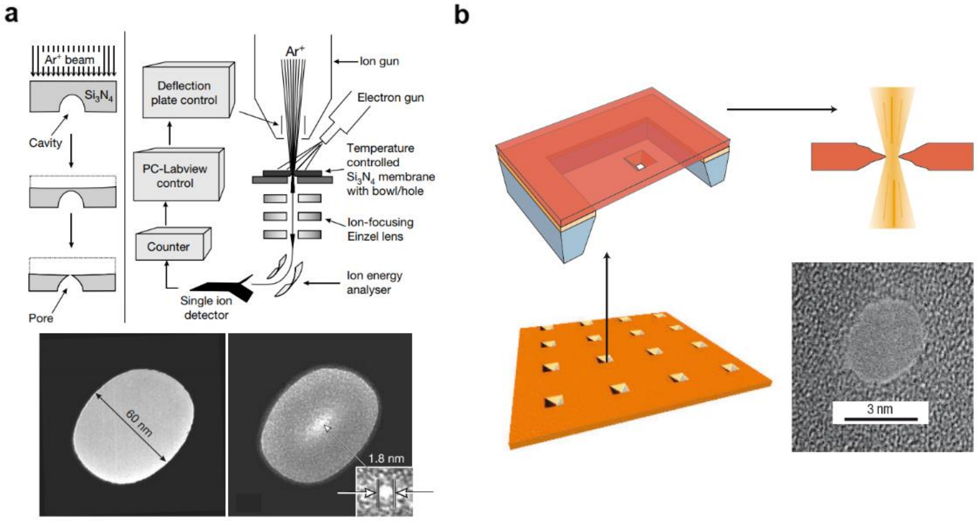

Figure 1-10 Fabrication of solid-state nanopores in Si-based membranes. (a) Ion-beam sculpting method developed by the Golovchenko group at Harvard University and TEM image of nanopore. (b) A focused electron-beam method developed by the Dekker group at Delft and TEM image of nanopore. Adapted from refs. 34 and 1.

1.4 Key issues in solid-state nanopores

1.4.1 Sensitivity issues

Nanopore sensing analyzes the molecular passage through blockade current (δI) and dwell time (t_d), and studies to improve the sensitivity have been conducted from three points of view: noise, spatial resolution, and temporal resolution. First, the electrical noise accompanied by the ion current measurement must be reduced to distinguish the differences in signal. The noise components of nanopores have four sources: called flicker, thermal, dielectric and amplifier noise. These sources show different dependency on the frequency (f) in the power spectral density in the fast Fourier transform of the current traces, as follows:[20]

$$S_{flicker} = A_N I^2 f^{-\beta} \quad (\propto f^{-\beta}),$$

$$S_{thermal} = 4kTG_{pore} \quad (\propto f^0),$$

$$S_{dielectric} = 8\pi kTC_{Chip}Df \quad (\propto f^1),$$

$$S_{amplifier} = \left(2\pi\left(C_{Chip} + C_w + C_{Amp}\right)v_n\right)^2 f^2 \quad (\propto f^2),$$

where A_N is noise power, I is the ion current, β is a fitting parameter close to 1, k is the Boltzmann constant, T is temperature, G_{pore} is the nanopore conductance, C_{Chip} is the device capacitance, D is dielectric loss,

C_w is electrode capacitance, C_{Amp} is amplifier capacitance, and v_n is the input-referred voltage noise of amplifier. The total noise is expressed as:

$$S_{total} = S_{flicker} + S_{thermal} + S_{dielectric} + S_{amplifier}.$$

Hence, the noise characteristics of nanopore can be improved by reducing the dominant source, as was noticed in fitting (Fig 1.11a). For instance, the dominant noise source in a conventional Si substrate-based nanopore is dielectric noise, and research has led to decreased capacitance and dielectric loss in devices.[43-45] The 2D-material membrane nanopore exhibits high flicker noise, which has been improved in work on mechanical stability of the membrane.[46-47] The spatial resolution is related to the requirement that nanopore thickness be less than the analytes to be identified. For example, a base-pair interval of DNA is 0.3 nm, and it is necessary to have a lower nanopore thickness than that interval to obtain information on only one nucleic acid in the blockade current signal.[48] In addition, the nanopore thickness has depends on the ion current through the pore:[7]

$$I = V \times \sigma \left(\frac{4h}{\pi d^2} + \frac{1}{d} \right)^{-1},$$

where V is the applied voltage, σ is the electrolyte conductivity, d is the pore diameter, and h is the nanopore thickness. This means that the blockade current can increase as the nanopore thickness decreases, thus increasing the signal-to-noise ratio. The blockade current (ΔI) for globular-shaped molecules is determined by[49-50]

$$d_H = [(\Delta I/I_0)(h+0.8d)d^2]^{1/3},$$

where d_H is the hydrodynamic protein diameter and I_0 is the open pore current, and this also shows the importance of nanopore thickness in the signal-to-noise ratio. There is an issue of temporal resolution: the speed of molecule translocation through the nanopore is fast compared to the sampling rate of the measurement equipment. Since the increase in noise from the increased bandwidth degrades the signal-to-noise ratio (Fig. 1-13), current technologies utilize measurement frequencies in the range 100 to 500 kHz and require a translocation speed of more than 10 μs per 1 analyte.[49-51]

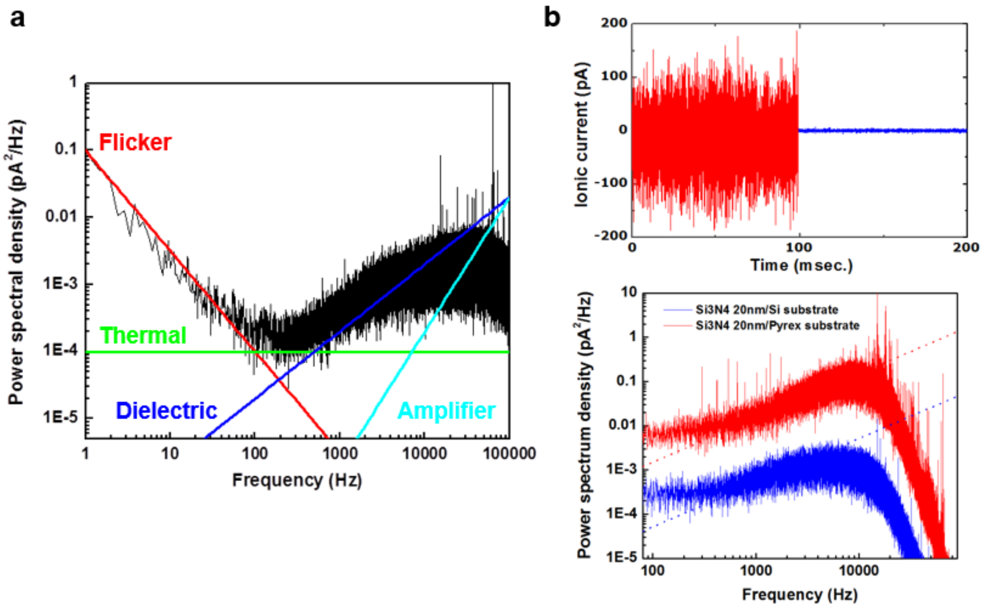

Figure 1-11 Noise on solid-state nanopore. (a) Noise analysis with fitting on power spectral density. The flicker, thermal, dielectric, and amplifier noise sources exhibit different dependencies on frequency. (b) Current traces for noise comparison between Si-based and Pyrex-based nanopores. PSD curves corresponding to current traces show the reduced dielectric noise in Pyrex-based nanopore. Adapted from ref. 45.

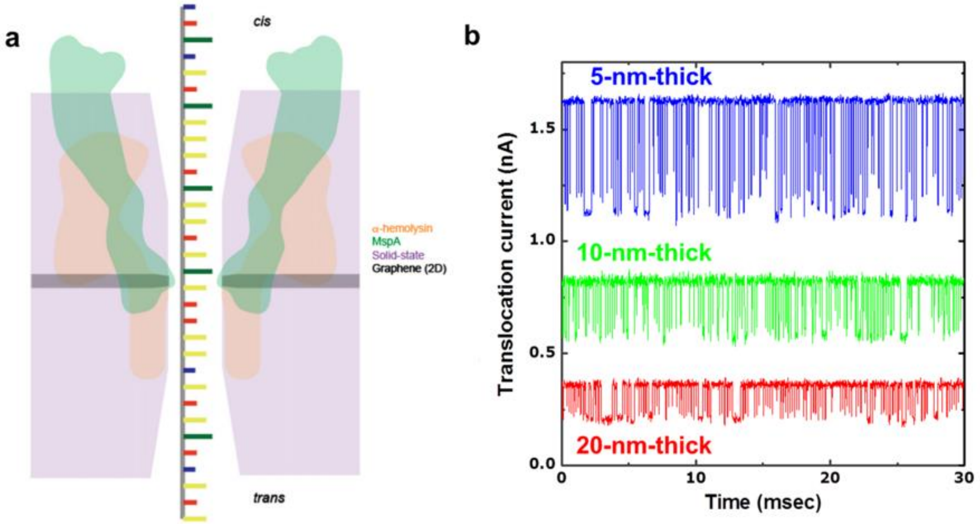

Figure 1-12 Spatial resolution and signal-to-noise ratio. (a) Comparison of the dimensions of α-haemolysin, MspA, SiN (solid-state), and graphene nanopores. The MspA and graphene nanopore exhibit excellent spatial resolution comparable to the base-pair interval of DNA. (b) Ion current traces for 40 nt ssDNA translocation shows the membrane thickness effect on signal-to-noise ratio. Adapted from refs. 48 and 45.

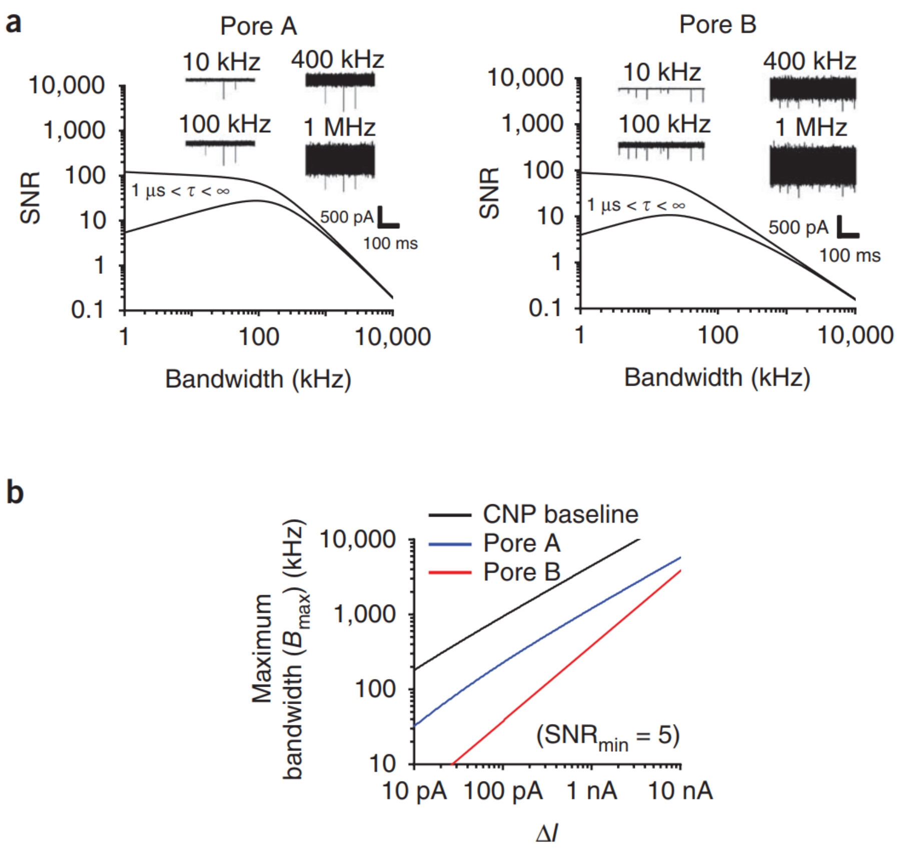

Figure 1-13 Temporal resolution and signal-to-noise ratio. (a) Signal-to-noise ratio as a function of measurement bandwidth for two nanopores using low-noise-amplifier system (CNP). (b) Maximum bandwidth defined by minimum signal-to-noise ratio of 5 as a function of amplitudes of blockade current. Adapted from ref. 51.

1.4.2 Issues in translocation behavior

Since nanopore sensing analyzes the molecular passages in an aqueous solution, controlling and optimizing molecular translocation behavior is a crucial issue. First, the molecules must be captured at a frequency that is optimized for the analysis. Slow capture rates can degrade throughput and analytical efficiency, and fast capture rates can interfere with the analysis by broadening signal spreads from molecule/molecule or molecule/pore interactions. Subsequently, the molecule must pass through the nanopore more slowly than the temporal resolution of the measurement system, as described in the previous section. In the case of DNA, we can understand the translocation behavior to a great extent. DNA basically follows electrophoretic capture well due to its uniform and strong charge of $-2e/0.34$ nm, and it exhibits sufficient dwell time in the molecular unit due to its long-chain form. However, proteins have unique structures and heterogeneous charge profiles, complicating the capture behavior, and often have too fast passage speed. Hence, the effect of each physical and chemical characteristic on translocation behavior needs further investigation. Finally, the molecule clogging on the pore surface that stops the analysis and determine the lifetime of devices must be controlled. The clogging is usually reversible by a change in applied voltage, but there is occasional irreversible clogging. Hence, surface treatments have been carried out to reduce clogging frequency.

Strategies to control and optimize translocation behavior on nanopores fall into three categories: control of experimental conditions, externally applied forces, and changes in pore surfaces. First, in controlling experimental conditions, the electrophoretic forces on the molecule is controlled by changing the applied voltage or influencing the molecule's electrophoretic mobility.[52-53] However, the strategy of slowing the translocation speed by changing voltage, electrolyte and temperature has the practical limitation that it accompanies the loss of current signal. Second, external forces, such as laser illumination and gate voltage, have been applied to the molecule, mainly using the changes in surface charge characteristics of nanopores.[54-58] Finally, studies that modify the surface properties of nanopores have been conducted by altering the membrane material[59-60] or by coating with organic materials.[61-63] This approach also utilizes the surface charge characteristics or interactions between molecule and pore surfaces. The effect of surface charge on molecule translocation is discussed in detail in the following chapter.

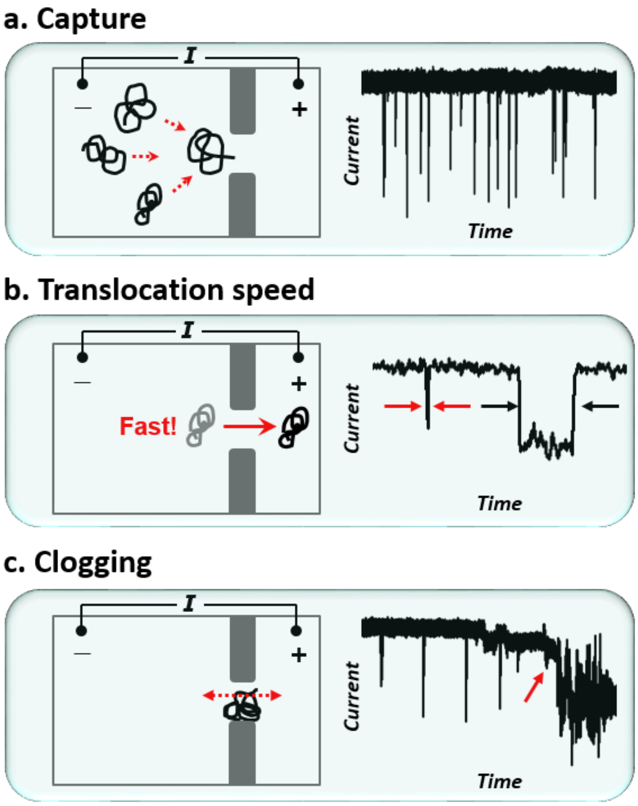

Figure 1-14 Translocation behavior to be controlled in nanopore sensing. (a) Capture of molecules on the nanopore and the capture signal on the current trace. (b) Molecular translocation speed required for temporal resolution of the measurement system; examples of too fast event (red) and sufficiently slow event (black) in current trace. (c) Clogging of molecule to nanopore and the clogging signal on the current trace.

1.5 Outline of dissertation

This dissertation describes research results on surface charge effects on molecule translocation behavior in solid-state nanopore through the strategies of laser illumination and polymer membrane.

Chapter 1 gives an overview of nanopore sensing. We explain the concept of nanopore sensing and summarize which applications are attracting attention. The competitiveness of biological nanopores in DNA sequencing is noted, and it is pointed out that understanding and adjusting molecular transport dynamics is a key issue, as is improving the sensitivity in solid-state nanopores. Chapter 2 reviews the effect of surface charge characteristics on molecular transport categorized by electro-osmotic flow and electrostatic interaction in nanopore sensing. In particular, it contains the background of the strategies for surface charge modulation presented in this dissertation. Chapter 3 describes photo-induced noise and surface charge in silicon nitride nanopores. By using our low-noise nanopore platform, synchronized optical and electronic detection of biomolecules is demonstrated. Chapter 4 discusses the polyurea nanopore with dimension controllability and unique high negative surface charge characteristics by using molecular-layer deposition techniques. In particular, high-throughput detection of small proteins is achieved by the dominant role of electro-osmotic flow in molecule capture. Finally, in chapter 5, we summarize the results of this study and suggest follow-up work to further the fundamental understanding of molecule translocation in nanopores.

References

1. Dekker, C., Solid-state nanopores. *Nature Nanotechnology* **2007,** *2*, 209.

2. Deamer, D.; Akeson, M.; Branton, D., Three decades of nanopore sequencing. *Nature Biotechnology* **2016,** *34*, 518.

3. Kasianowicz, J. J.; Brandin, E.; Branton, D.; Deamer, D. W., Characterization of individual polynucleotide molecules using a membrane channel. *Proceedings of the National Academy of Sciences* **1996,** *93* (24), 13770-13773.

4. Bayley, H.; Cremer, P. S., Stochastic sensors inspired by biology. *Nature* **2001,** *413*, 226.

5. Derrington, I. M.; Butler, T. Z.; Collins, M. D.; Manrao, E.; Pavlenok, M.; Niederweis, M.; Gundlach, J. H., Nanopore DNA sequencing with MspA. *Proceedings of the National Academy of Sciences* **2010,** *107* (37), 16060-16065.

6. Shi, W.; Friedman, A. K.; Baker, L. A., Nanopore Sensing. *Analytical Chemistry* **2017,** *89* (1), 157-188.

7. Wanunu, M., Nanopores: A journey towards DNA sequencing. *Physics of life reviews* **2012,** *9* (2), 125-158.

8. Kist, L. T. C. F. a. E. C. a. T. B. L., A review of DNA sequencing techniques. *Quarterly reviews of biophysics* **2002,** *35 2*, 169-200.

9. Hutchison, I. I. I. C. A., DNA sequencing: bench to bedside and beyond †. *Nucleic Acids Research* **2007,** *35* (18), 6227-6237.

10. Rhee, M.; Burns, M. A., Nanopore sequencing technology: research trends and applications. *Trends in Biotechnology* **2006,** *24* (12), 580-586.

11. Eisenstein, M., An ace in the hole for DNA sequencing. *Nature* **2017,** *550*, 285.

12. Wanunu, M.; Bhattacharya, S.; Xie, Y.; Tor, Y.; Aksimentiev, A.; Drndic, M., Nanopore Analysis of Individual RNA/Antibiotic Complexes. *ACS Nano* **2011,** *5* (12), 9345-9353.

13. Shim, J. W.; Gu, L.-Q., Encapsulating a Single G-Quadruplex Aptamer in a Protein Nanocavity. *The Journal of Physical Chemistry B* **2008,** *112* (28), 8354-8360.

14. Shim, J.; Humphreys, G. I.; Venkatesan, B. M.; Munz, J. M.; Zou, X.; Sathe, C.; Schulten, K.; Kosari, F.; Nardulli, A. M.; Vasmatzis, G.; Bashir, R., Detection and quantification of methylation in DNA using solid-state nanopores. *Sci Rep* **2013,** *3*, 1389.

15. Shim, J.; Kim, Y.; Humphreys, G. I.; Nardulli, A. M.; Kosari, F.; Vasmatzis, G.; Taylor, W. R.; Ahlquist, D. A.; Myong, S.; Bashir, R., Nanopore-Based Assay for Detection of Methylation in Double-Stranded DNA Fragments. *ACS Nano* **2015,** *9* (1), 290-300.

16. Zhao, Q.; Sigalov, G.; Dimitrov, V.; Dorvel, B.; Mirsaidov, U.; Sligar, S.; Aksimentiev, A.; Timp, G., Detecting SNPs Using a Synthetic Nanopore. *Nano Letters* **2007,** *7* (6), 1680-1685.

17. Yu, J.-S.; Lim, M.-C.; Huynh, D. T. N.; Kim, H.-J.; Kim, H.-M.; Kim, Y.-R.; Kim, K.-B., Identifying the Location of a Single Protein along the DNA Strand Using Solid-State Nanopores. *ACS Nano* **2015,** *9* (5), 5289-5298.

18. Kwak, D.-K.; Chae, H.; Lee, M.-K.; Ha, J.-H.; Goyal, G.; Kim, M. J.; Kim, K.-B.; Chi, S.-W., Probing the Small-Molecule Inhibition of an Anticancer Therapeutic Protein-Protein Interaction Using a Solid-State Nanopore. *Angewandte Chemie International Edition* **2016,** *55* (19), 5713-5717.

19. Haque, F.; Li, J.; Wu, H.-C.; Liang, X.-J.; Guo, P., Solid-state and biological nanopore for real-time sensing of single chemical and sequencing of DNA. *Nano Today* **2013,** *8* (1), 56-74.

20. Lee, K.; Park, K.-B.; Kim, H.-J.; Yu, J.-S.; Chae, H.; Kim, H.-M.; Kim, K.-B., Recent Progress in Solid-State Nanopores. *Adv Mater* **2018,** *30* (42), 1704680.

21. Wei, R.; Gatterdam, V.; Wieneke, R.; Tampé, R.; Rant, U., Stochastic sensing of proteins with receptor-modified solid-state nanopores. *Nat. Nanotechnol.* **2012,** *7,* 257.

22. Astier, Y.; Kainov, D. E.; Bayley, H.; Tuma, R.; Howorka, S., Stochastic Detection of Motor Protein–RNA Complexes by Single-Channel Current Recording. *ChemPhysChem* **2007,** *8* (15), 2189-2194.

23. Kowalczyk, S. W.; Blosser, T. R.; Dekker, C., Biomimetic nanopores: learning from and about nature. *Trends in biotechnology* **2011,** *29* (12), 607-614.

24. Hou, X.; Guo, W.; Xia, F.; Nie, F.-Q.; Dong, H.; Tian, Y.; Wen, L.; Wang, L.; Cao, L.; Yang, Y.; Xue, J.; Song, Y.; Wang, Y.; Liu, D.; Jiang, L., A Biomimetic Potassium Responsive Nanochannel: G-Quadruplex DNA Conformational Switching in a Synthetic Nanopore. *Journal of the American Chemical Society* **2009,** *131* (22), 7800-7805.

25. Kowalczyk, S. W.; Kapinos, L.; Blosser, T. R.; Magalhaes, T.; van Nies, P.; Lim, R. Y.; Dekker, C., Single-molecule transport across an individual biomimetic nuclear pore complex. *Nature nanotechnology* **2011,** *6* (7), 433-8.

26. Laszlo, A. H.; Derrington, I. M.; Gundlach, J. H., MspA nanopore as a single-molecule tool: From sequencing to SPRNT. *Methods* **2016,** *105*, 75-89.

27. Howorka, S.; Siwy, Z., Nanopore analytics: sensing of single molecules. *Chemical Society Reviews* **2009,** *38* (8), 2360-2384.

28. Manara, R. M. A.; Jayne Wallace, E.; Khalid, S., DNA sequencing with MspA: Molecular Dynamics simulations reveal free-energy differences between sequencing and non-sequencing mutants. *Scientific Reports* **2015,** *5*, 12783.

29. Schneider, G. F.; Dekker, C., DNA sequencing with nanopores. *Nat Biotech* **2012,** *30* (4), 326-328.

30. Branton, D.; Deamer, D. W.; Marziali, A.; Bayley, H.; Benner, S. A.; Butler, T.; Di Ventra, M.; Garaj, S.; Hibbs, A.; Huang, X.; Jovanovich, S. B.; Krstic, P. S.; Lindsay, S.; Ling, X. S.; Mastrangelo, C. H.; Meller, A.; Oliver, J. S.; Pershin, Y. V.; Ramsey, J. M.; Riehn, R.; Soni, G. V.; Tabard-Cossa, V.; Wanunu, M.; Wiggin, M.; Schloss, J. A., The potential and challenges of nanopore sequencing. *Nat Biotech* **2008,** *26* (10), 1146-1153.

31. Butler, T. Z.; Pavlenok, M.; Derrington, I. M.; Niederweis, M.; Gundlach, J. H., Single-molecule DNA detection with an engineered MspA protein nanopore. *Proceedings of the National Academy of Sciences* **2008,** *105* (52), 20647-20652.

32. Manrao, E. A.; Derrington, I. M.; Laszlo, A. H.; Langford, K. W.; Hopper, M. K.; Gillgren, N.; Pavlenok, M.; Niederweis, M.; Gundlach, J. H., Reading DNA at single-nucleotide resolution with a mutant MspA nanopore and phi29 DNA polymerase. *Nature biotechnology* **2012,** *30* (4), 349-353.

33. Derrington, I. M.; Craig, J. M.; Stava, E.; Laszlo, A. H.; Ross, B. C.; Brinkerhoff, H.; Nova, I. C.; Doering, K.; Tickman, B. I.; Ronaghi, M.; Mandell, J. G.; Gunderson, K. L.; Gundlach, J. H., Subangstrom single-molecule measurements of motor proteins using a nanopore. *Nature biotechnology* **2015,** *33*, 1073.

34. Li, J.; Stein, D.; McMullan, C.; Branton, D.; Aziz, M. J.; Golovchenko, J. A., Ion-beam sculpting at nanometre length scales. *Nature* **2001,** *412*, 166.

35. Dekker, C., Solid-state nanopores. *Nature nanotechnology* **2007,** *2* (4), 209-15.

36. Storm, A. J.; Chen, J. H.; Ling, X. S.; Zandbergen, H. W.; Dekker, C., Fabrication of solid-state nanopores with single-nanometre precision. *Nature Materials* **2003,** *2*, 537.

37. Mara, A.; Siwy, Z.; Trautmann, C.; Wan, J.; Kamme, F., An Asymmetric Polymer Nanopore for Single Molecule Detection. *Nano Letters* **2004,** *4* (3), 497-501.

38. Steinbock, L. J.; Krishnan, S.; Bulushev, R. D.; Borgeaud, S.; Blokesch, M.; Feletti, L.; Radenovic, A., Probing the size of proteins with glass nanopores. *Nanoscale* **2014,** *6* (23), 14380-7.

39. Kwok, H.; Briggs, K.; Tabard-Cossa, V., Nanopore Fabrication by Controlled Dielectric Breakdown. *PLoS ONE* **2014,** *9* (3), e92880.

40. Wanunu, M.; Meller, A., Chemically Modified Solid-State Nanopores. *Nano Letters* **2007,** *7* (6), 1580-1585.

41. Hall, A. R.; Scott, A.; Rotem, D.; Mehta, K. K.; Bayley, H.; Dekker, C., Hybrid pore formation by directed insertion of [alpha]-haemolysin into solid-state nanopores. *Nat Nano* **2010,** *5* (12), 874-877.

42. Bell, N. A. W.; Engst, C. R.; Ablay, M.; Divitini, G.; Ducati, C.; Liedl, T.; Keyser, U. F., DNA Origami Nanopores. *Nano Letters* **2012,** *12* (1), 512-517.

43. Tabard-Cossa, V.; Trivedi, D.; Wiggin, M.; Jetha, N. N.; Marziali, A., Noise analysis and reduction in solid-state nanopores. *Nanotechnology* **2007,** *18* (30), 305505.

44. Smeets, R. M. M.; Keyser, U. F.; Dekker, N. H.; Dekker, C., Noise in solid-state nanopores. *Proceedings of the National Academy of Sciences of the United States of America* **2008,** *105* (2), 417-421.

45. Lee, M. H.; Kumar, A.; Park, K. B.; Cho, S. Y.; Kim, H. M.; Lim, M. C.; Kim, Y. R.; Kim, K. B., A low-noise solid-state nanopore platform based on a highly insulating substrate. *Sci Rep* **2014,** *4*, 7448.

46. Heerema, S. J.; Schneider, G. F.; Rozemuller, M.; Vicarelli, L.; Zandbergen, H. W.; Dekker, C., 1/f noise in graphene nanopores. *Nanotechnology* **2015,** *26* (7), 074001.

47. Park, K.-B.; Kim, H.-J.; Kim, H.-M.; Han, S. A.; Lee, K. H.; Kim, S.-W.; Kim, K.-B., Noise and sensitivity characteristics of solid-state nanopores with a boron nitride 2-D membrane on a pyrex substrate. *Nanoscale* **2016,** *8* (10), 5755-5763.

48. Carson, S.; Wanunu, M., *Challenges in DNA motion control and sequence readout using nanopore devices*. 2015; Vol. 26, p 074004.

49. Waduge, P.; Hu, R.; Bandarkar, P.; Yamazaki, H.; Cressiot, B.; Zhao, Q.; Whitford, P. C.; Wanunu, M., Nanopore-Based Measurements of Protein Size, Fluctuations, and Conformational Changes. *ACS Nano* **2017,** *11* (6), 5706-5716.

50. Larkin, J.; Henley, R. Y.; Muthukumar, M.; Rosenstein, Jacob K.; Wanunu, M., High-Bandwidth Protein Analysis Using Solid-State Nanopores. *Biophysical Journal 106* (3), 696-704.

51. Rosenstein, J. K.; Wanunu, M.; Merchant, C. A.; Drndic, M.; Shepard, K. L., Integrated nanopore sensing platform with sub-microsecond temporal resolution. *Nature Methods* **2012,** *9*, 487.

52. Fologea, D.; Uplinger, J.; Thomas, B.; McNabb, D. S.; Li, J., Slowing DNA Translocation in a Solid-State Nanopore. *Nano Letters* **2005,** *5* (9), 1734-1737.

53. Kowalczyk, S. W.; Wells, D. B.; Aksimentiev, A.; Dekker, C., Slowing down DNA Translocation through a Nanopore in Lithium Chloride. *Nano Letters* **2012,** *12* (2), 1038-1044.

54. Trepagnier, E. H.; Radenovic, A.; Sivak, D.; Geissler, P.; Liphardt, J., Controlling DNA Capture and Propagation through Artificial Nanopores. *Nano Letters* **2007,** *7* (9), 2824-2830.

55. He, Y.; Tsutsui, M.; Fan, C.; Taniguchi, M.; Kawai, T., Controlling DNA Translocation through Gate Modulation of Nanopore Wall Surface Charges. *ACS Nano* **2011,** *5* (7), 5509-5518.

56. Keyser, U. F.; Does, J. v. d.; Dekker, C.; Dekker, N. H., Optical tweezers for force measurements on DNA in nanopores. *Review of Scientific Instruments* **2006,** *77* (10), 105105.

57. Di Fiori, N.; Squires, A.; Bar, D.; Gilboa, T.; Moustakas, T. D.; Meller, A., Optoelectronic control of surface charge and translocation dynamics in solid-state nanopores. *Nature nanotechnology* **2013,** *8* (12), 946-951.

58. Cadinu, P.; Campolo, G.; Pud, S.; Yang, W.; Edel, J. B.; Dekker, C.; Ivanov, A. P., Double Barrel Nanopores as a New Tool for Controlling Single-Molecule Transport. *Nano Letters* **2018**.

59. Larkin, J.; Henley, R.; Bell, D. C.; Cohen-Karni, T.; Rosenstein, J. K.; Wanunu, M., Slow DNA Transport through Nanopores in Hafnium Oxide Membranes. *ACS Nano* **2013,** *7* (11), 10121-10128.

60. Park, K.-B.; Kim, H.-J.; Kang, Y.-H.; Yu, J.-S.; Chae, H.; Lee, K.; Kim, H.-M.; Kim, K.-B., Highly reliable and low-noise solid-state nanopores with an atomic layer deposited ZnO membrane on a quartz substrate. *Nanoscale* **2017,** *9* (47), 18772-18780.

61. Yusko, E. C.; Johnson, J. M.; Majd, S.; Prangkio, P.; Rollings, R. C.; Li, J.; Yang, J.; Mayer, M., Controlling protein translocation through nanopores with bio-inspired fluid walls. *Nat Nano* **2011,** *6* (4), 253-260.

62. Ren, R.; Zhang, Y.; Nadappuram, B. P.; Akpinar, B.; Klenerman, D.; Ivanov, A. P.; Edel, J. B.; Korchev, Y., Nanopore extended field-effect transistor for selective single-molecule biosensing. *Nature Communications* **2017,** *8* (1), 586.

63. Anderson, B. N.; Muthukumar, M.; Meller, A., pH Tuning of DNA

Translocation Time through Organically Functionalized Nanopores. *ACS nano* **2013,** *7* (2), 1408-1414.

Chapter 2.

Review: the effect of the surface charge characteristic on molecular transport through nanopores

2.1 Effect of electro-osmotic flow

For the electrical detection of biomolecule translocation using nanopores, a voltage is applied across the pore for ion current measurement, resulting in electro-osmotic flow that depends on the surface charge of the pore. Electro-osmotic flow arises from a counter-ion layer formed to shield the charge of a solid surface; it is called the electric double layer and is composed of a compact layer and a diffuse layer. The electric field produces drag on the ions in the diffuse layer to produce an effective slip velocity (v_{EO}) given by Helmholtz-Smoluchowski equation:

$$v_{EO} = -{}^{\epsilon\zeta}/_{\eta}\, E$$

where ϵ is permittivity of the electrolyte solution, ζ is the zeta potential of the pore wall, η is the viscosity of the electrolyte solution, and E th eis electric field. The zeta potential ζ can be derived from the relation with surface charge density under certain electrolyte conditions using Grahame's equation

$$\sigma = \frac{2\epsilon k_B T}{e\lambda_D}\sinh(\frac{e\zeta}{2k_B T})$$

where k_BT is thermal energy and λ_D is the Debye screening length, which is the thickness of the electric double layer. The Debye screening length (λ_D) is determined by the concentration of the electrolyte as

$$\lambda_D = \sqrt{\frac{\epsilon k_B T}{2e^2 n_{KCl}}}$$

The velocity of electro-osmotic flow (v_{EO}) can be estimated at about 0.1 m/s under typical experimental conditions for nanopores: pore diameter 6 nm, pore thickness 20 nm, applied voltage 0.3 V, and zeta potential -10 mV. This fluid flow can affect capture or translocation behavior by applying a hydrodynamic viscous drag force to the molecule in a direction the same as or opposite to the electrophoretic driving force.[1] He et al., in a theoretical investigation of the quantitative relation between DNA translocation behavior and the surface charge density manipulated by gate voltage, demonstrated that a high DNA capture rate is obtained by anionic electro-osmotic flow enhancing capturing radius.[2]

Conversely, when DNA stays in the pore, cationic electro-osmotic flow delays the DNA transport. Many experimental studies that altered surface charge in nanopores have reported the effect of electro-osmotic flow on biomolecule capture,[3-9] but only one experimental study has reported the effect on the transport speed.[5] For instances, pioneers in the field pointed to negative surface-charge density as a origin of low dsDNA capture rates in SiN nanopores and showed the enhanced capture rate by coating the pore surface with positively charged aluminum oxide.[3] Ren et al. fabricated a field-effect transistor on a glass nanopipette and demonstrated that the low 3kbp dsDNA capture rate of 0.15 events/sec at −0.4 V gate bias can be enhanced to 4.8 events/sec at +0.4 V gate bias.[7] In case of protein analytes, Firnkes et al. demonstrated the effect of electro-osmotic flow on protein capture (Avidin, PZC of pH 8) by altering the electrolyte pH.[10] While the positively charged SiN pore surface enhanced the protein capture to 90 events/sec at pH 4, the negatively charged pore surface reduce it to 6 events/sec at pH 6. Waduge et al. show that a few kinds of protein in a net charge range from −6 to +7 translocate in the direction of electro-osmotic flow irrespective of the electrophoretic direction.[6]

The internal charge of biological nanopores can be precisely modified by protein engineering. Modification with positive charge enhances the 92 nt ssDNA capture in α-hemolysin pores[8] and the 290 bp dsDNA capture in ClyA pores.[9] On the other hand, the effect of electro-osmotic flow on transport speed has been reported only by Di Fiori et al.[5] They demonstrated that the electro-osmotic flow from a laser-induced negative surface charge density of about −100 mC/m^2 in SiN nanopores slows down the 5kbp dsDNA transport from a mean dwell time of 1.2 ms to 12 ms and reduces the capture rate from 3.3 events/sec to 1.4 events/sec.

In summary, in case of biomolecule capture, the diffusion is minor in the electric-field-dominant region around the pore, and hence the effect of the electro-osmotic flow by electric field can be observed well. On the other hand, when a molecule passes through a pore, it is hard to observe the effect of electro-osmotic flow because other drag forces in addition to that from electric field must be considered, such as surface friction force by molecule/pore interaction, viscous drag in solution, and entropic barrier from changes in molecular conformation.

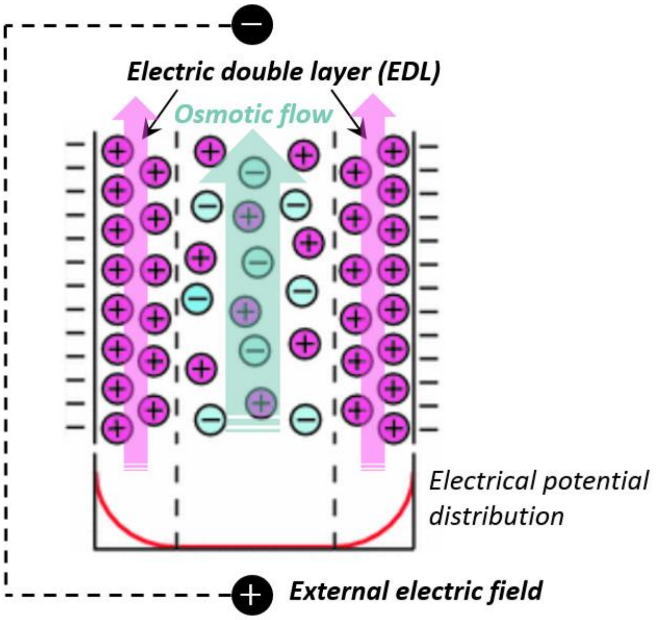

Figure 2-1 Electro-osmotic flow. The electrophoretic drift of positive ions in the diffuse part of electric double layer produces drag on the fluid and hence an electro-osmotic flow.

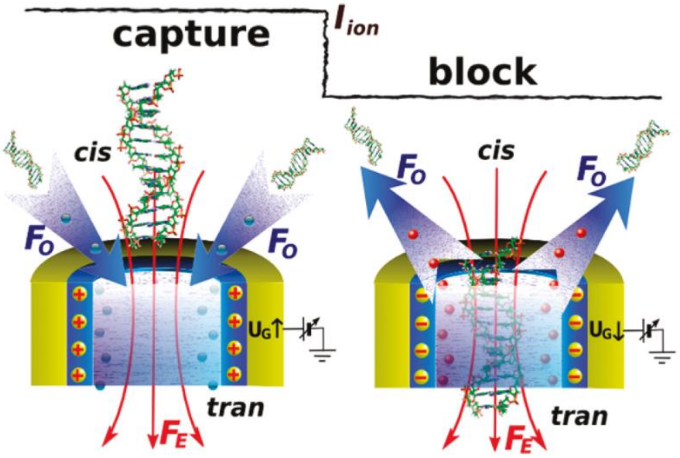

Figure 2-2 Control of DNA motion by electro-osmotic flow. Schematics of gate manipulation of DNA capture and transport with ion-current feedback system. Anionic electro-osmotic flow enhances the DNA capture and thus alters cationic electro-osmotic flow so as to slow down DNA transport. Adapted from ref. 2.

2.2 Electrostatic interaction between biomolecule and pore

Electrostatic interaction, also called Coulomb interaction, is the attraction or repulsion of objects due to their electrical charges. By electrostatic interaction, nanopores with opposite charges to analytes can enhance the capture rate by attraction force or can act as a friction force that slows down molecular transport. Similarly, nanopores with the same charge as the analyte could be useful in reducing signal scattering or preventing unwanted adsorption and clogging of molecules. Of course, electrostatic interaction can affect molecule capture on nanopores. However, in general solid-state nanopore experimental conditions, the effect of electrostatic interaction on molecule capture is expected to be less than that of electro-osmotic flow for the following reasons: a high-ionic-strength condition (1 M or more) is conventionally used to obtain a signal of sufficient magnitude. In this condition, the nanopore diameter of the order of a few nm is often considerably larger than the Debye screening length (0.3 nm at 1 M) where the charge is shielded. On the other hand, electro-osmotic flow can extend the capture radius on the order of a few hundred nm around the nanopore.[2] In addition, since the repulsion force has not yet been meaningfully utilized in present techniques, this chapter focuses on studies that use electrostatic attraction force to reduce the transport speed. In the case of DNA, many previous studies have shown retarding of DNA motion by direct electrostatic interaction with nanopores.[7, 11-18] For instance, Anderson et al. coated SiN with 3-(amino-propyl)tri-methoxysilane to achieve positively charged pore surfaces and slowed down the 1 kbp DNA translocation from a dwell time of 11 μs (SiN nanopore) to 25 μs.[13] Venkatesan et al. have indicated long times for DNA translocation owing to significant interactions between DNA and positively charged Al_2O_3 nanopores.[11] Experimental studies using nanopore extended-field-effect transistors by three research groups have shown that positive gate bias retards the translocation of dsDNA (Fig. 2-3).[7, 16, 18] Park et al. have shown that the voltage dependence of the electrostatic interaction between DNA and ZnO nanopores is in agreement with simulation study of particle-pore interaction on transport.[12] Until now, the effect of electrostatic interaction has not been studied for protein analytes because of their large translocation speed and heterogeneous charge profiles. Table 2-1 summarizes the changes in transport speed reported in studies that modify the nanopore surface charge. Although the combined effect of driving forces and drag forces may or may not cause a change in speed in the electro-osmotic direction, many studies have reported slowing down of DNA through electrostatic interaction. Taking all factors into account, electrostatic interaction is a sufficiently reliable strategy to reduce transport speeds in nanopores.

.

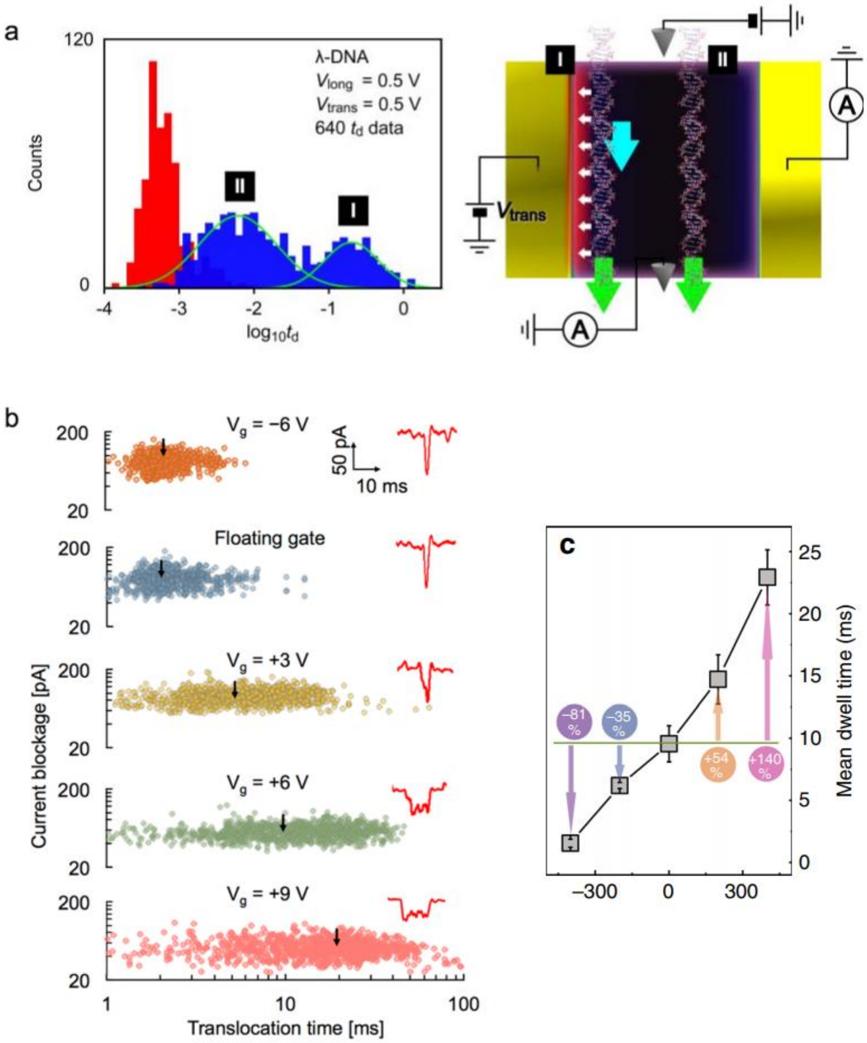

Figure 2-3 Electrostatic retardation of DNA transport in field-effect transistor. (a) Slowing of DNA transport with +0.5 V gate bias and dwell time distribution indicates events with electrostatic interaction with pore surface. (b), (c) Increase of mean dwell time with increase of positive gate voltage. Adapted from refs. 18, 16 and 7.

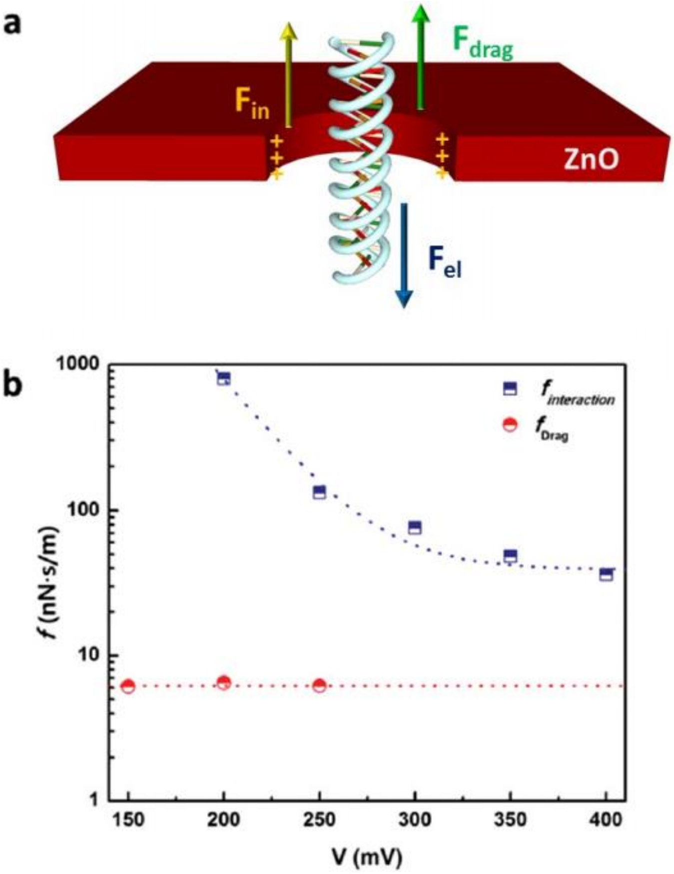

Figure 2-4 Driving and drag forces on DNA with electrostatic interaction. (a) The surface frictional force from electrostatic interaction between DNA and pore (F_{in}), hydrodynamic drag force (F_{drag}) and electrophoretic driving force (F_{el}) (b) experimentally extracted friction coefficient of electrostatic interaction between DNA and positively charged ZnO nanopore. Adapted from ref. 12.

Table 2-1 Effect of surface charge modification on biomolecule transport

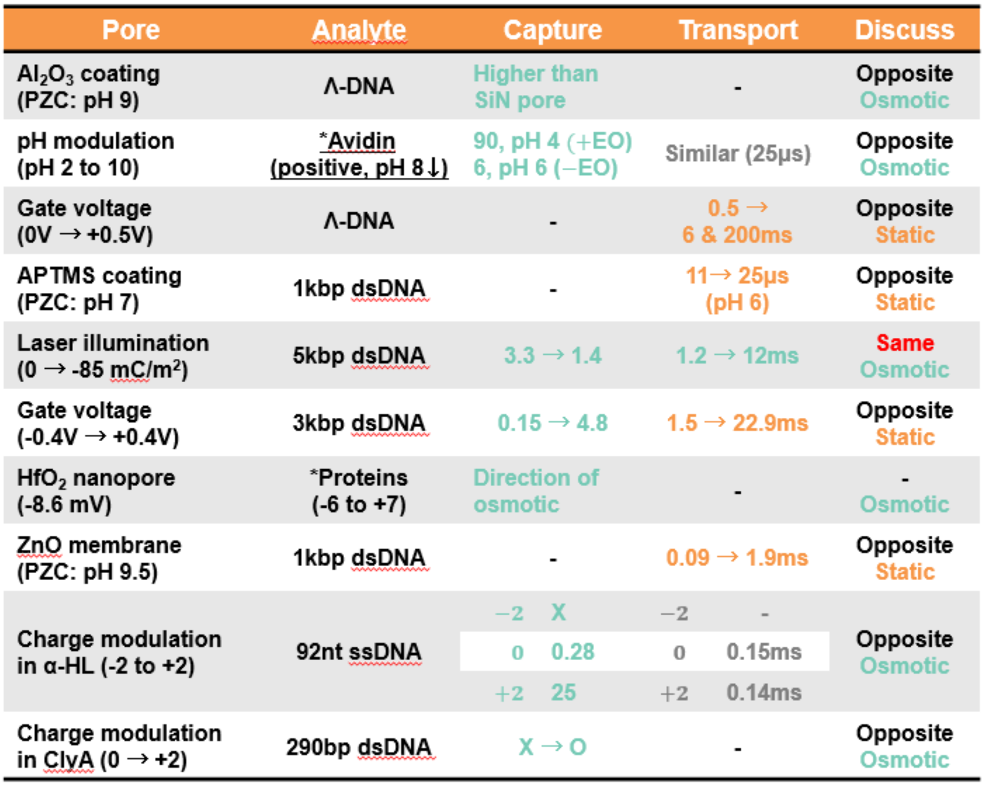

Pore	Analyte	Capture	Transport	Discuss
Al_2O_3 coating (PZC: pH 9)	Λ-DNA	Higher than SiN pore	-	Opposite Osmotic
pH modulation (pH 2 to 10)	*Avidin (positive, pH 8↓)	90, pH 4 (+EO) 6, pH 6 (−EO)	Similar (25μs)	Opposite Osmotic
Gate voltage (0V → +0.5V)	Λ-DNA	-	0.5 → 6 & 200ms	Opposite Static
APTMS coating (PZC: pH 7)	1kbp dsDNA	-	11→ 25μs (pH 6)	Opposite Static
Laser illumination (0 → -85 mC/m^2)	5kbp dsDNA	3.3 → 1.4	1.2 → 12ms	Same Osmotic
Gate voltage (-0.4V → +0.4V)	3kbp dsDNA	0.15 → 4.8	1.5 → 22.9ms	Opposite Static
HfO_2 nanopore (-8.6 mV)	*Proteins (-6 to +7)	Direction of osmotic	-	- Osmotic
ZnO membrane (PZC: pH 9.5)	1kbp dsDNA	-	0.09 → 1.9ms	Opposite Static
Charge modulation in α-HL (-2 to +2)	92nt ssDNA	−2 X 0 0.28 +2 25	−2 - 0 0.15ms +2 0.14ms	Opposite Osmotic
Charge modulation in ClyA (0 → +2)	290bp dsDNA	X → O	-	Opposite Osmotic

2.3 Our strategies for surface charge modulation

2.3.1 Laser illumination of silicon nitride nanopore

The model of optoelectronic control of surface charge density in silicon nitride nanopore was proposed in 2013 by Amit Meller's group at Boston University.[5] They suggested that electrons are excited in Si-rich defects (Si band gap: 1.1eV) in SiN membrane (Si_3N_4 band gap: 5.1 eV) by laser beam irradiation (ionization energy of visible light: 1.62 ~ 3.17 eV). The excited electrons could induce a negative surface charge (ρ) that is proportional to the laser power (P) as $\rho = \gamma P$, where γ is defined as photoreactivity. The surface charge density is inversely calculated from the surface charge term of the measured ion current, as follows (Fig. 2-5a):

$$I_{Total} = I_{bulk} + I_{DL} + I_{EOF}$$

$$I_{bulk} = \sigma \pi r^2 E_z$$

$$I_{DL} = \mu_{K+} E_z \int_0^R \rho(r) 2\pi r dr$$

$$I_{EOF} = \int_0^R v_{EOF}(r) \rho(r) 2\pi r dr$$

where I_{Total} is measured total ion current, I_{bulk} is current from the bulk electrolyte, I_{DL} is current from ions in double layer, I_{EOF} is current from electro-osmotic flow, σ is electrolyte conductivity, r is pore radius, E_z is applied electric field, μ_{K+} is mobility of counter ion (K^+) in double layer and v_{EOF} is velocity of electro-osmotic flow. The basis of this model is the following experimental results. First, a different local N/Si stoichiometry was induced in SiN nanopores by electron-beam exposure. A Si-rich stoichiometry is expected in SiN nanopores exposed to an electron beam for a long time (500 sec); they therefore exhibit higher photoreactivity (~70 C/cm^2W) than nanopores after 60-sec exposure (~27 C/cm^2W). In addition, the induced surface charge affecting DNA translocation was investigated. For instance, clogged molecules were removed by the induced negative surface charge. Electro-osmotic flow induced by a negative charge acts as a viscous drag force in the opposite direction to the electrophoretic force of DNA, making the transport speed 2 ~ 10 times slower (Fig. 2-5c), and the capture rate was reduced by half that of the minor level compared to the reduction in transport speed. This result had great impact in showing that molecular transport could be controlled at a meaningful level by adjusting the laser power.

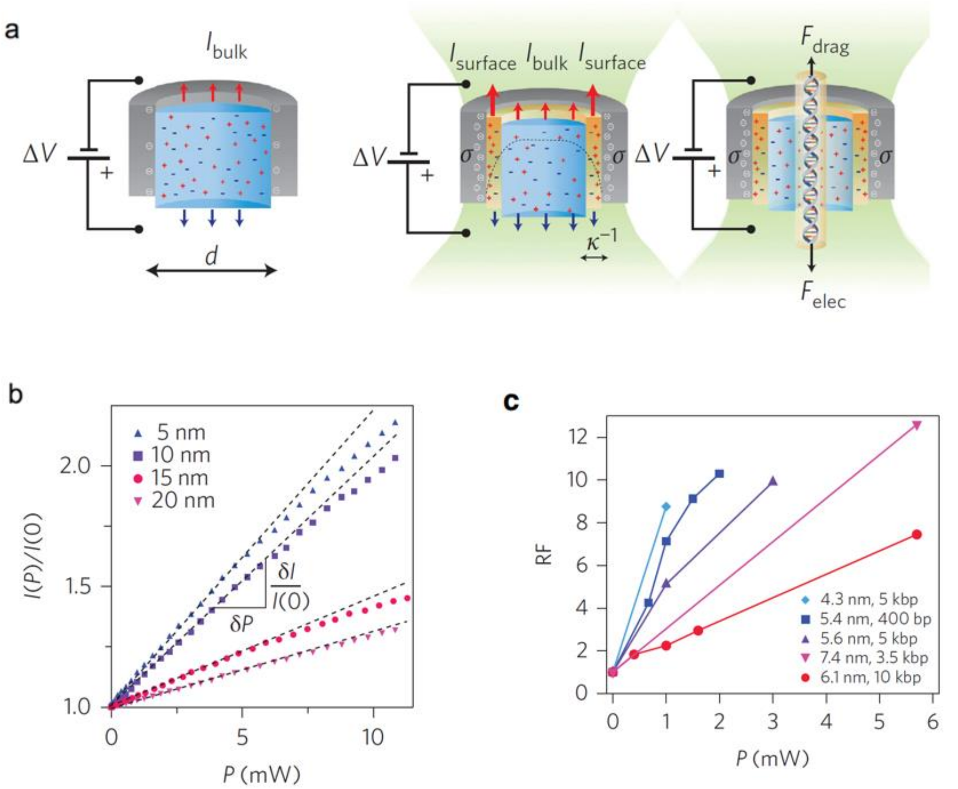

Figure 2-5 Optoelectronic control of surface charge in nanopores. (a) Schematics of light-induced modulation of ion current and DNA translocation. (b) Ion current enhancement as a function of laser power. (c) Retardation factor (RF) indicating the reduction in dwell time as a function of laser power.

2.3.2 Polymer membranes with negative surface charge

In solid-state nanopores, various surface-charge characteristics can be obtained by altering the membrane materials or coating the materials on the surface. The surface-charge characteristic of materials in an electrolyte solution is determined by adsorption of ions at the surface or protonation /deprotonation or ionization of surface chemical groups. For example, SiN exhibits a point of zero charge at pH 5, and its surface charge is determined by the reaction of surface chemical groups such as SiOH ($SiOH \leftrightarrow SiO^- + H^+$) and $SiNH_2$ ($SiNH_2 + H^+ \leftrightarrow SiNH_3^+$), depending on the solution pH. In general, when the surface is highly charged, the interaction with water will be stronger and the contact angle will decrease. However, it has been reported that hydrophobic materials such as Teflon (polytetrafluoroethylene) exhibits highly negative surface charge density.[19] Fig. 2-6 shows that SiO_2 and Teflon exhibit different relationships between surface charge and hydrophilicity.[19-21] SiO_2 exhibits a negative charge (zeta potential −30 mV at pH 7) by the OH group, and shows the most hydrophobic characteristic at pH 3, the point of zero charge. On the other hand, Teflon show the most hydrophilic characteristic at pH 3.6, its point of zero charge. In particular, Teflon has a highly negative surface charge density (zeta potential −60 mV at pH 7), even though it is composed of non-polar bonds and has no reactive surface groups. In fact, various hydrophobic polymers exhibit the point of zero charge at ~pH

3 regardless of their composition or synthesis method,[22-26] as also shown in a review paper on the measured zeta potential values of the polymers.[20] This characteristic might be attributed to the preferential adsorption of OH^- by the self-decomposition of water at the hydrophobic/solution interface for the following three reasons: 1) A strong charge appears despite few polar groups on the surface, 2) The influence of other ion concentrations on the solution is small, but the negative charge is increased by OH concentration, 3) Simulation of the high OH^- concentration at the interface (in units of Å).[27-29] The hydrophobic polymer polyurea is selected as a membrane material due to its high mechanical stability[30], chemical resistance[30], thermal stability[31], and its potential application in lithography[32]. It has been reported that polyurea has a consistent low point of zero charge (~pH 2.6) with various structures (linear or branched), compositions, and end groups (Fig. 2-7).[33]

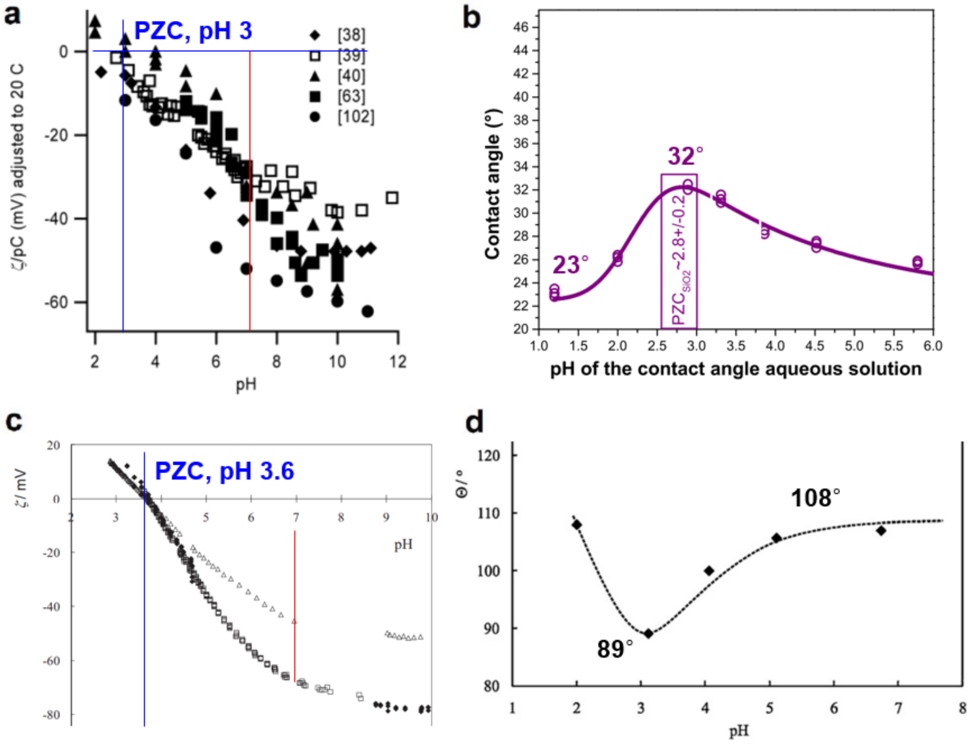

Figure 2-6 Relationship between surface charge and hydrophilicity. (a) The zeta potential of SiO_2 as a function of pH and (b) the contact angle at the corresponding pH. (c) The zeta potential of Teflon as a function of pH and (d) the contact angle at the corresponding pH. Adapted from refs. 19, 20 and 21.

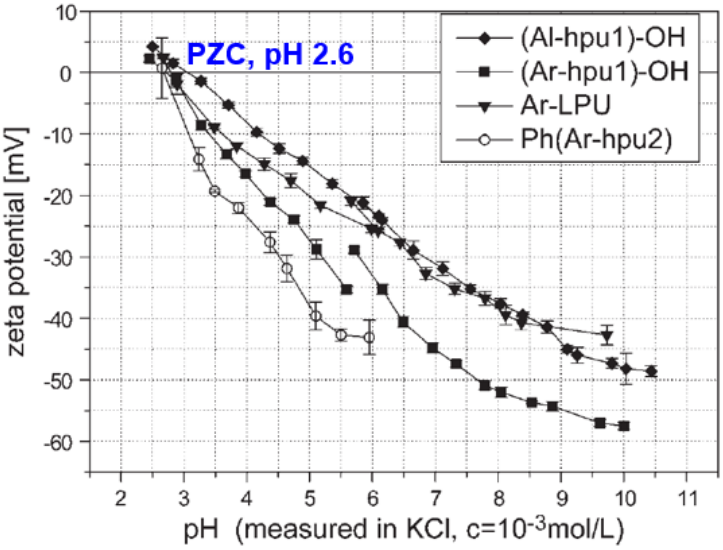

Figure 2-7 Surface charge characteristic of polyurea. The zeta potential as a function of pH for polyurea of various structures, compositions and end groups. Adapted from ref. 33.

References

1. Squires, A.; Meller, A., DNA Capture and Translocation through Nanoscale Pores—a Fine Balance of Electrophoresis and Electroosmosis. *Biophysical Journal* **2013,** *105* (3), 543-544.

2. He, Y.; Tsutsui, M.; Fan, C.; Taniguchi, M.; Kawai, T., Gate Manipulation of DNA Capture into Nanopores. *ACS Nano* **2011,** *5* (10), 8391-8397.

3. Chen, P.; Mitsui, T.; Farmer, D. B.; Golovchenko, J.; Gordon, R. G.; Branton, D., Atomic layer deposition to fine-tune the surface properties and diameters of fabricated nanopores. *Nano letters* **2004,** *4* (7), 1333-1337.

4. Firnkes, M.; Pedone, D.; Knezevic, J.; Döblinger, M.; Rant, U., Electrically facilitated translocations of proteins through silicon nitride nanopores: conjoint and competitive action of diffusion, electrophoresis, and electroosmosis. *Nano letters* **2010,** *10* (6), 2162-2167.

5. Di Fiori, N.; Squires, A.; Bar, D.; Gilboa, T.; Moustakas, T. D.; Meller, A., Optoelectronic control of surface charge and translocation dynamics in solid-state nanopores. *Nature nanotechnology* **2013,** *8* (12), 946-951.

6. Waduge, P.; Hu, R.; Bandarkar, P.; Yamazaki, H.; Cressiot, B.; Zhao, Q.; Whitford, P. C.; Wanunu, M., Nanopore-Based Measurements of Protein Size, Fluctuations, and Conformational Changes. *ACS Nano* **2017,** *11* (6), 5706-5716.

7. Ren, R.; Zhang, Y.; Nadappuram, B. P.; Akpinar, B.; Klenerman, D.; Ivanov, A. P.; Edel, J. B.; Korchev, Y., Nanopore extended field-effect transistor for selective single-molecule biosensing. *Nature Communications*

2017, *8* (1), 586.

8. Maglia, G.; Restrepo, M. R.; Mikhailova, E.; Bayley, H., Enhanced translocation of single DNA molecules through α-hemolysin nanopores by manipulation of internal charge. *Proceedings of the National Academy of Sciences* **2008,** *105* (50), 19720.

9. Franceschini, L.; Brouns, T.; Willems, K.; Carlon, E.; Maglia, G., DNA Translocation through Nanopores at Physiological Ionic Strengths Requires Precise Nanoscale Engineering. *ACS Nano* **2016,** *10* (9), 8394-8402.

10. Firnkes, M.; Pedone, D.; Knezevic, J.; Döblinger, M.; Rant, U., Electrically Facilitated Translocations of Proteins through Silicon Nitride Nanopores: Conjoint and Competitive Action of Diffusion, Electrophoresis, and Electroosmosis. *Nano Letters* **2010,** *10* (6), 2162-2167.

11. Venkatesan, B. M.; Shah, A. B.; Zuo, J.-M.; Bashir, R., DNA Sensing Using Nanocrystalline Surface-Enhanced Al2O3 Nanopore Sensors. *Advanced Functional Materials* **2010,** *20* (8), 1266-1275.

12. Park, K.-B.; Kim, H.-J.; Kang, Y.-H.; Yu, J.-S.; Chae, H.; Lee, K.; Kim, H.-M.; Kim, K.-B., Highly reliable and low-noise solid-state nanopores with an atomic layer deposited ZnO membrane on a quartz substrate. *Nanoscale* **2017,** *9* (47), 18772-18780.

13. Anderson, B. N.; Muthukumar, M.; Meller, A., pH Tuning of DNA Translocation Time through Organically Functionalized Nanopores. *ACS nano* **2013,** *7* (2), 1408-1414.

14. Kim, Y.-R.; Min, J.; Lee, I.-H.; Kim, S.; Kim, A.-G.; Kim, K.; Namkoong, K.; Ko, C., Nanopore sensor for fast label-free detection of short double-stranded DNAs. *Biosensors and Bioelectronics* **2007,** *22* (12), 2926-

2931.

15. Venkatesan, B. M.; Dorvel, B.; Yemenicioglu, S.; Watkins, N.; Petrov, I.; Bashir, R., Highly Sensitive, Mechanically Stable Nanopore Sensors for DNA Analysis. *Advanced materials (Deerfield Beach, Fla.)* **2009,** *21* (27), 2771-2776.

16. Liu, Y.; Yobas, L., Slowing DNA Translocation in a Nanofluidic Field-Effect Transistor. *ACS Nano* **2016,** *10* (4), 3985-3994.

17. Mitsuhashi, S.; Kryukov, K.; Nakagawa, S.; Takeuchi, J. S.; Shiraishi, Y.; Asano, K.; Imanishi, T., A portable system for rapid bacterial composition analysis using a nanopore-based sequencer and laptop computer. *Scientific reports* **2017,** *7* (1), 5657.

18. Tsutsui, M.; He, Y.; Furuhashi, M.; Rahong, S.; Taniguchi, M.; Kawai, T., Transverse electric field dragging of DNA in a nanochannel. *Scientific reports* **2012,** *2*, 394.

19. Preočanin, T.; Selmani, A.; Lindqvist-Reis, P.; Heberling, F.; Kallay, N.; Lützenkirchen, J., Surface charge at Teflon/aqueous solution of potassium chloride interfaces. *Colloids and Surfaces A: Physicochemical and Engineering Aspects* **2012,** *412*, 120-128.

20. Kirby, B. J.; Hasselbrink, E. F., Zeta potential of microfluidic substrates: 2. Data for polymers. *ELECTROPHORESIS* **2004,** *25* (2), 203-213.

21. Cloarec, J.-P.; Chevalier, C.; Genest, J.; Beauvais, J.; Chamas, H.; Chevolot, Y.; Baron, T.; Souifi, A., *pH driven addressing of silicon nanowires onto Si 3 N 4 /SiO 2 micro-patterned surfaces*. 2016; Vol. 27, p 295602.

22. Beneš, P.; Paulenová, M., Surface charge and adsorption properties

of polyethylene in aqueous solutions of inorganic electrolytes. *Kolloid-Zeitschrift und Zeitschrift für Polymere* **1973,** *251* (10), 766-771.

23. Möckel, D.; Staude, E.; Dal-Cin, M.; Darcovich, K.; Guiver, M., Tangential flow streaming potential measurements: Hydrodynamic cell characterization and zeta potentials of carboxylated polysulfone membranes. *Journal of Membrane Science* **1998,** *145* (2), 211-222.

24. Bismarck, A.; Kumru, M. E.; Springer, J., Characterization of Several Polymer Surfaces by Streaming Potential and Wetting Measurements: Some Reflections on Acid–Base Interactions. *Journal of Colloid and Interface Science* **1999,** *217* (2), 377-387.

25. Werner, C.; König, U.; Augsburg, A.; Arnhold, C.; Körber, H.; Zimmermann, R.; Jacobasch, H.-J., Electrokinetic surface characterization of biomedical polymers — a survey. *Colloids and Surfaces A: Physicochemical and Engineering Aspects* **1999,** *159* (2), 519-529.

26. Sze, A.; Erickson, D.; Ren, L.; Li, D., Zeta-potential measurement using the Smoluchowski equation and the slope of the current–time relationship in electroosmotic flow. *Journal of Colloid and Interface Science* **2003,** *261* (2), 402-410.

27. Beattie, J. K., The intrinsic charge on hydrophobic microfluidic substrates. *Lab on a Chip* **2006,** *6* (11), 1409-1411.

28. Kudin, K. N.; Car, R., Why Are Water−Hydrophobic Interfaces Charged? *Journal of the American Chemical Society* **2008,** *130* (12), 3915-3919.

29. Winter, B.; Faubel, M.; Vácha, R.; Jungwirth, P., Behavior of hydroxide at the water/vapor interface. *Chemical Physics Letters* **2009,** *474*

(4), 241-247.

30. Toader, G.; Rusen, E.; Teodorescu, M.; Diacon, A.; Stanescu, P. O.; Rotariu, T.; Rotariu, A., Novel polyurea polymers with enhanced mechanical properties. *Journal of Applied Polymer Science* **2016,** *133* (38).

31. Loscutoff, P. W.; Zhou, H.; Clendenning, S. B.; Bent, S. F., Formation of Organic Nanoscale Laminates and Blends by Molecular Layer Deposition. *ACS Nano* **2010,** *4* (1), 331-341.

32. Zhou, H.; Bent, S. F., Molecular Layer Deposition of Functional Thin Films for Advanced Lithographic Patterning. *ACS Applied Materials & Interfaces* **2011,** *3* (2), 505-511.

33. Abd, E. M.; Brigitte, V.; Bernd, B.; Klaus-Jochen, E.; Karina, G.; C., B., Structural and end-group effects on bulk and surface properties of hyperbranched poly(urea urethane)s. *Journal of Polymer Science Part A: Polymer Chemistry* **2005,** *43* (15), 3376-3393.

Chapter 3.

Study on photo-induced noise and surface charge for synchronized optical and electronic detection of biomolecules using nanopore

This chapter is based the paper published in

ACS Nano, (2015)

4.1 Introduction

Initially inspired by molecular transport across biological pores and the Coulter counter, the use of nanopores as single molecule sensors has come into prominence in the past two decades with a remarkable quantity of research having been published.[1] The most commonly used detection method is that of resistive pulse sensing, where analyte molecules are electrophoretically driven across an insulating membrane, separating two sides of an electrolyte, via a nanopore. Single-molecule detection is subsequently provided by the transient reduction in pore conductance from the steady-state whilst an analyte is present in the pore. Using this technique, a wide range of analytes have now been studied, most commonly single- and double-stranded DNA and proteins, with both biological and solid-state nanopores.[2–5]

Recently, the desire to acquire complementary information, increase structural resolution and analytical throughput has led to the integration of additional detection methods such as transverse electrodes and optical detection via Raman and fluorescence spectroscopy.[6–9] The integration of fluorescence spectroscopy is of particular value due to its versatility: a range of molecular properties can be probed including molecular distance (via FRET), orientation (via polarization) and local environment (via quenching).[10] In addition, the nanopore platform provides the potential to enhance optical detection via control of throughput, incorporation of additional photonic structure or use as a zero-mode waveguide.[7,11] A number of optical configurations have so far been reported, these include the use of wide-field imaging,[7] liquid core anti-resonant reflecting optical waveguides,[12] total internal reflection fluorescence microscopy[13,14] and confocal fluorescence microscopy.[7]

For structural information to be probed via resistive pulse sensing, high temporal resolution measurements are crucial due to the high translocation velocity of molecules. The most commonly used solid-state nanopore sensors consist of a silicon nitride membrane and bulk silicon substrate.[15] Unfortunately, the high frequency noise, so-called dielectric and input capacitance noise, associated with these platforms high capacitance reduces the signal bandwidth at which molecules may be detected. Although integrated measurement electronics and additional dielectric layers can reduce background noise consequently increasing operating signal bandwidth,[16,17] an additional noise source exists under laser illumination due to the presence of Si.[18] This photo-induced noise significantly limits the applicability of these platforms to high bandwidth, high laser power simultaneous optical and electronic measurements.

Here we present a unique low noise nanopore platform, composed of a predominately pyrex substrate and silicon nitride membrane as a platform for the synchronized optical and electronic detection of biomolecules.[19,20]

Pyrex's high resistivity lowers device capacitance (~5-10 pF in 1M KCl buffer) and therefore high frequency noise enabling sub-5 pA RMS ionic current measurements at 10 kHz bandwidth. Furthermore, the absence of a bulk Si substrate means photoinduced increases of RMS current are typically sub-pA in magnitude.

The application of a confocal microscope to a hybrid nanopore-zero mode waveguide platform is perhaps the most powerful technique for directly probing a single nanopore due to localised excitation volumes on the order of a zeptolitre and single photon resolution.[7,21] For this technique, a partially metallic nanopore is crucial so that no propagation modes for incident light exist within the nanopore. Using platforms coated with aluminium, we demonstrate synchronized optical and electronic detection of biomolecule translocation events. Aluminium was chosen due to its high extinction coefficient and high reflectivity at the desired wavelength (488 nm).[22] This enabled the use of membranes composed of only 30 nm thick aluminium and 20 nm thick silicon nitride, therefore providing a small nanopore volume whilst also ensuring low transmittance of light across the pore and bulk membrane. We show signal-to-noise ratios of up to 15.6 are possible for the optical detection of Yoyo-1 labelled 5 kbp DNA (7.5 base pairs to one dye molecule) within 0.1M KCl at a temporal resolution of 0.5 ms.

4.2 Experimental details

Fabrication of nanopore devices

A unique low noise nanopore platform was used in this study in order to mitigate photo-induced ionic current noise. This device is composed of a nanopore within a pyrex substrate based SiN_x (Py-SiN_x) platform instead of a typical Si substrate based SiN_x (Si-SiN_x) platform (Fig. 3-1). Silicon substrate based silicon nitride (Si-SiN_x) devices were fabricated from boron doped, <100> crystal orientation, 500 µm thick silicon wafers coated with 20 nm thick low-stress silicon nitride (SiN_x). Briefly, wafers were segmented via photolithography and reactive ion etching (RIE) into 10mm x 10 mm chips, each with a central square window of SiN_x removed. A wet KOH etch was subsequently used to establish a ~50 µm x 50 µm free standing SiN_x membrane before milling of a nanopore using a JEOL 2010F transmission electron microscope.

Pyrex substrate based silicon nitride (Py-SiN_x) devices were fabricated as follows. Pyrex substrates (10 mm x 10 mm, 200 µm thick) were coated with amorphous Si (a-Si, 200 nm thick) on both sides via low pressure chemical vapour deposition. Photolithography and RIE were used to 'open' a 5 µm x 5 µm window in *a*-Si on the topside of the wafer before a HF wet etch (49 wt. %, 5 minutes) of the exposed pyrex. Photolithography and RIE were then used to define a 100µm x 100 µm opening in *a*-Si on the bottom side of the wafer and a HF wet etch (49 wt.%) of the exposed pyrex used to merge the two etched chambers. SiN_x membranes (20 nm thick) were prepared separately via plasma-enhanced chemical vapour deposition onto a Ni-Si platform. Poly(methyl methacrylate) (PMMA, 200 nm thick) was then deposited via spin coating, yielding a PMMA/SiN_x/Ni/Si structure. Addition to a $FeCl_3$ solution dissolved the Ni present, establishing a PMMA/SiNx membrane which was added to the topside of the Py-SiN_x platform. PMMA was subsequently dissolved using acetone and the SiN_x membrane secured by depositing photodefinable PDMS (10-20 µm thick). For synchronised detection using a zero-mode waveguide modality, a 30 nm thick aluminium layer was deposited onto the topside of the Py-SiN_x platform (Py-SiN_x-Al) via electron beam evaporation before deposition of PDMS.

Measurement set-up

Simultaneous optical and electrical measurements were enabled by mounting nanopore devices in an optical cell, using a coverslip as a base. This enabled illumination of the nanopore using a custom-built confocal microscope (Fig. 3-2).[23] Nanopores were illuminated using a 488 nm continuous-wave solid-state laser (Sapphire 488LP, Coherent) and a 60x water immersion objective (1.20 NA, UPLSAPO 60XW, UIS2, Olympus). Fluorescence emission was split into two bands, 500-580 nm and 640-800 nm, using a dichroic mirror (630DCXR) before detection by two avalanche photodiodes (SPCM-AQR-14, Perkin-Elmer) coupled with a DAQ card (NI 6602, National Instruments) for data logging. A transmembrane potential was applied to nanopore sensors using an A-M systems 2400 patch-clamp amplifier and Ag/AgCl electrodes. Unless otherwise stated, the analogue signal was filtered by an integrated 6 position, four pole low pass Bessel filter at 10 kHz before digitization at 100 kHz using a NI-USB 6259 DAQ card. All electrolytes were buffered using 10mM Tris.HCl, 1mM EDTA (pH7).

Custom Matlab scripts were used for data analysis. Power spectrums were estimated, using a fast-fourier transform and 9.75 s duration data sets. To rectify signal attenuation before the cut-off frequency, power spectrums were normalised by the magnitude response of a four-pole low pass Bessel filter at the corresponding low pass filter frequency. RMS current was calculated using 0.2 s ionic current traces. Peak selection criteria for both optical and electrical translocation data was a minimum amplitude of 5 standard deviations of the background signal. To account for ionic current noise, the baseline of all electrical data was smoothed using an asymmetric least squares smoothing algorithm before peak selection.

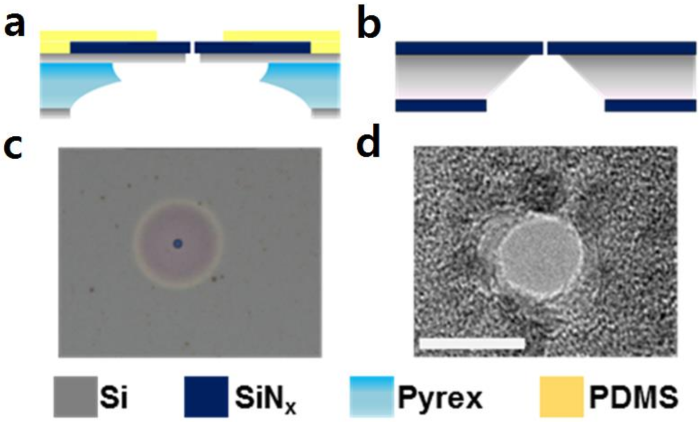

Figure 3-1. Schematics of (a) Si and (b) Pyrex substrate based silicon nitride nanopore platforms. (c) Optical image of a Pyrex substrate (Py-SiN_x) platform (scale bar = 10 µm). Two circular features are present. The larger feature (diameter: ~19 µm) corresponds to the aperture within the pyrex substrate and the smaller feature (diameter: ~2.1 µm) to the free standing silicon nitride membrane. (d) TEM image of a 7 nm diameter nanopore within the free-standing silicon nitride membrane of a Py-SiN_x platform (scale bar = 10 nm).

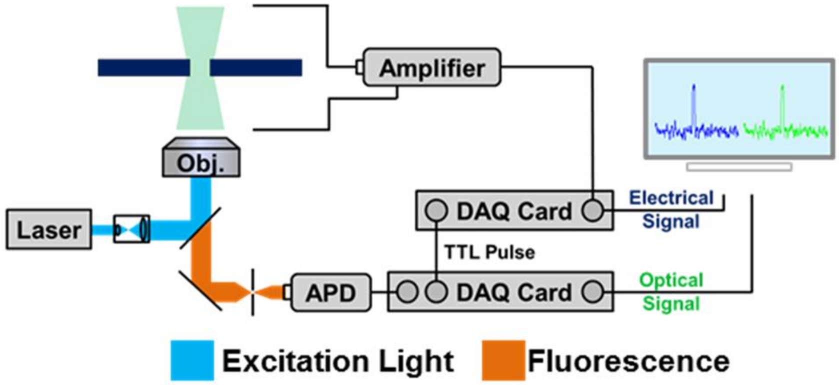

Figure 3-2. The experimental set-up: an epifluorescence optical configuration employing a 488 nm continuous-wave laser; a 60x water immersion objective (Obj.) and avalanche photodiode (APD) is used to probe a SiN_x nanopore (Materials and Methods). When electrical data acquisition is initiated, a TTL pulse is generated by the electrical data acquisition (DAQ) card which subsequently triggers optical acquisition.

4.3 Results and discussion

4.3.1 Photo-induced noise and surface charge

A pyrex substrate based SiN$_x$ (Py-SiN$_x$) platform and a typical Si substrate based SiN$_x$ (Si-SiN$_x$) platform were fabricated so that their photoinduced noise characteristics could be compared within a typical 0.1 M KCl electrolyte. As a result of Pyrex’s high resistivity (400 MΩ m), Py-SiN$_x$ platforms have lower capacitance (~5-10 pF in 1M KCl buffer) and therefore exhibit lower dielectric and input capacitance noise than Si-SiN$_x$ platforms (Boron doped, Si substrate resistivity: 1-30 Ω cm).[24] Consequently, with the laser turned off, the level of electrical noise for Py-SiN$_x$ platforms was lower than that for Si-SiN$_x$ platforms. For example, the standard deviation of ionic current at 0 mV bias, with the laser turned off, for a ~27 nm diameter nanopore was only 4.02 ± 0.02 pA for a Py-SiN$_x$ platform compared to 26.9 ± 0.9 pA for a Si-SiN$_x$ platform. Furthermore, bypassing the low pass Bessel filter integrated within the amplifier, a Py-SiN$_x$ platform provides a standard deviation of only 6.74 pA at 0 mV bias. As the dimensions of these pores are similar, they will exhibit comparable thermal noise.[24] Hence, the low noise exhibited by the Py-SiN$_x$ platform is a direct consequence of it low capacitance. There is also a substantial difference in the response of the devices to laser illumination. Fig. 3-3a shows the baseline ionic current at 0 mV bias for a nanopore within a Py-SiN$_x$ and Si-SiN$_x$

platform, as laser power is raised to ~580 µW in magnitude. Assuming a cylindrical geometry, the pores have an approximate diameter of 27 nm based on the measured pore conductance (Py-SiN$_x$ conductance: 25.5 nS, Si-SiN$_x$ conductance: 25.4 nS).[1] The standard deviation of the ionic current standard increases by 780.1 ± 25.8 pA (2864.2 ± 95.1%) for the Si-SiN$_x$ platform compared to only 0.9 ± 0.1 pA (17.6 ± 1.4%) for the Py-SiN$_x$ platform (Fig. 3-4). Fig. 3-3b and c show power spectrum densities (PSDs) for both platforms with the laser off and at ~580 µW laser power. Interestingly, a broad peak centred at ~225 Hz exists at ~580 µW laser power for the Si-SiN$_x$ platform. Both photo-induced heating of the electrolyte and surface charge change for silicon nitride nanopores have previously been reported.[25,26] However, the frequency dependence of this noise source is inconsistent with that of surface charge protonation noise or temperature dependant thermal and dielectric noise.[24,27] Furthermore, this peaks absence within the Py-SiN$_x$ platforms power spectrum suggests the source of noise is related to the Si substrate. The optical transparency of the SiN$_x$ membrane and photon energy (2.54 eV) is sufficient for electron-hole pair generation in the Si substrate (band gap ~1.1 eV), reported to promote photoreduction of H^+ at p-type Si interfaces.[28] We therefore suspect, as previously reported, that the increase in noise is via electrochemical reaction at the silicon-electrolyte interface.[18]

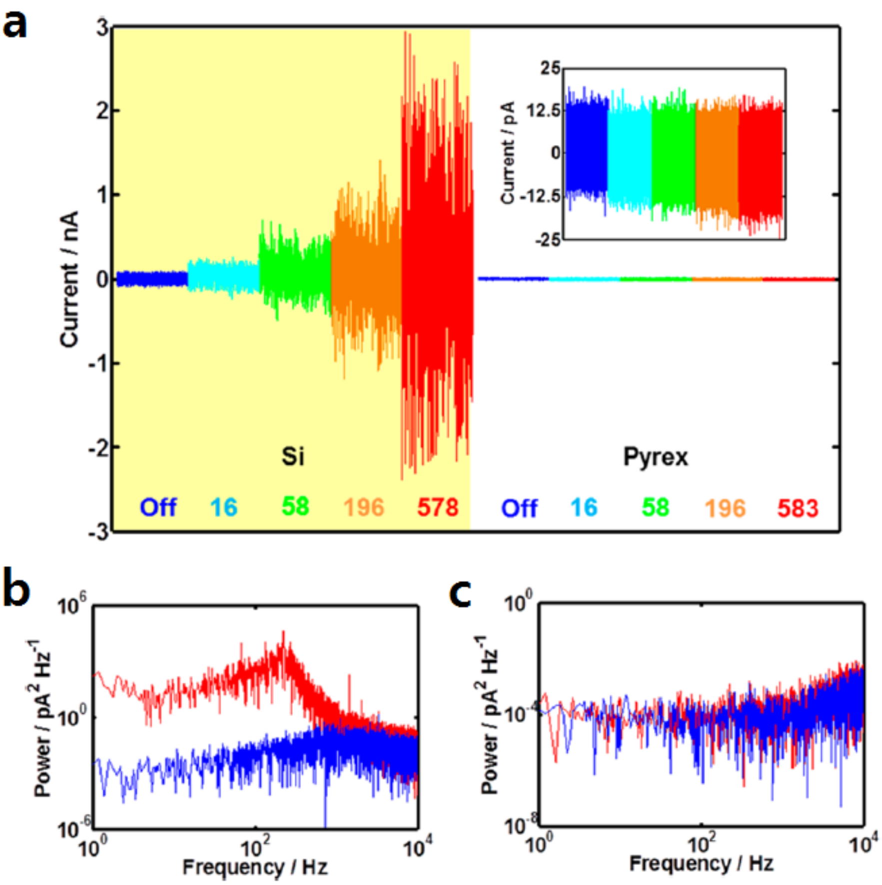

Figure 3-3. (a) Baseline ionic current at 0 mV, under laser illumination, for a ~27 nm diameter nanopore in a Si-SiN$_x$ (yellow background) and Py-SiN$_x$ platform. Different colour traces correspond to different laser powers, as indicated by the number (in µW units) beneath each trace. The inset is an expanded view of data for the Py-SiN$_x$ device. (b) Power Spectral Densities at 0mV for the Si-SiN$_x$ platform with the laser off (blue) and at ~578 µW laser power (red). (c) Power Spectral Densities at 0mV for the Py-SiN$_x$ platform with the laser off (blue) and at ~583 µW laser power (red).

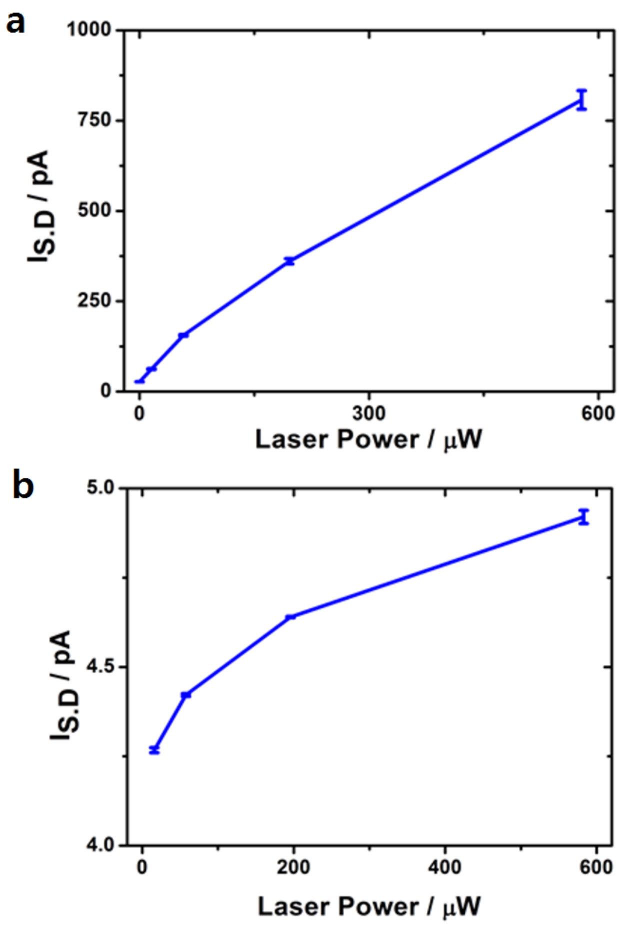

fig

Figure 3-4. Standard deviation of ionic current as a function of laser power, at 0 mV bias, for a ~27 nm diameter nanopore within a A) Si-SiN (conductance: 25.4 nS) and B) Py-SiN platform (conductance: 25.5 nS). Data collected using a 0.1M KCl, 10mM Tris.HCl, 1mM EDTA (pH 7) buffer.

The small increase of noise for Py-SiN$_x$ platforms stems from an increase in pore conductance with laser illumination and is a result of flicker noise scaling with the square of the ionic current and thermal noise being directly proportional to pore conductance.[24,29] Fig. 3-4a shows current-voltage characteristics and corresponding conductance's at 0 mV bias for a ~7 nm diameter pore (conductance: 4.0 nS at 0 mV) at laser powers up to ~596 μW. Increases in noise for this nanopore are minor: sub-pA at 0mV, 100mV and 200mV bias across the entire laser power range (Figure 3-5b). The linear scaling of pore conductance with laser power may be a result of increases in pore surface charge and local heating of the electrolyte.[25,26] Previous studies suggest temperature change is likely to be small. For instance, the absorption coefficient of water for 488 nm wavelength light (0.0144 m^{-1}) is significantly lower than for 1064 nm wavelength light (12 m^{-1}) which has been reported to increase temperature at a rate of 20 K per mW.[26,30] Furthermore, introduction and translocation of 5 kbp DNA (0.75 nM), using this nanopore, revealed a reduction of translocation frequency by 25.8 ± 1.5% and 60.4 ± 5.6% at ~74 μW and ~204 μW laser power respectively (Fig. 3-6). An increase in surface charge is expected to reduce translocation frequency due to higher electro-osmotic flow, whilst the opposite trend is expected from local heating due to lower solution viscosity.[25,31–33] These findings suggest that increases in surface charge are the primary source of conductance change.

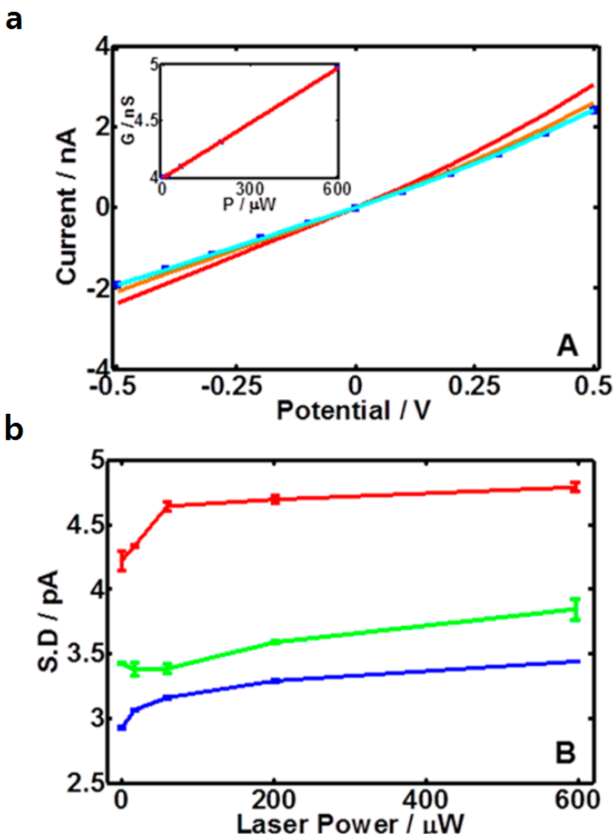

Figure 1-5. (a) Current–Voltage trace for a ~7 nm diameter (conductance: 4.0 nS at 0 mV) Py-SiN$_x$ nanopore with the laser off (blue) and at ~17 µW (blue), ~201 µW (orange) and ~596 µW (red) power. The inset shows pore conductance at 0 mV as a function of laser power. (b) Standard deviation of ionic current versus laser power with a bias of 0mV (blue), -100mV (green) and -200mV (red).

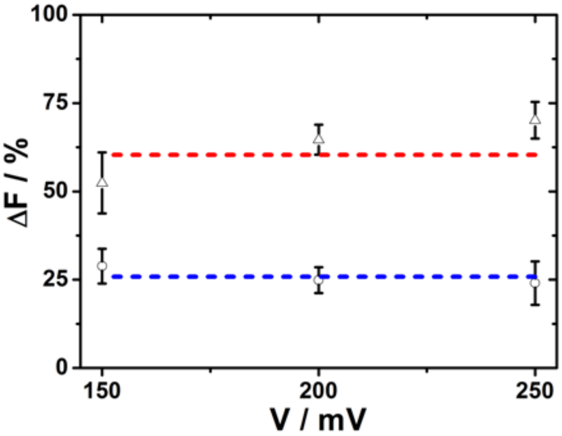

Figure 3-6. The relative reduction in translocation frequency of 5 kbp DNA at ~74 µW (O) and ~204 µW (Δ) laser power, w.r.t. the translocation frequency with the laser off. Fits reveal an average reduction of 25.8 ± 1.5% and 60.4 ± 5.6% at ~74 µW and ~204 µW laser power respectively. Data collected using a ~7 nm diameter pore (conductance: 4.0 nS at 0 mV) and a 0.1M KCl, 10mM Tris.HCl, 1mM EDTA (pH 7) buffer.

By assuming changes in pore conductance were due to an increase in surface charge density alone, an expression which provided conductance as a function of laser power was derived and fit to the inset within Fig. 3-5a. At first, the conductance of a cylindrical nanopore can be approximated in high ionic strength solutions (>100mM) using equation 1 which accounts for contributions from bulk conductance, access resistance and electro-osmosis.[1] Next, based on the experimental observation that pore conductance increases linearly with laser power, similar to Di Fiori *et al*, we approximate that surface charge density is related to laser power via expression 2, where the photoreactivity (γ) describes the rate of change of surface charge with laser illumination.[25] Combining equations 1 and 2 provides equation 3, which describes pore conductance as a function of laser power. This expression was fit to the inset of Figure 3A in the main text to deduce the photoreactivity (γ) and initial surface charge density (σ_{initial}). To reduce the number of fitting parameters, the electrophoretic mobility of K^+ within the double layer was assumed to be equal to that reported in free solution (7.616×10^{-8} m^2 V^{-1}s^{-1}), whilst the diameter and length were fixed at 20 nm and 7 nm respectively.[3] This value of pore diameter was estimated from transmission electron microscopy images taken after fabrication.

$$(1)\ G = \sigma_S \frac{1}{\left(\left(\frac{4L}{\pi d^2}\right) + \left(\frac{1}{d}\right)\right)} + \pi \frac{d}{L} \mu_K \sigma_{surf}$$

$$(2)\ \sigma_{surf} = \sigma_{initial} + \gamma P$$

$$(3)\ G = \sigma_S \frac{1}{\left(\left(\frac{4L}{\pi d^2}\right) + \left(\frac{1}{d}\right)\right)} + \pi \frac{d}{L} \mu_K \sigma_{initial} + \pi \frac{d}{L} \mu_K \gamma P$$

Where d is pore diameter (m); L is pore length (m); σ_s is solution conductivity (S m^{-1}); σ_{surf} is surface charge density (C m^{-2}); μ_k is electrophoretic mobility of potassium in the double layer (m^2 $V^{-1}s^{-1}$); initial is surface charge density with the laser off (C m^{-2}); γ is the photoreactivity (C m^{-2} W^{-1}) and P is laser power (W). This expression provided an estimate of 27.9 mC m^{-2} for the surface charge density with the laser turned off and and 20.0 C m^{-2} W^{-1} for the rate of change of surface charge. Both values are in good agreement with literature.[25,27]

PSDs of the ionic current at 200 mV and 0 mV bias were fit with $S_n(f) = Af^{-\alpha}$ and $S_n(f) = B + Cf + Df^2$, respectively, where f is frequency; A is the amplitude of flicker noise; B of white (thermal) noise; C of dielectric noise and D of input capacitance noise (Fig. 3-7).[24,34] As expected, this analysis revealed an increase in the amplitude of both flicker noise and white (thermal) noise with laser power (Fig. 3-8). Due to dielectric and input capacitance noise's dependence on frequency ($\propto$ F and $\propto$ F^2 respectively), for these power spectrum analysis was conducted on ionic current data low pass filtered at 20 kHz to increase the fitting range and certainty of extracted parameters. No significant dependence of the amplitude of either dielectric or input capacitance noise on laser power was found (Fig. 3-9).

Increases in the amplitude of thermal noise (B) are in line with conductance changes as predicted using a thermal noise model, $B=4k_BTG$, where T is temperature and G pore conductance. For instance, at ~596 µW laser power the amplitude of thermal noise increased by 35.0 ± 9.1% and pore conductance increased by 25 % (Fig. 3-4a, inset). At ~596 µW laser power, the amplitude of flicker noise increased by 87.0 ± 45.4 % (Fig. 3-7). The amplitude of flicker noise is known to scale with the square of the ionic current (i.e. $A \propto I^2$).[24,35] The noise amplitude once normalised w.r.t. I^2 is approximately constant across the laser power range with a mean of $3.56 \pm 0.17 \times 10^{-7}$ Hz^{-1} (Fig. 3-8, inset). This implies that the rise in amplitude of flicker noise occurs due to the increase in magnitude of the current.

Previous studies have shown that nanopores which exhibit low flicker noise (<1 pA^2 / Hz at 1 Hz) may be described by Hooges relation, which characterizes flicker noise arising from fluctuations in bulk electrolyte mobility.[17] In such cases, the flicker noise amplitude (A) is given by $A = aI^2/f$, where I is current; f is frequency and a is the normalised noise amplitude. The normalised noise amplitude is given by $a=\alpha/N_c$ where N_c is the number of charge carriers and α is the Hooge parameter.[35–37] Upon illumination of a nanopore, the surface charge density increases and hence so does the number of charge carriers. If the Hooge relation is obeyed, the normalised noise amplitude (a) would therefore decrease with laser power. The independence of the normalised flicker noise amplitude to laser power therefore suggests that mobility fluctuations are not the sole mechanism responsible for flicker noise in this system. A variety of additional flicker noise sources have been reported, including nanobubbles and inhomogeneous surface charge, which could be present simultaneously.[17,38,39]

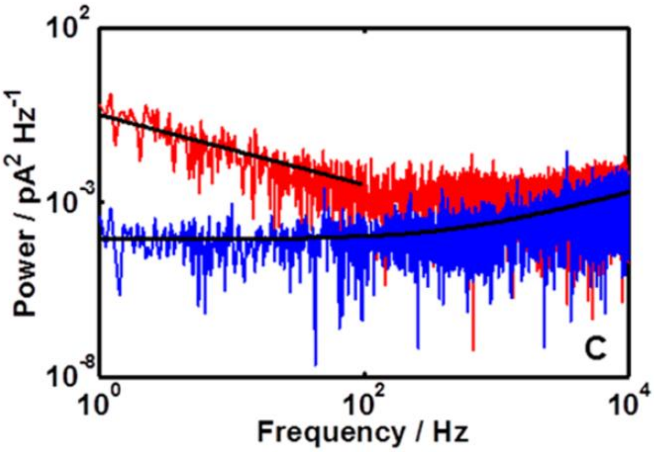

Fig. 3-7 Power Spectral Densities at 0 mV (blue) & -200mV (red) with the laser power at ~596 μW. Black lines indicate fits of $S(f) = Af^{-\alpha-}$ and $S(f) = B + Cf + Df^2$ (where A–D are fitting parameters and $0 < \alpha < 2$, with exponent α typically close to 1) for data collected at -200mV and 0mV respectively.

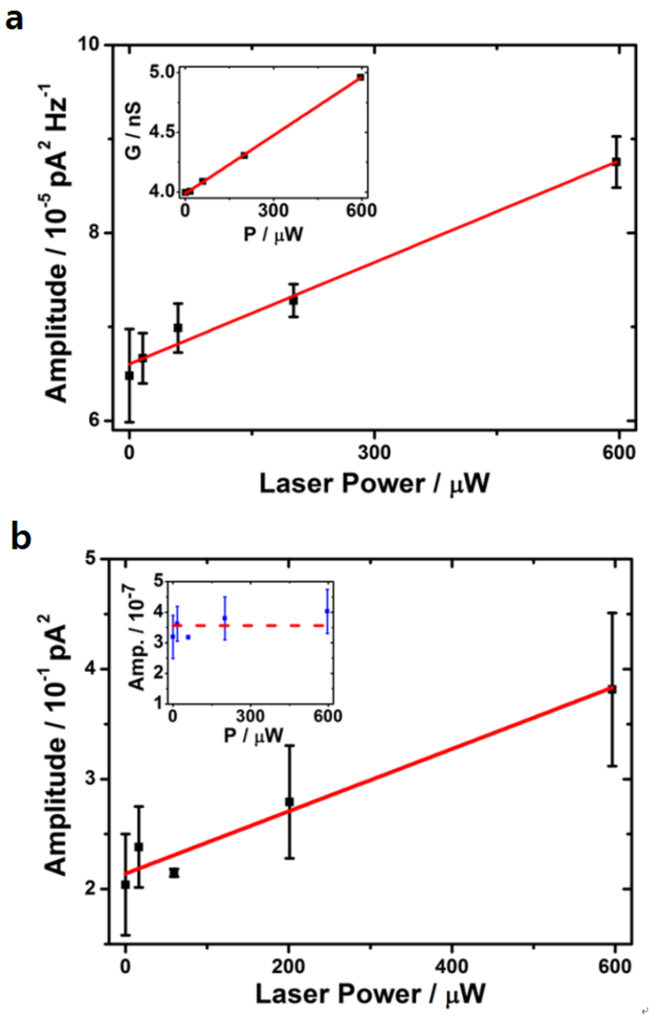

Figure 3-8. Dependence of (a) Thermal and (b) Flicker noise on laser power. The inset of panel (a) shows pore conductance at 0 mV and (b) the normalised flicker noise amplitude (w.r.t. $<I>^2$) as a function of laser power. Data collected using a ~7 nm diameter pore (conductance: 4.0 nS at 0 mV) and 0.1M KCl, 10mM Tris.HCl, 1mM EDTA (pH 7) buffer.

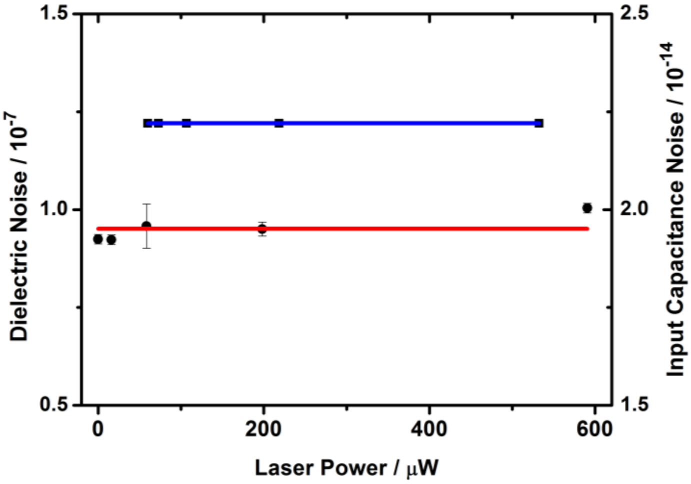

Figure 3-9. Dependence of dielectric and input capacitance noise on laser power. The average amplitude of dielectric noise and input capacitance noise are $2.22\times10^{-14} \pm 1.14\times10^{-20}$ and $9.51\times10^{-8} \pm 1.75\times10^{-9}$ respectively. The data was collected using an ~10 nm diameter pore (conductance: 6.8 nS), 0.1M KCl, 10mM Tris.HCl, 1mM EDTA (pH 7) buffer and was low pass filtered at 20 kHz.

For Si-SiN_x platforms, the broad peak at ~225 Hz within PSDs, associated with photo-induced electrochemical reaction, prevented the same procedure of analysis. Nonetheless, visual inspection of Fig. 3-5b shows a substantial increase in the amplitude of noise below 1000 Hz at ~578 µW laser power and 0 mV bias. Use of a smoothing spline indicated an increase in the amplitude of noise at 225 Hz and 1 Hz by factors of $1.79 \pm 0.17 \times 10^5$ and $7.74 \pm 2.56 \times 10^4$, respectively. These noise characteristics are in stark contrast to Py-SiN_x devices. For comparative purposes, the same analysis was conducted on Fig. 3-7 as it was collected with a similar sized (~ 27 nm diameter) Py-SiN_x nanopore. Here, illumination with ~583 µW laser power induced an increase by a factor of only 1.48 ± 0.05 and 1.49 ± 0.06 at 1 Hz and 225 Hz, respectively. Fig. 3-10 contains PSDs for both devices, normalised w.r.t. I^2, at -200 mV bias with the laser turned off and on. For this Si-SiN_x nanopore, at ~578 µW laser power the magnitude and breadth of the peak at ~225 Hz is great enough to obscure flicker noise. Whereas for the Py-SiN_x platform, as previously discussed, increases of low frequency noise are in accordance with the growth of flicker noise associated with higher ionic current. Comparison of these PSDs highlights the significance of the additional source of noise for Si-SiN_x platforms. In addition, it shows the distinct improvement a predominately pyrex substrate provides: ionic current measurements at a noise floor defined by the magnitude of conductance change induced by laser illumination.

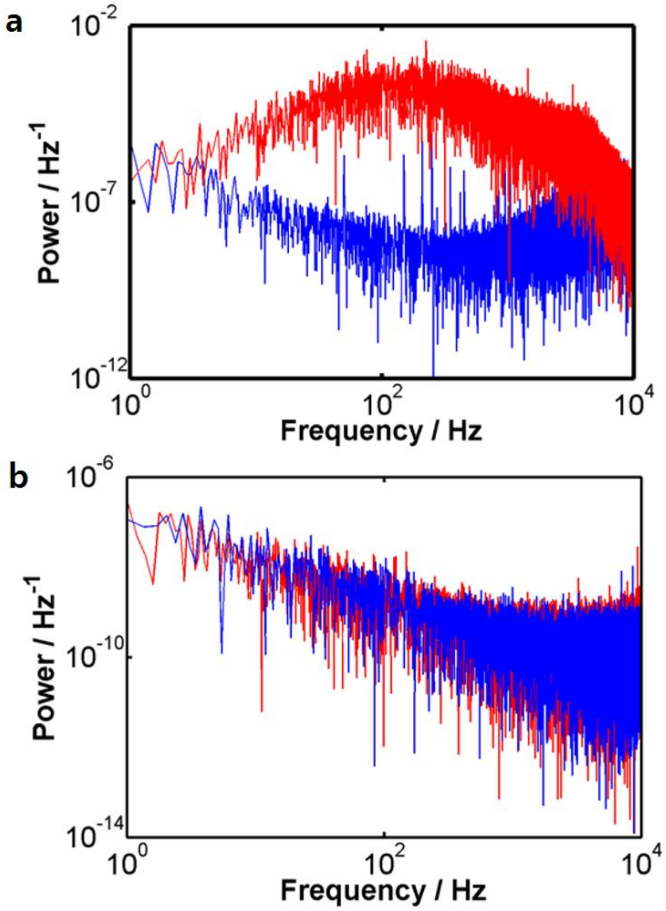

Figure 3-10. Power spectral densities at -200 mV, normalised with respect to the square of the ionic current, for a ~27 nm diameter nanopore in a Si-SiN$_x$ and Py-SiN$_x$ platform. (a) Power Spectral Densities for the Si-SiN$_x$ platform with the laser off (blue) and at ~578 μW power (red). (b) Power spectral densities for the Py-SiN$_x$ platform with the laser off (blue) and at ~583 μW power (red).

4.3.2 Independent optical and electronic detection

The low light induced noise of Py-SiN_x nanopore devices make them ideal for utilisation with confocal microscopy for synchronised optical and electronic detection of biomolecules. Previous studies have demonstrated the advantages of a hybrid nanopore-zero-mode waveguide platform: reduced background photon noise, the ability to precisely localise a molecule within the optical probe volume and control of throughput.[7,40] This powerful technique involves illumination of a partially metallic nanopore where, crucially, the lateral dimensions of the nanopore mean no propagation modes exist for the incident light. As a result, light inside the aperture decays evanescently resulting in confined excitation volumes on the order of a zeptolitre (1×10^{-21}). It is important pore length is not increased substantially by a metallic layer, as changes in pore conductance induced by a translocating molecule are inversely proportional to pore length.[41] Thus Py-SiN_x platforms were coated with 30 nm thick aluminium via electron beam evaporation before milling of a sub-30 nm diameter pore. This structure was selected as it provided a small nanopore volume whilst also ensuring low transmittance of light across the pore and bulk membrane. Transmittance of light across the bulk membrane is significantly attenuated, with a reduction in the electromagnetic field intensity across a 30 nm thick Al membrane of ~20 dB ($10\log_{10}|E|^2$).[22] Furthermore, at the wavelength of interest (488 nm), the ZMW cut-off diameter is 215 nm ensuring attenuation of light intensity along the pore-axis.[22] Assuming the ZMW was fabricated using a perfect conductor, the intensity of light decays according to the below expression where h is pore depth, I_h is intensity at depth h, I_o is initial intensity, λ_c is the cut-off wavelength and λ_m is the wavelength of incident light.[42]Using this equation, a reduction of intensity by 99.6 % is expected at a depth of 5 nm within a 10 nm diameter pore. It should be noted that this only an estimate as attenuation is lower for real metals, due to a finite skin depth.[43]

$$\frac{I_h}{I_o} = exp\left(-\frac{4\pi h}{\lambda_b}\sqrt{\left(\frac{\lambda_m}{\lambda_c}\right)^2 - 1}\right)$$

Before attempting synchronised detection, independent optical and electronic measurements of the translocation of 5kbp DNA were conducted to assess the viability of this platform for single molecule detection. Excellent signal-to-noise for both electronic and optical signals was provided by these nanopore platforms. Fig. 3-11a shows a typical ionic current trace for a ~19 nm diameter nanopore (conductance: 49.6 nS) within a 1M KCl electrolyte, after introduction of 5 kbp DNA (2.6 nM) and application of a 100 mV bias. Corresponding event durations and amplitudes were extracted and are shown by a contour plot in Fig 3-11b. Translocation events of linear and folded DNA molecules are easily distinguished and are labelled as type 1 and 2 events respectively.[3]

For optical detection, DNA was labelled with Yoyo-1 at ratio of 7.5 base pairs to one dye molecule. Yoyo®-1 was selected as its absorbance maximum (491 nm) is close to the wavelength of the laser (488 nm). The fluorescence of Yoyo®-1 is quenched by chloride ions, however a 0.1M KCl electrolyte provided good signal-to-noise with this binding ratio. Figure 4C shows an example optical trace for 500-580 nm wavelength fluorescence at 300 mV bias and ~17 μW laser power illumination, after the introduction of labelled DNA (0.85 nM) to a 30 nm diameter pore (conductance: 25.7 nS). The presence of a translocating DNA molecule within the optical probe volume results in a burst of fluorescence. Corresponding dwell times and event amplitudes were extracted, using a custom Matlab script, and are shown within a contour plot in Fig. 3-11d. Signal-to-noise is excellent: the ratio of mean pulse height (28.5 ± 11.6 photons per 0.5 ms) to background photon counts (1.85 ± 0.65 photons per 0.5 ms) is 15.6 ± 8.3. The dwell time within the optical channel is larger than that would be expected in the electronic channel. A fit of a log-normal probability distribution function to a histogram of event duration provided a mean of 78.3 ± 3.9 ms. This is a result of a molecule which has left the nanopore being detected optically until it has left the focal plane via a combination of diffusion and electrokinetic phenomena.[7]

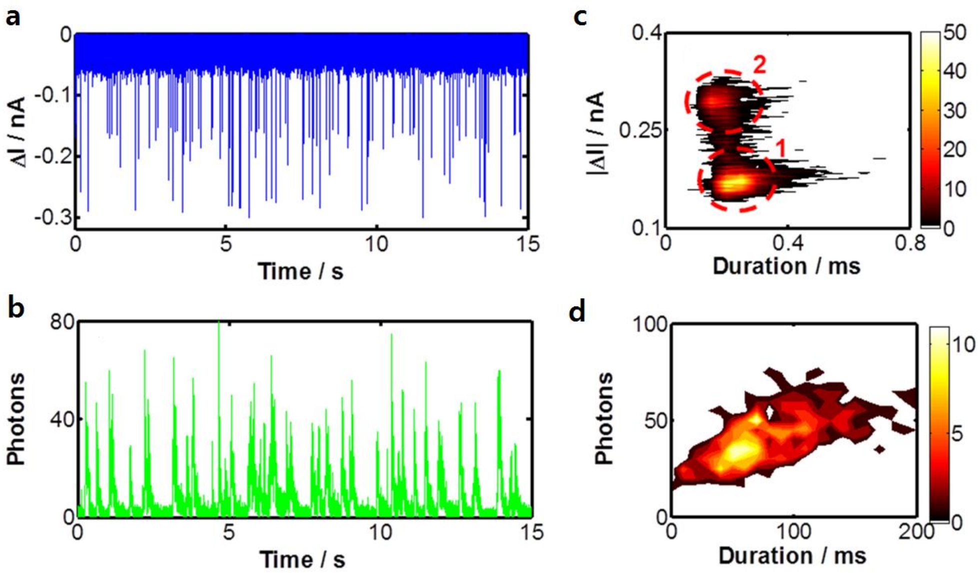

Figure 3-11. (a) Baseline-adjusted ionic current trace for electrical 5 kbp DNA translocation detection at 100 mV using a ~19 nm diameter pore (conductance: 49.6 nS) and 1M KCl electrolyte. (b) Corresponding contour plot of event amplitude versus duration for 100 mV electrical detection data. (c) Photon trace (0.5 ms resolution) for optical Yoyo®-1 labelled 5 kbp DNA (7.5bp's : 1 dye) translocation detection at 300 mV bias and ~17 μW laser power using a 30 nm diameter pore (conductance: 25.7 nS) and 0.1 M KCl electrolyte. Data corresponds to 500-580 nm wavelength fluorescence. (d) Corresponding contour plot of event amplitude (photons per 0.5ms) versus duration for 300 mV optical detection data.

4.3.2 Synchronized detection

Synchronised optical and electrical data acquisition was enabled through the use of hardware and a custom LabView program for optical data acquisition. Synchronization of optical and electrical signals was verified by illuminating a ~14 nm diameter nanopore (conductance: 9.1 nS) with 1.87 mW laser power in finite intervals using an optical beam shutter (Thorlabs, SHO5). Photo-induced increases in pore conductance were correlated with an increase of background fluorescence from the pore surface, detected within the red channel of the optical set-up (λ~ 640- 800 nm). Cross-correlation of the two signals was conducted, for a total of 14 pulses, to quantify any delay in acquisition. This indicated that the electronic signal trailed the optical signal by an average of 0.18 ± 0.02 ms (Fig. 3-12). This delay is close to the difference in rise-time of the two signals, 0.17 ± 0.08 ms, indicating that data acquisition was indeed synchronized.

To demonstrate synchronised detection, we introduced Yoyo-1 labelled 5kbp DNA (0.790 nM) to a platform containing two pores (~10 nm and ~6 nm diameter, total conductance: 9.1 nS). Fig. 3-12 shows a sample of the recorded ionic current (I (t)) and optical fluorescence (F (t)) signals at ~16 µW laser power and -400 mV applied bias. A total of 191 events were detected in the optical channel and 206 events in the electronic channel: a 92.7% synchronized detection efficiency. The slightly lower quantity of events in the optical channel is in part due to the longer dwell time of DNA within the optical detection volume (mean duration: 152.0 ± 23.0 ms, Fig. 12d) resulting in amalgamation of consecutive translocation events. Accounting for such events provides an efficiency of 93.7%. Efficiency could be improved further by using an alternate fluorescent dye, for example Alexa Fluor 488 as its fluorescence is not quenched by halides, this was deemed unnecessary for this proof of principle experiment.

Interestingly, an increase in ionic current upon exit of a DNA molecule from the pore is observed in 77.7% of events (160 events). This phenomenon was also observed for Py-SiN_x platforms which contained a single nanopore, with and without Al (data not shown). Resistive pulses are a result of a decrease in the flux of ions across the pore and consequently pore conductance whilst a molecule is present. The mechanism responsible for a peak in ionic current (mean duration: 0.08 ± 0.03 ms, mean amplitude: 197.0 ± 37.9 pA) is less clear. If the diameter of the nanopore is close to that of dsDNA (2.2 nm) and its double layer ($\lambda_D = 0.97$ nm for 0.1M KCl), this phenomenon can arise due to the release of accumulated electrolyte ions at the pore entrance after translocation and analyte double layer effects such as diffusive currents and concentration polarisation.[44–46] However, the nanopore dimensions (~10 nm and ~6 nm) are larger than that of a single DNA molecule and hence these mechanisms are unlikely to be significant. Instead, we suspect this peak in ionic current arises from electrostatic enhancement of counter-ion concentration at the pore exit due to molecule surface charge.[47] Menestrina *et al* have previously reported a decrease and subsequent increase in current upon entry and exit of negatively charged 410 nm diameter PMMA particles across a 1400 nm diameter pore for electrolyte concentrations <200mM KCl.[47] We believe that the peak in ionic current arises predominately due to this mechanism. We are not fully certain why this phenomenon is only observed in 77.7 % of events, but this may be a consequence of differing conformations of DNA upon leaving the pore.

A histogram of resistive pulse height revealed a single cluster of events with a mean amplitude of 196.4 ± 67.8 pA (Fig. 3-13c, inset). The corresponding molecule diameter was estimated, neglecting surface charge effects, using the expression derived by Smeets *et al* as 4.57 ± 1.41 nm.[41] This indicates that molecules translocated predominately in a folded conformation. A histogram of the resistive pulse duration, shown in figure 5b, was fit with the 1D linear translocation probability density function reported by Ling *et al*,

$$\mathrm{F1(t)} = \left(\frac{\mathrm{L}}{4\pi \mathrm{D} t^3}\right) 1/2 e^{-\frac{(L-vt)2}{4Dt}},$$

where v is drift velocity, L is the length of 5kbp dsDNA and D is the diffusion coefficient.[48] The length of unfolded 5 kbp DNA is 1.7 µm; the Ling distribution indicated a molecule length of 1.064 µm confirming that molecules were folded during translocation. The mean translocation time and drift velocity were 0.283 ms and 3.76 mm/s, which are in good agreement with literature.[3,15]

Synchronization was verified via cross-correlation of the optical and electrical signals. Due to the irregular shape and long duration of optical events, they were replaced with pulses with the same duration as the corresponding electrical event. As a high proportion of electrical events were biphasic, the optical signal was cross-correlated with both resistive pulses and peaks in ionic current. Cross-correlation indicated that molecules were detected optically 80 µs after the resistive pulse and 109 µs before the peak in ionic current associated with exit from the pore. Figure 3-14 shows cross-correlation of the optical events and the associated peaks in ionic current for the data set shown in Figures 3-13. The delay in optical detection with respect to the initial resistive pulse indicates that, due to the evanescent decay of incident light along the pore axes, the effective optical observation volume is indeed confined to the far region of the pore.

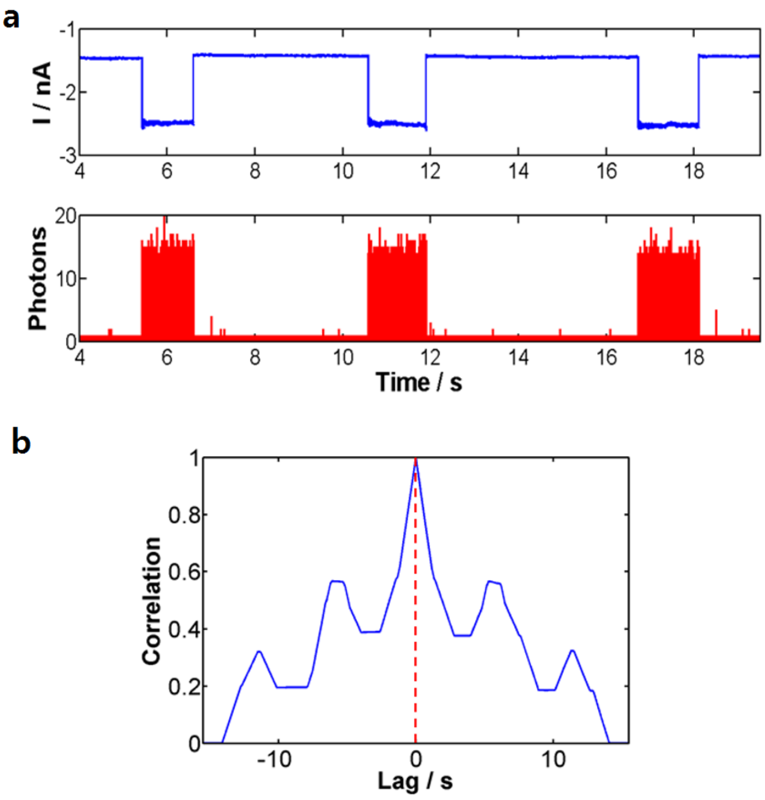

Figure 3-12. (a) The top and bottom trace correspond to ionic current and photon counts within the red channel of the optical set-up (λ~ 640- 800 nm) at -200 mV bias respectively. Electrical data was sampled at 100 kHz and low pass filtered to 10 kHz, whilst optical data was sampled at 100 kHz. Increases in the magnitude of both signals correspond to illumination of the pore with a 1.87 mW, 488 nm wavelength laser. (b) Cross-correlation of the data shown in panel A. The electronic signal trailed the optical signal by an average of 0.18 ± 0.02 ms. Data collected using a ~14 nm diameter (conductance: 9.1 nS) nanopore and a 0.1M KCl, 10mM Tris.HCl, 1mM EDTA (pH7) buffer.

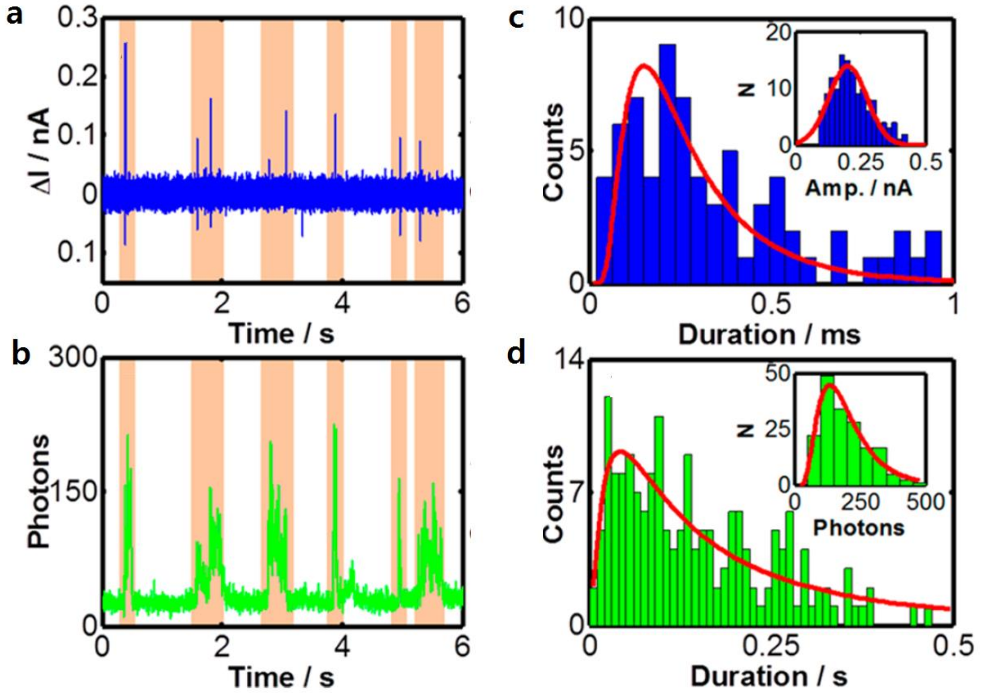

Figure 3-13. (a) and (b) Baseline adjusted ionic current and photon trace for Yoyo®-1 labelled 5 kbp DNA (7.5bp's : 1 dye) translocation detection at 400 mV bias and ~17 μW laser power using two pores (~10 nm and 6 nm diameter, total conductance: 9.1 nS) and a 0.1 M KCl electrolyte. Data within the optical channel has been re-binned at 2 ms resolution. (c) Corresponding electrical data histograms of event duration and amplitude (inset) fit with Ling *et al* and Gaussian probability distribution functions, respectively.[48] (d) Corresponding optical data histograms of event duration and amplitude (inset) fit with log-normal probability distribution functions.

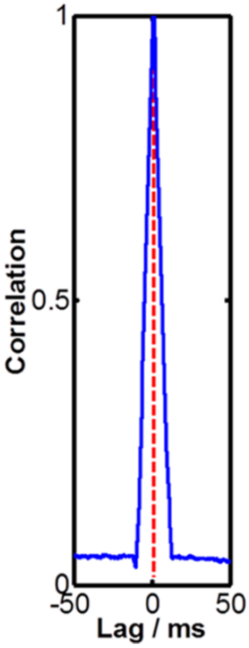

Figure 3-14. Cross-correlation of the optical events within the green channel (λ ~ 500- 580 nm) and the associated peaks in ionic current for the data set shown in Panel A and B in Fig. 3-12.

3.4 Summary

We have presented a process of fabricating polymer membrane on low-noise pyrex substrate using molecular layer deposition with controllable thickness, molecular composition, and orientation. This platform has potential application in the exploration of various biomolecule/polymer interfaces. We have demonstrated the formation of polyurea nanopores with 4–10 nm diameter and sub-10 nm thickness, using a TEM perforation method that induces a highly negative surface charge. We have shown that polyurea nanopores can successfully detect single-molecule translocation events of negatively charged dsDNA at a high ionic strength of 2.5 M KCl, as along with that of positively charged MDM2 protein. Comparing with SiN nanopore and by numerical analysis of EOF, we suggest that EOF suppresses the capture of negatively charged DNA and enhances the capture of positively charged MDM2. In addition, a longer dwell time of MDM2 in the polyurea nanopore, compared to that in the SiN nanopore, was observed as a result of electrostatic interaction. The polyurea nanopore exhibits an advantage of improved detection efficiency of positively charged proteins, in terms of event frequency and slow-down of molecular transport, relative to SiN nanopores. Further work will be to investigate the translocation of various analytes through polyurea nanopore and we expect to demonstrate the influence of the analytes' properties on their translocation.

References

1. Wanunu, M. Nanopores: A Journey towards DNA Sequencing. *Phys. Life Rev.* 2012, *9*, 125–158.

2. Fologea, D.; Gershow, M.; Ledden, B.; McNabb, D. S.; Golovchenko, J. A.; Li, J. Detecting Single Stranded DNA with a Solid State Nanopore. *Nano Lett.* 2005, *5*, 1905–1909.

3. Storm, A. J.; Chen, J. H.; Zandbergen, H. W.; Dekker, C. Translocation of Double-Strand DNA through a Silicon Oxide Nanopore. *Phys. Rev. Stat. nonlinear, soft matter Phys.* 2005, *71*, 51903.

4. Fologea, D.; Ledden, B.; McNabb, D. S.; Li, J. L. Electrical Characterization of Protein Molecules by a Solid-State Nanopore. *Appl. Phys. Lett.* 2007, *91*.

5. Bayley, H.; Cremer, P. S. Stochastic Sensors Inspired by Biology. *Nature* 2001, *413*, 226–230.

6. Ivanov, A. P.; Instuli, E.; McGilvery, C. M.; Baldwin, G.; McComb, D. W.; Albrecht, T.; Edel, J. B. DNA Tunneling Detector Embedded in a Nanopore. *Nano Lett.* 2011, *11*, 279–285.

7. Chansin, G. A. T.; Mulero, R.; Hong, J.; Kim, M. J.; deMello, A. J.; Edel, J. B. Single-Molecule Spectroscopy Using Nanoporous Membranes. *Nano Lett.* 2007, *7*, 2901–2906.

8. Cecchini, M. P.; Wiener, A.; Turek, V. A.; Chon, H.; Lee, S.; Ivanov, A. P.; McComb, D. W.; Choo, J.; Albrecht, T.; Maier, S. A.; *et al.* Rapid Ultrasensitive Single Particle Surface-Enhanced Raman Spectroscopy Using Metallic Nanopores. *Nano Lett.* 2013, *13*, 4602–4609.

9. Miles, B. N.; Ivanov, A. P.; Wilson, K. A.; Dogan, F.; Japrung, D.; Edel, J. B. Single Molecule Sensing with Solid-State Nanopores: Novel Materials Methods and Applications. *Chem. Soc. Rev.* 2013, *42*, 15–28.

10. Deniz, A. a; Mukhopadhyay, S.; Lemke, E. a. Single-Molecule Biophysics: At the Interface of Biology, Physics and Chemistry. *J. R. Soc. Interface* 2008, *5*, 15–45.

11. Aouani, H.; Mahboub, O.; Bonod, N.; Devaux, E.; Popov, E.; Rigneault, H.; Ebbesen, T. W.; Wenger, J. Bright Unidirectional Fluorescence Emission of Molecules in a Nanoaperture with Plasmonic Corrugations. *Nano Lett.* 2011, *11*, 637–644.

12. Liu, S.; Zhao, Y.; Parks, J. W.; Deamer, D. W.; Hawkins, A. R.; Schmidt, H. Correlated Electrical and Optical Analysis of Single Nanoparticles and Biomolecules on a Nanopore-Gated Optofluidic Chip. *Nano Lett.* 2014, *14*, 4816–4820.

13. Soni, G. V; Singer, A.; Yu, Z.; Sun, Y.; McNally, B.; Meller, A. Synchronous Optical and Electrical Detection of Biomolecules Traversing through Solid-State Nanopores. *Rev. Sci. Instrum.* 2010, *81*, 014301.

14. McNally, B.; Singer, A.; Yu, Z.; Sun, Y.; Weng, Z.; Meller, A. Optical Recognition of Converted DNA Nucleotides for Single-Molecule DNA Sequencing Using Nanopore Arrays. *Nano Lett.* 2010, *10*, 2237–2244.

15. Li, J.; Gershow, M.; Stein, D.; Brandin, E.; Golovchenko, J. A. DNA Molecules and Configurations in a Solid-State Nanopore Microscope. *Nat. Mater.* 2003, *2*, 611–615.

16. Rosenstein, J. K.; Wanunu, M.; Merchant, C. a; Drndic, M.; Shepard, K. L. Integrated Nanopore Sensing Platform with Sub-Microsecond Temporal Resolution. *Nat. Methods* 2012, *9*, 487–492.

17. Tabard-Cossa, V.; Trivedi, D.; Wiggin, M.; Jetha, N. N.; Marziali, A. Noise Analysis and Reduction in Solid-State Nanopores. *Nanotechnology* 2007, *18*, 305505.

18. Li, Y.; Chen, C.; Kerman, S.; Neutens, P.; Lagae, L.; Groeseneken, G.; Stakenborg, T.; Van Dorpe, P. Harnessing Plasmon-Induced Ionic Noise in Metallic Nanopores. *Nano Lett.* 2013, *13*, 1724–1729.

19. Huisman, E. M.; Biance, A.-L.; Madouri, A.; Patriarche, G.; Bourhis, E.; Oukhaled, G.; Auvray, L.; Gierak, J. A New Way to Integrate Solid State Nanopores for Translocation Experiments. *Microelectron. Eng.* 2008, *85*, 1311–1313.

20. Lee, M.-H.; Kumar, A.; Park, K.-B.; Cho, S.-Y.; Kim, H.-M.; Lim, M.-C.; Kim, Y.-R.; Kim, K.-B. A Low-Noise Solid-State Nanopore Platform Based on a Highly Insulating Substrate. *Sci. Rep.* 2014, *4*.

21. Larkin, J.; Foquet, M.; Turner, S. W.; Korlach, J.; Wanunu, M. Reversible Positioning of Single Molecules inside Zero-Mode Waveguides. *Nano Lett.* 2014, *14*, 6023–6029.

22. Hong, J.; Lee, Y.; Chansin, G. A. T.; Edel, J. B.; deMello, A. J. Design of a Solid-State Nanopore-Based Platform for Single-Molecule Spectroscopy. *Nanotechnology* 2008, *19*, 165205.

23. Huebner, A.; Srisa-Art, M.; Holt, D.; Abell, C.; Hollfelder, F.; DeMello, A. J.; Edel, J. B. Quantitative Detection of Protein Expression in Single Cells Using Droplet Microfluidics. *Chem. Commun.* 2007, 1218–1220.

24. Tabard-Cossa, V. Instrumentation for Low-Noise High-Bandwidth Nanopore Recording. In *Engineered Nanopores for Bioanalytical Applications*; Edel, J. B.; Albrecht, T., Eds.; Micro and Nano Technologies; William Andrew Publishing: Oxford, 2013; pp. 59–93.

25. Di Fiori, N.; Squires, A.; Bar, D.; Gilboa, T.; Moustakas, T. D.; Meller, A. Optoelectronic Control of Surface Charge and Translocation Dynamics in Solid-State Nanopores. *Nat. Nanotechnol.* 2013, *8*, 946–951.

26. Keyser, U. F.; Krapf, D.; Koeleman, B. N.; Smeets, R. M. M.; Dekker, N. H.; Dekker, C. Nanopore Tomography of a Laser Focus. *Nano Lett.* 2005, *5*, 2253–2256.

27. Hoogerheide, D. P.; Garaj, S.; Golovchenko, J. A. Probing Surface Charge Fluctuations with Solid-State Nanopores. *Phys. Rev. Lett.* 2009, *102*, 256804.

28. Mathews, N. R.; Sebastian, P. J.; Mathew, X.; Agarwal, V. Photoelectrochemical Characterization of Porous Si. 2003, *28*, 629–632.

29. Chen, P.; Mitsui, T.; Farmer, D. B.; Golovchenko, J.; Gordon, R. G.; Branton, D. Atomic Layer Deposition to Fine-Tune the Surface Properties and Diameters of Fabricated Nanopores. *Nano Lett.* 2004, *4*, 1333–1337.

30. Hale, G. M.; Querry, M. R. Optical Constants of Water in the 200-Nm to 200-Mm Wavelength Region. *Appl. Opt.* 1973, *12*, 555–563.

31. Meller, A.; Nivon, L.; Brandin, E.; Golovchenko, J.; Branton, D. Rapid Nanopore Discrimination between Single Polynucleotide Molecules. *Proc. Natl. Acad. Sci. U. S. A.* 2000, *97*, 1079–1084.

32. Fologea, D.; Uplinger, J.; Thomas, B.; McNabb, D. S.; Li, J. Slowing DNA Translocation in a Solid-State Nanopore. *Nano Lett.* 2005, *5*, 1734–1737.

33. Reiner, J. E.; Robertson, J. W. F.; Burden, D. L.; Burden, L. K.; Balijepalli, A.; Kasianowicz, J. J. Temperature Sculpting in Yoctoliter Volumes. *J. Am. Chem. Soc.* 2013, *135*, 3087–3094.

34. Levis, R. A.; Rae, J. L. The Use of Quartz Patch Pipettes for Low Noise Single Channel Recording. *Biophys. J.* 1993, *65*, 1666–1677.

35. Dekker, R. M. M. S. and N. H. D. and C. Low-Frequency Noise in Solid-State Nanopores. *Nanotechnology* 2009, *20*, 95501.

36. Smeets, R. M.; Keyser, U. F.; Dekker, N. H.; Dekker, C. Noise in Solid-State Nanopores. *Proc. Natl. Acad. Sci. U. S. A.* 2008, *105*, 417–421.

37. Hooge, F. N. 1/*f* Noise Is No Surface Effect. *Phys. Lett. A* 1969, *29*, 139–140.

38. Smeets, R. M.; Keyser, U. F.; Wu, M. Y.; Dekker, N. H.; Dekker, C. Nanobubbles in Solid-State Nanopores. *Phys. Rev. Lett.* 2006, *97*, 088101.

39. Chen, P.; Mitsui, T.; Farmer, D. B.; Golovchenko, J.; Gordon, R. G.; Branton, D. Atomic Layer Deposition to Fine-Tune the Surface Properties and Diameters of Fabricated Nanopores. *Nano Lett.* 2004, *4*, 1333–1337.

40. Larkin, J.; Foquet, M.; Turner, S. W.; Korlach, J.; Wanunu, M. Reversible Positioning of Single Molecules inside Zero-Mode Waveguides. *Nano Lett.* 2014, *14*, 6023–6029.

41. Smeets, R. M.; Keyser, U. F.; Krapf, D.; Wu, M. Y.; Dekker, N. H.; Dekker, C. Salt Dependence of Ion Transport and DNA Translocation through Solid-State Nanopores. *Nano Lett.* 2006, *6*, 89–95.

42. Kraus, J. D. *Electromagnetics*; Carver, K. R., Ed.; McGraw-Hill electrical and electronic engineering series; McGraw-Hill: New York, 1973.

43. Zhu, P.; Craighead, H. G. Zero-Mode Waveguides for Single-Molecule Analysis. *Annu. Rev. Biophys.* 2012, *41*, 269–293.

44. Aksimentiev, A.; Heng, J. B.; Timp, G.; Schulten, K. Microscopic Kinetics of DNA Translocation through Synthetic Nanopores. *Biophys. J.* 2004, *87*, 2086–2097.

45. Heng, J. B.; Ho, C.; Kim, T.; Timp, R.; Aksimentiev, A.; Grinkova, Y. V; Sligar, S.; Schulten, K.; Timp, G. Sizing DNA Using a Nanometer-Diameter Pore. *Biophys. J.* 2004, *87*, 2905–2911.

46. Liu, H.; Qian, S.; Bau, H. H. The Effect of Translocating Cylindrical Particles on the Ionic Current through a Nanopore. *Biophys. J.* 2014, *92*, 1164–1177.

47. Menestrina, J.; Yang, C.; Schiel, M.; Vlassiouk, I.; Siwy, Z. S. Charged Particles Modulate Local Ionic Concentrations and Cause Formation of Positive Peaks in Resistive-Pulse-Based Detection. *J. Phys. Chem. C* 2014, *118*, 2391–2398.

48. Ling, D. Y.; Ling, X. S. On the Distribution of DNA Translocation Times in Solid-State Nanopores: An Analysis Using Schrödinger's First-Passage-Time Theory. *J. Phys. Condens. Matter* 2013, *25*, 375102.

49. Venta, K.; Shemer, G.; Puster, M.; Rodríguez-Manzo, J. A.; Balan, A.; Rosenstein, J. K.; Shepard, K.; Drndić, M. Differentiation of Short, Single-Stranded DNA Homopolymers in Solid-State Nanopores. *ACS Nano* 2013, *7*, 4629–4636.

50. Ivankin, A.; Henley, R. Y.; Larkin, J.; Carson, S.; Toscano, M. L.; Wanunu, M. Label-Free Optical Detection of Biomolecular Translocation through Nanopore Arrays. *ACS Nano* 2014, *8*, 10774–10781.

51. Jonsson, M. P.; Dekker, C. Plasmonic Nanopore for Electrical Profiling of Optical Intensity Landscapes. 2013, 8–12.

52. Jothimuthu, P.; Carroll, A.; Bhagat, A. A. S.; Lin, G.; Mark, J. E.; Papautsky, I. Photodefinable PDMS Thin Films for Microfabrication Applications. *J. Micromechanics Microengineering* 2009, *19*, 45024.

53. Eilers, P. H. C.; Boelens, H. F. M. Baseline Correction with Asymmetric Least Squares Smoothing. *Leiden Univ. Med. Cent. Rep.* 2005.

Chapter 4.

Translocation of DNA and protein through sequentially polymerized polyurea nanopore

This chapter is based the paper published in

Nanoscale, (2018)

4.1 Introduction

Nanopore sensing is an emerging technology for characterizing various biomolecules and their complexes at single-molecule resolution.[1-3] In this, molecules are translocated through a nanometer-sized pore by an applied electric field and the translocations are detected by transient changes of ionic current. The change in magnitude and dwell time of current provides information on the structural features of the analytes, such as the size and length of biomolecules, specific sequence of nucleic acids in DNA, or the conformational changes in proteins.[2] There has been much progress in protein nanopores, as in α-hemolysin and MspA embedded in the lipid bilayer, with advantages of having a reproducible and uniform sized pore (< 1.5 nm) and feasibility of modifying the pore functionality by genetic engineering.[4-5] In contrast, progress in solid-state nanopores has been relatively slow, despite the merits of mechanical and chemical durability of membrane and pore-size adjustability to accommodate various-sized analytes.[1]

In the solid-state nanopore analysis, one of a major difficulty is to understand the effect of surface characteristics, such as charge density and chemical affinity of the pore periphery, on the translocation of biomolecule. For instance, many studies have shown that translocation of biomolecule is affected by the surface chemistry or surface charge of the membrane, by either employing various membrane materials[6-8] or by coating with organic species[9-

[11]. Surface charge[6-7, 11], hydrophobicity[8], and specific biological binding affinity[9-10] of the membrane are known to effectively slow down the transport of molecules. Moreover, surface charge of the membrane is well known to cause electro-osmotic flow, which affects molecule capture rate and translocation kinetics.[12-13]

In this aspect, organic material is highly desirable as the membrane, due to its wide range of surface charge density, hydrophobicity, and chemical functionality, which can provide suitable biomolecule-sensing platform for a specific application.[14-20] Previous studies on solid-state nanopores, using organic material, had adopted one of the following two approaches: (1) using polymer film as membrane[21-23], and (2) coating organic molecules on inorganic nanopore surface as a self-assembled monolayer (SAM)[9, 11, 17, 24-29]. Nanopore on polymer membrane have been fabricated by laser heating[22] or track-etch method[21, 23]; however, the thickness of polymer films reported so far has been > 10 μm. SAM coating on nanopore surface allows the fabrication of a sub-10-nm-thick membrane with advantages of utilizing various organic molecules for modifying its surface functional groups. However, an additional coating step complicates the fabrication process and the dimension of the nanopore is often difficult to control.

In this chapter, we present a sub-10-nm-thick polyurea membrane using molecular layer deposition (MLD). MLD is considered an outstanding technique to fabricate ultrathin organic films with precisely controlled film thickness, composition, and molecular orientation.[30-35] The polyurea membrane was chosen due to its high mechanical stability[30], chemical resistance[30], thermal stability[36], and its potential application in lithography[37]. Moreover, a highly negative surface charge density at neutral pH is anticipated, since the isoelectric point of polyurea (pH = 2.6)[38] is lower than that of the SiN nanopore (pH = 5)[39]. First, we fabricated uniformly aligned polyurea films through coupling reactions between *p*-phenylenediisocyanate (PDI) and *p*-phenylenediamine (PDA), by MLD based on self-limiting surface reactions. After transferring the polyurea film on our prepared low-noise pyrex substrate[40], nanopores were perforated using focused electron beam from TEM. Next, we analyzed the ionic conductance and noise characteristics of such nanopores. Finally, we investigated the translocation of dsDNA and MDM2 proteins through the highly negatively charged polyurea nanopore. Our experimental scheme is summarized in Fig. 4-1.

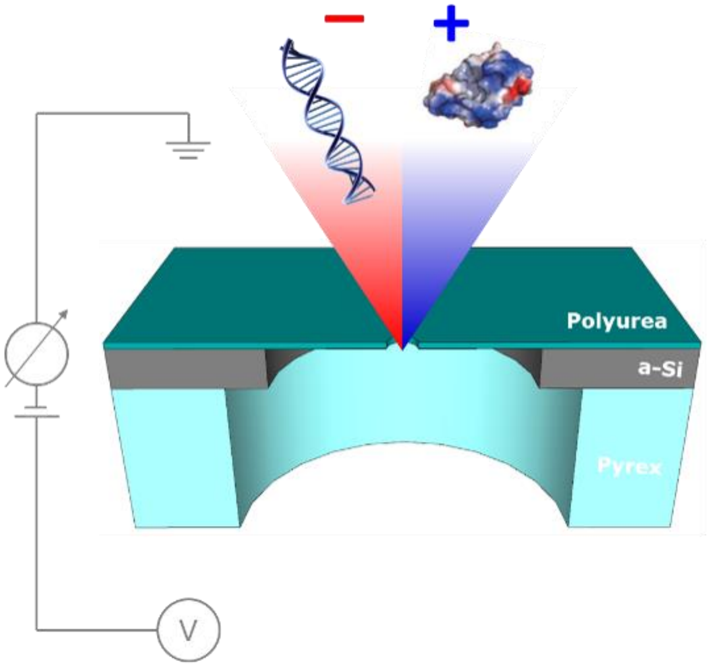

Figure 4-1. A schematic representation of DNA and MDM2 translocation through polyurea nanopore on a pyrex substrate

4.2 Experimental details

Fabrication of polyurea MLD film

Organic polyurea MLD films were fabricated in our homemade hot wall viscous flow vacuum MLD chamber equipped with *in situ* Fourier-transform infrared spectroscopy (FTIR) apparatus (Fig. 4-2) by Ui-Jin Choi and Hyein Kim from Jin Seok Lee’s laboratory in Sookmyung women's university, in the same way as in previous report.[31-33] The organic precursors, **p**-penylenediisocyanete (PDI; $C_6H_4(NCO)_2$), and *p*-penylenediamine (PDA; $C_6H_4(NH_2)_2$), were heated to 90 ℃, and 105 ℃, respectively, to achieve reasonable vapor pressure, and MLD chamber was heated to 110 ℃. After 60 s PDI dosing with a 30 sccm flow of Ar carrier gas, the MLD chamber was maintained for 30 s to provide a sufficient opportunity for surface reaction. And, the MLD chamber was purged with Ar for 120 s at a flow rate of 400 sccm, and evacuated for 30 s to ensure that no precursors remained in the chamber. These sequences of dose, exposure, purge, and evacuation were repeated with PDA.

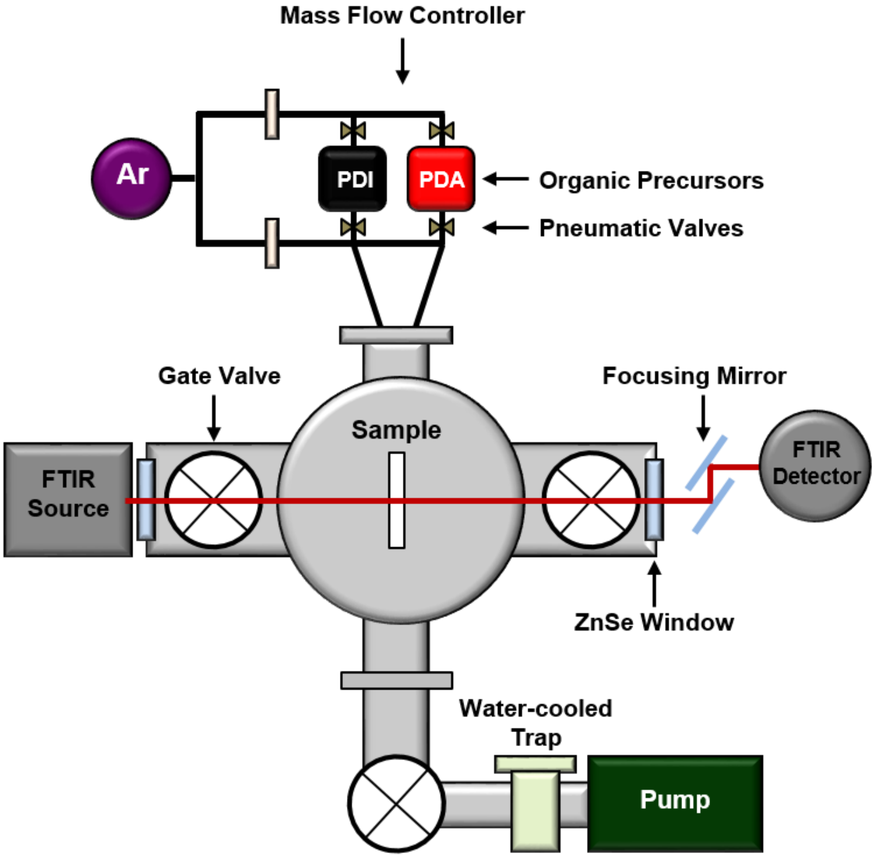

Figure 4-2. Schematics diagram of homemade MLD set up, equipped with in situ FTIR spectroscopy and hot wall viscous flow vacuum chamber.

Ex-situ characterization

Film thickness on flat substrate was measured by ex-situ ellipsometry (Gaertner Scientific C., L2W15S830) using He-Ne laser light at a wavelength of 632.8 nm. Thickness was measured in at least four different spots on each sample to confirm uniformity of the polyurea MLD film. Two-dimensional AFM image and height profile were obtained using atomic force microscopy (AFM; Park Systems, NX-10), with 30-nm-thick Al-coated cantilever in a noncontact mode, at a scan size of 3 μm × 3 μm. Zeta potential of film surface was measured by electrophoretic light scattering spectrophotometer (Delsa Nano C, ELS Z-1000). Surface of the sample was configured with the top a box-like cell. Zeta potential was calculated from the apparent electrophoretic mobility by monitoring particles at several positions inside the cell and analyzing the electro-osmotic mobility on the solid surface using the electro-osmotic profile.

Nanopore measurements

Prior to ionic current measurements, the nanopore chips were immersed in diluted ethanol (30 %) for 2 h to enhance the wettability of the pores. Then, a 5 mm nanopore chip was mounted on a customized PTFE microfluidic flow cell with a PDMS gasket of 3 mm diameter, and both chambers were filled with a KCl electrolyte and TE buffer solution (pH 8) or 1× PBS (pH 7.4) buffer solution. Ag/AgCl electrodes were inserted into both chambers of the flow cell and bias voltage was applied on the trans- chamber. The electrodes were connected to an Axopatch 200B amplifier with a sampling rate of 250 kHz and low pass four-pole Bessel filter of 100 kHz. The 1 kbp NoLimits DNA fragments (Thermo Scientific) was used and 2 nM of dsDNA was inserted into the cis- chamber. Recombinant MDM2 N-terminal domain (residues 3-109) construct was overexpressed in Escherchia coli BL21 (DE3) by induction with 0.4 mM isopropyl-β-D-thioglactoside (IPTG) at the OD600 of 0.9 by Dong-kyu Kwak from Seung-Wook Chi's laboratory in Korea research institute of bioscience and biotechnology. After IPTG induction, cells were grown at 20 ℃ for 16 hours in LB media. The protein was precipitated with ammonium sulfate and further purified using ion exchange chromatography (HiTrap™ SP and Q, GE Healthcare) and gel-filtration chromatography (HiLoad® 16/600 Superdex® 75pg, GE healthcare), as previously reported.[41] Hundred nanomolar proteins were inserted into the cis- chamber. The translocation events were collected, and analyzed using Clampfit, pCLAMP 10.4 software.

4.3 Results and discussion

4.3.1 Fabrication of polyurea nanopores

At first, polyurea MLD film was fabricated in homemade MLD chamber equipped with an *in situ* Fourier-transform infrared (FTIR) spectrometer. The surface reactions for the polyurea MLD film are schematically illustrated in Fig. 4-3a. One MLD cycle consisted of a sequential molecular reaction between PDI and PDA precursor, and polyurea MLD films of a desired thickness was obtained by varying the number of cycles. To identify self-limiting surface reaction, we conducted *in situ* FTIR measurements during alternative gas phase exposures of PDI and PDA on a SiO_2 nanoparticle substrate (Fig. 4-3b).[31-33] When the PDI precursor reacted with the SiO_2 substrate, a N=C=O stretching vibration peak arose at 2270 cm^{-1} and the N-H stretching vibration appeared at 3400–3100 cm^{-1}. In addition, the C=O stretching (amide I) and C-N stretching vibration (amide II) peaks appeared at 1651 cm^{-1} and 1510 cm^{-1}, respectively, indicating the formation of urethane linkage. After PDA exposure, the amine group reacted with the surface-terminated N=C=O group from which the urea linkage was formed. We also monitored the thickness of $(PDI/PDA)_n$ polyurea MLD films as a function of the number of cycles, using ex-situ ellipsometry, as shown in Fig. 4-3c. The thickness of polyurea MLD films followed a linear growth curve with a constant growth rate of 3.9 Å /cycle.

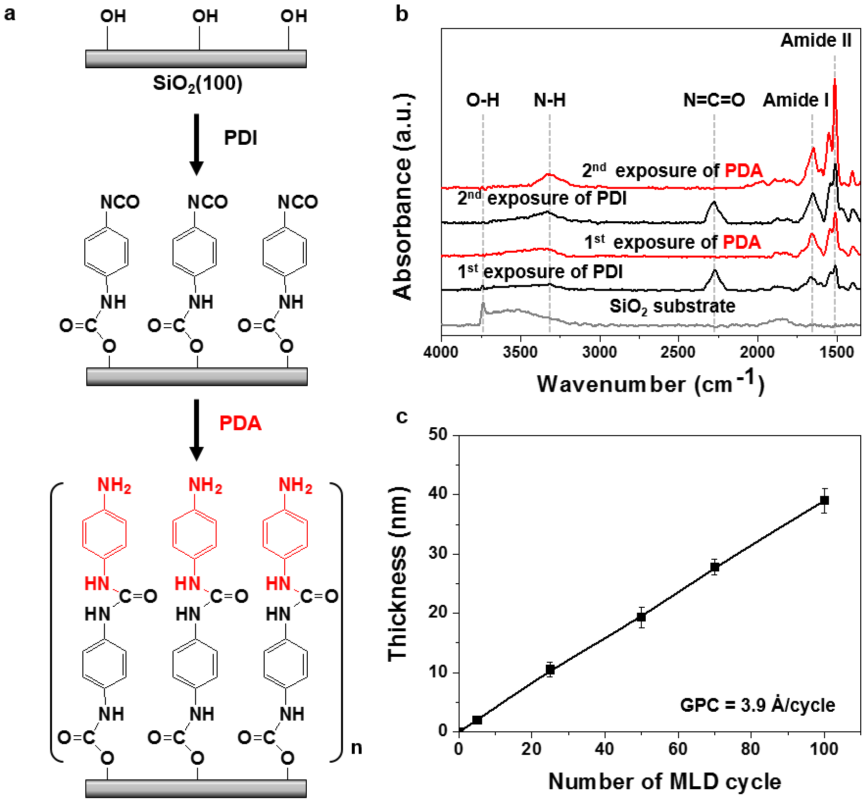

Figure 4-3. (a) Illustration for surface reaction of polyurea film fabricated by molecular layer deposition (MLD). The *p*-phenylenediisocyanate (PDI) and *p*-phenylenediamine (PDA) are alternately bonded on SiO_2 (100) substrate. (b) In-situ FTIR spectra of the SiO_2 substrate after the first and second exposure of PDI and PDA. (c) Thickness profiles of $(PDI/PDA)_n$ polyurea MLD films as a function of the number of MLD cycles using ellipsometry.

We characterized the surface charge density of polyurea film using zeta potential analyzer and compared it with that of SiN deposited on Si substrate, using low-pressure chemical vapor deposition. The measured zeta potential values of polyurea and SiN films were –20.5 ± 0.7 mV and –4.5 ± 0.2 mV, respectively. The relatively high negative value in case of polyurea was also reported by Elrehim *et al* (–36.7 ± 5.6 mV at pH 7, 1 mM KCl)[38], and a similar value of zeta potential was reported in SiN membrane (–7.9 ± 3.6 mV at pH 7.8, 0.4 M KCl)[42]. The highly negative surface charge density of polyurea film is due to the interaction of urea groups with hydroxyl anions (OH^-) to form the negative surface.[38]

The polyurea films $(PDI/PDA)_{25}$, grown on Si/SiO_2 substrate, were then covered with poly-methyl-methacrylate (PMMA) and immersed in diluted hydrofluoric acid to separate the PMMA-polyurea samples by etching the SiO_2 substrate. The floated PMMA-polyurea layers were rinsed in deionized water and transferred to the prepared pyrex substrate with 2-μm opening.[40] The samples were then immersed in acetone and 2-propanol for 10 s each, to remove PMMA (Fig. 4-4a). The polyurea membrane that covered the 2-μm hole is shown in transmission electron microscope (TEM) image (Fig. 4-4b). The thickness of transferred polyurea film (10 nm) was confirmed using atomic force microscope (AFM), as shown in Fig. 4-5. Finally, a nanometer-sized pore was drilled in polyurea membrane by focused electron beam using

200 kV TEM (1.5 nA e-beam current and 0.12 nA/nm^2) with pore size ranging from 4 to 10 nm, as seen in Fig. 4-4c.

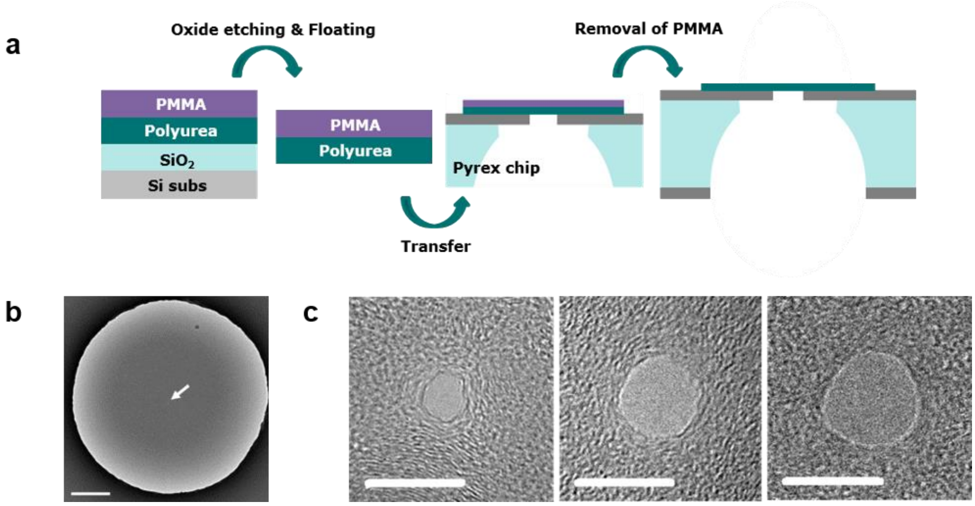

Figure 4-4 (a) Fabrication process of polyurea nanopore with pyrex substrate. A 10-nm-thick polyurea is deposited by MLD on SiO_2 substrate. The free-standing polyurea membrane is fabricated by wet-transfer method using PMMA supporting layer and HF-wet etching. (b) TEM image of 2 μm free-standing polyurea membrane with a-Si supporting layer (scale bar: 0.5 μm). (c) TEM images of polyurea nanopores with 5, 7, and 10-nm diameter (scale bar: 10 nm).

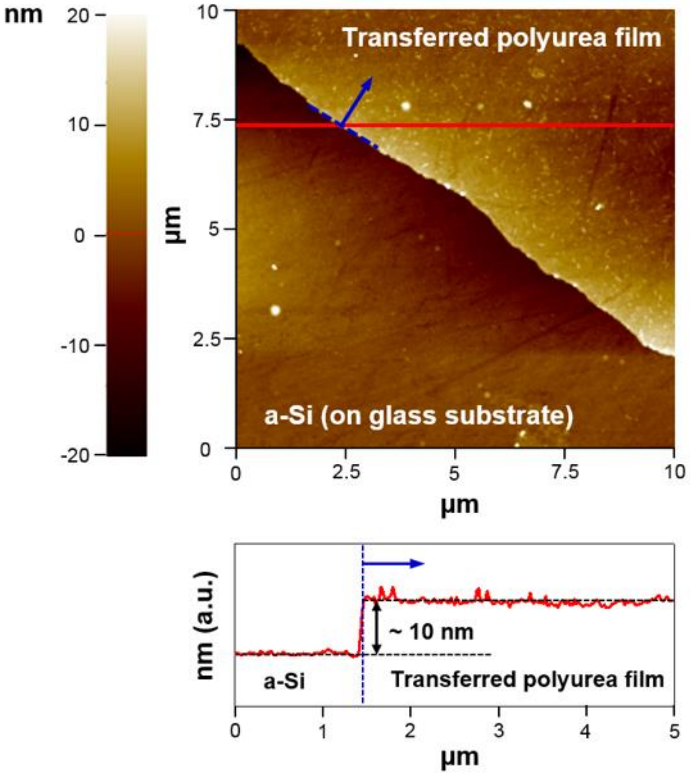

Figure 4-5 (a) Two-dimensional AFM image and the height profiles (along with red line in AFM image) of the (PDI/PDA)$_{25}$ polyurea MLD film transferred to a-Si layer on pyrex substrate. The blue arrow indicates the polyurea film and the right is the a-Si layer. The scan area is 10 μm × 10 μm.

4.3.2 Characterization of polyurea nanopores

After the nanopore chip was immersed in diluted ethanol (40 %) to enhance the wettability of the pores, ionic conductance was measured in 1 M KCl solution with TE buffer (10 mM Tris and 1 mM EDTA, pH 8.0) using an Axopatch amplifier. Fig. 4-6a shows the current-voltage characteristics of polyurea nanopores with 5, 7, and 10 nm diameter. The ionic currents exhibited ohmic characteristic in the voltage ranges from −300 to 300 mV and each conductance value was fitted to be 33, 54, and 112 nS, respectively. At high salt concentrations (>0.1 M), the conductance of a nanopore can be estimated by the pore dimension with the contributions from bulk ion concentration, access resistance, and electro-osmosis:[3]

$$G = \left((\mu_{K+} + \mu_{Cl-})n_{KCl}e\right)\left(\frac{4h_{eff}}{\pi {d_p}^2} + \frac{1}{d_p}\right)^{-1} + \mu_{K+}\sigma\frac{\pi d_p}{h_{eff}},$$

where μ_{K+} and μ_{Cl-} are the electrophoretic mobility of K^+ ($7.62 \times 10^{-8}\ \mathrm{m^2\,V^{-1}s^{-1}}$) and Cl^- ions ($7.91 \times 10^{-8}\ \mathrm{m^2\,V^{-1}s^{-1}}$), n_{KCl} is the number density of K^+ or Cl^- ions, e is the elementary charge, d_p is the diameter of pore, h_{eff} is the effective thickness of pore, and σ is the surface charge density of pore.[43] The electro-osmosis term (last term) in the equation present the surface charge contribution to the conductance that explain the transport of counter-ions shielding the charged pore surfaces.[43-44] By inserting measured membrane thickness and pore diameter, we estimated the surface charge density of polyurea nanopores at 1 M KCl electrolyte (Fig. 4-7). We obtained the surface charge density for polyurea nanopores as −51 ± 8 mC/m^2 at 1 M KCl, which is much higher than that for SiN nanopores (−14 ± 5 mC/m^2 at 1 M KCl). The obtained value of SiN nanopores is well matched with the reported value (−18 mC/m^2 at 1 M KCl)[43].

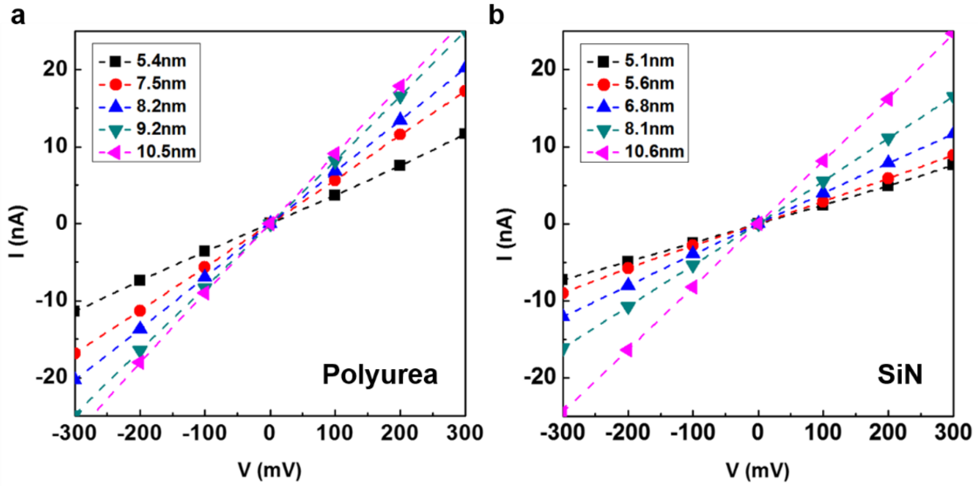

Figure 4-6 Ionic current *vs* applied voltage characteristics for (a) polyurea nanopore (h_{eff}=8nm) and (b) SiN nanopore (h_{eff}=9nm) at 1 M KCl electrolyte with TE buffer (pH=8).

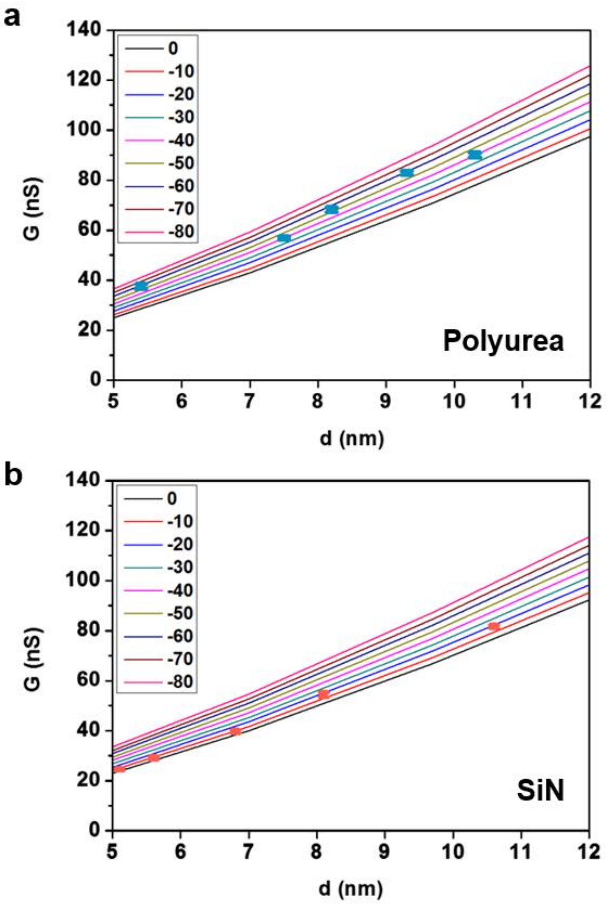

Figure 4-7 The experimental conductance value in Fig. 4-6 were fitted with the conductance equation. The conductance of five polyurea nanopores (a) and SiN nanopores (b) were used to characterize the surface charge density at 1 M KCl. The solid line indicates the surface charge density value with 10 mC/m2s intervals. The surface charge of polyurea nanopore is in -51 ± 8 mC/m2 and SiN nanopore is in -14 ± 5 mC/m2.

Fig. 4-8 shows the noise characteristic analysis of the polyurea nanopore by power spectral density (PSD) plots for Φ 7 nm polyurea pore at 0 and 100 mV. The PSD data were obtained from 20-s-recorded trace at a sampling rate of 250 kHz and digital low-pass Bessel filter of 100 kHz. As a result of low capacitance (10 pF in 1M KCl buffer) of pyrex substrate[40, 45], polyurea nanopore has a low dielectric noise of $6 \times 10^{-8}\, f$ $(\mathrm{pA}^2/\mathrm{Hz})$ and exhibits low RMS noise value, 30 pA at 0 mV. However, it exhibited relatively high 1/f noise levels $(80/f^{0.9}$ $\mathrm{pA}^2/\mathrm{Hz})$ with RMS noise value of 60 pA at 100 mV. The origin of this high flicker noise in polyurea membrane is not clear at this moment. Previously, mechanical stability of membrane[46], carbon contaminants from the surface[47], and imperfect wetting of nanopore surface[48-49] had been reported as the possible sources of high flicker noise (1/f noise). For instance, mechanical instability of the membrane has been reported as a source of high flicker noise in atomically thin 2-D membranes such as graphene, BN, and MoS_2, and this 1/f noise is reduced by increasing membrane thickness[6, 50] or reducing the window size of the supporting layer[51-52]. However, we do not see improvement of 1/f noise either by increasing the membrane thickness to 25 nm or by reducing the window size of the supporting layer to 150 nm^2, suggesting that mechanical stability is not the primary source (Fig. 4-9). For SiN nanopores, carbon contaminants and imperfect wetting of pore are reported to be sources of high 1/f noise and can be improved by cleaning with piranha solution (H_2SO_4:H_2O_2) from

$100/f$ pA^2/Hz (bare state) to $1/f$ pA^2/Hz.[49] However, polyurea nanopores cannot be treated with piranha solution since it damages the membrane. Nevertheless, polyurea nanopores have a sufficient noise level to detect biomolecules at 100 kHz signal bandwidths, as shown below.

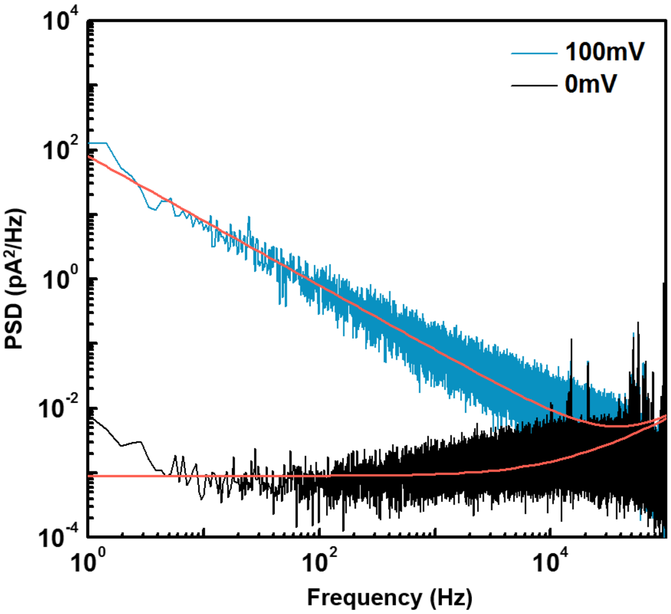

Figure 4-8 Power spectral densities (PSD) of 7-nm pores at 0 and 100 mV applied voltages in buffered 1 M KCl solution (pH 8.0), filtered at 100 kHz. Each red line results from fitting of the data to: $S = Af^{-\beta} + B + Cf + Df^2$.

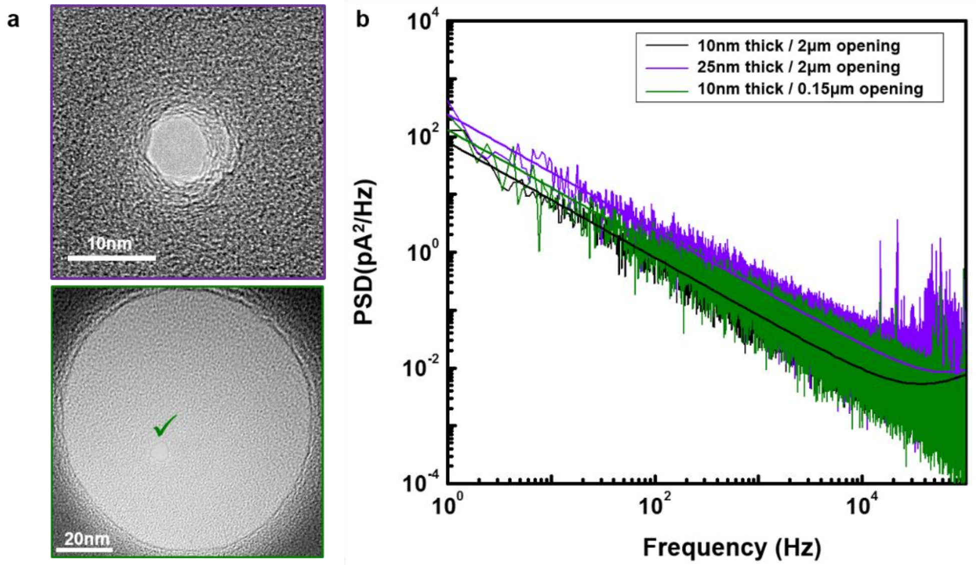

Figure 4-8 (a) TEM images of 7 nm polyurea nanopores with 25 nm thick 2μm opening membrane (Top) and 10 nm thick 0.15 μm opening membrane (Bottom) (b) Power spectral densities (PSD) for 3 kinds of 7 nm pores under 100 mV voltages in 1 M KCl electrolyte solution with TE buffer (pH 8.0), filtered at 100kHz. Each line results from fitting of the data to $S = Af^{-\beta} + B + Cf + Df^2$.

4.3.3 DNA detection

To investigate the transport behavior of DNA molecules through polyurea nanopores, 1 kbp dsDNA was translocated through polyurea nanopores in KCl electrolyte with a TE buffer (pH 8.0), using a low pass filter of 100 kHz. At first, the transport of DNA for ϕ 5–10 nm polyurea nanopores was rarely observed in 1 M KCl solution, whereas that for SiN nanopores was well observed under the same condition (Fig. 4-9). Several reports have shown that the translocation frequency of DNA into the nanopore can be enhanced by altering charge distribution of the pore[53-55], or by changing the ionic strength of the solution[56-57], mostly in protein nanopore. For instance, Franceschini *et al* presented that dsDNA does not translocate through highly negatively charged ClyA protein nanopores (net charge of pore lumen; −120) at 1 M NaCl, but does so at higher ionic strengths (2.5 M NaCl).[57] Inspired by Franceschini *et al,* we tested the translocation of DNA through polyurea nanopore at 2.5 M KCl. Fig. 4-10a shows the continuous 10 s current traces at 200 mV (black), 250 mV (red) and 300 mV (blue) of applied voltages. Indeed, these results demonstrate that DNA translocates through the polyurea nanopore at high molar concentrations; the scatter plots of blockade current (ΔI) *vs* dwell time (t_D) at applied voltages in the range 200–300 mV are shown in Fig. 4-10c. The number of total events was 185 (200 mV), 244 (250 mV), and 280 (300 mV) and corresponding histograms of ΔI fitted with Gaussian distribution the in Fig. 4-10d. As expected, the mean values of ΔI present a linear dependency on the applied voltages (inset in Fig. 4-10d), with the blockade conductance (ΔG) being 5.53±0.34 nS. The ΔG is estimated by $\Delta G = G(d_p) - G(d_{eff})$, where G is the calculated conductance, and d_{eff} is the effective diameter of the pore with the DNA inside, calculated by $d_{eff} = \sqrt{(d_p{}^2 - d_{DNA}{}^2)}$, taking d_{DNA} = 2.2 nm.[58] The estimated ΔG (5.87 nS) is well matched with measured ΔG (5.53 nS). In addition, the histograms of log t_D at each driving voltage of 200, 250, and 300 mV are plotted in Fig. 3e, to determine the mean values of t_D. The fitted mean t_D values were 97±1, 34±1, and 15±1 μs at 200, 250, and 300 mV, respectively.

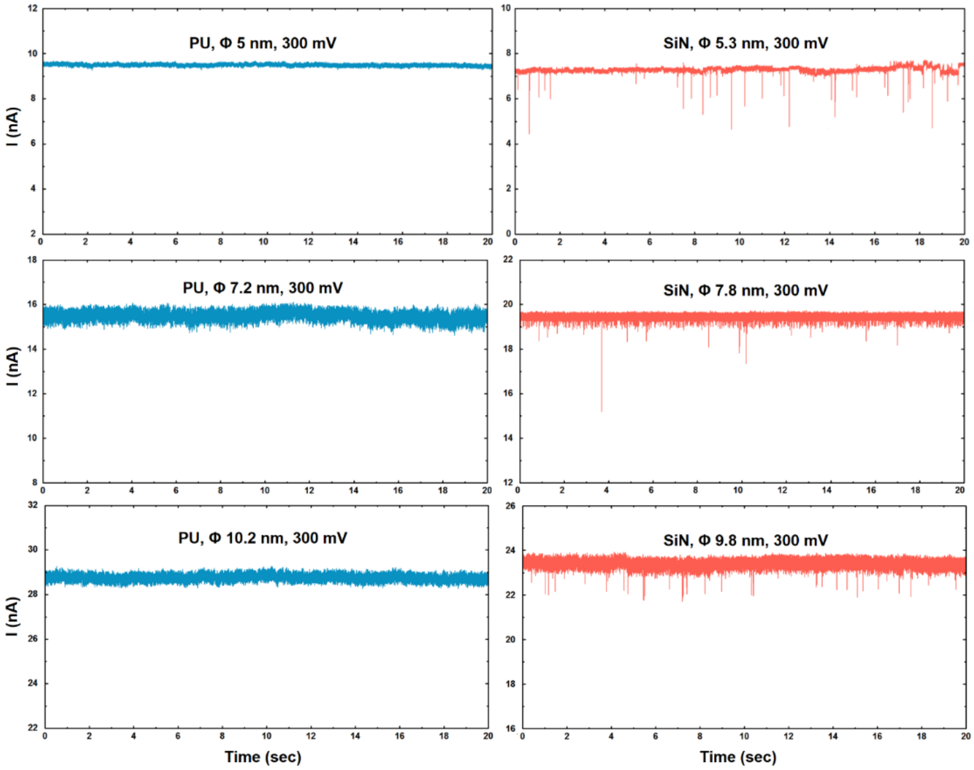

Figure 4-9 Ionic current traces with 2nM 1kbp dsDNA in cis-chamber for polyurea nanopore and SiN nanopore at 300 mV applied voltage, filtered at 100 kHz in 1 M KCl with TE buffer (pH 8.0).

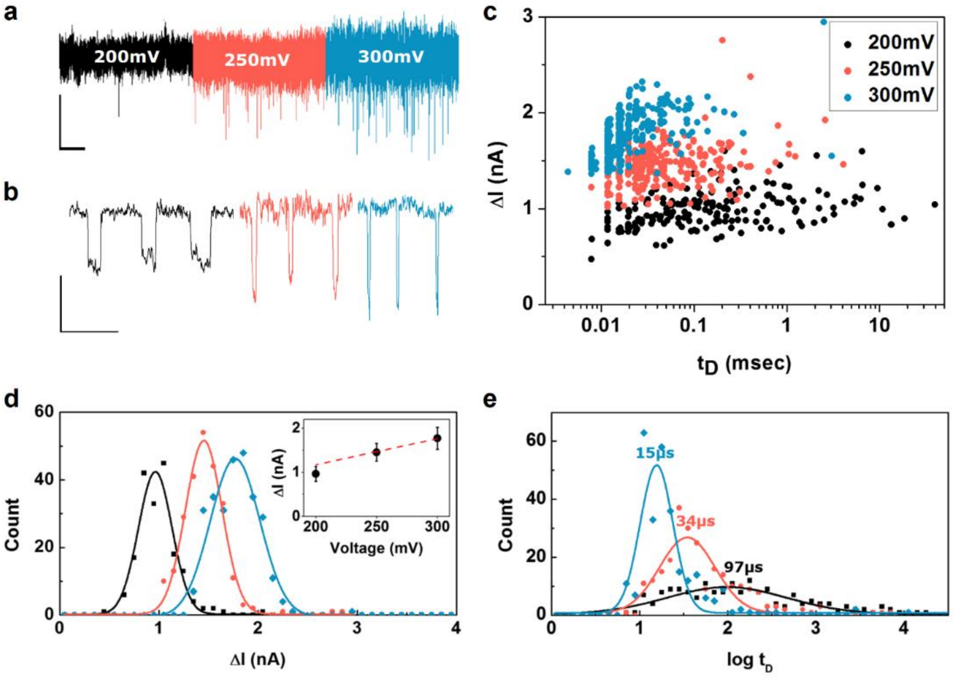

Figure 4-10 (a) Continuous 10-s ionic current traces for 1-kbp DNA translocation through polyurea nanopore (Φ 7.2 nm, 8 nm thick) in buffered 2.5 M KCl solution (pH 8.0) at 200 mV (black), 250 mV (red), 300 mV (blue) (scale bar: 1 nA, 2 s). (b) Representative events extracted from the current traces in (a) (scale bar: 1 nA, 0.5 ms). (c) Scatter plots of ΔI *vs* t_D for 1-kbp DNA translocation through Φ 7.2 nm polyurea nanopore in the range V = 200–300 mV. (d) Histograms of ΔI corresponding to panel c in the range V = 200–300 mV. Solid lines indicate the Gaussian distribution fits and the inset shows the mean values of ΔI with respect to applied voltage. The dashed line represents the linear fit of data. (e) Histograms of log t_D in the range V = 200–300 mV. Solid lines indicate the Gaussian distribution fits.

In order to explain the obtained results, namely, the noticeable increase in event frequency at 2.5 M KCl relative to that at 1 M KCl solution, we estimated the electro-kinetic forces on DNA capturing at each condition. The negatively charged polyurea surface inside the pore may induce two effects on DNA trapping: (1) electro-osmotic force (EOF) resulting from the cation flow inside the pore, acting in a direction opposite to that of the electrophoretic driving force on DNA and (2) electrostatic repulsion between the negatively charged DNA and negatively charged polyurea surface. The effect of electrostatic repulsion is likely to be minor, since the pore diameter is considerably larger than the Debye screening length ($\lambda_D;$ 0.3 nm at 1 M; 0.2 nm at 2.5 M;). When $\lambda_D \ll d_p/2$, the velocity of EOF (v_{EO}) can be calculated by the Helmholtz-Smoluchowski equation:

$$v_{EO} = -\mu_{EO} E, \qquad \mu_{EO} = {}^{\epsilon\zeta}/_{\eta},$$

where ϵ is permittivity of the electrolyte solution, ζ is zeta potential of the pore wall, η is viscosity of the electrolyte solution, and E is electric field. We assumed that the surface charge density of the nanopore is constant in the salt concentration range of 1–2.5 M referring to the previous studies in SiN nanopore and follows the Grahame equation, $\sigma = \epsilon\zeta/\lambda_D$ for $\zeta \ll 50$ mV (Fig. 4-11).[43] With the reported and calculated parameters ($\epsilon = 80\epsilon_0$; ζ values as calculated from measured $\sigma = -51\,mC/m^2$ and $\lambda_D = 0.303/\sqrt{c}$; where c is the salt concentration; $\eta = 1\,mPa\ s$;), the calculated μ_{EO} at 1 M

KCl ($1.53 \times 10^{-8}\ m^2V^{-1}s^{-1}$), dropped to $0.97 \times 10^{-8}\ m^2V^{-1}s^{-1}$ at 2.5 M KCl, due to the decrease in λ_D. The electrophoretic velocity of DNA can be estimated by $v_{EP} = \mu_{DNA}E$, where μ_{DNA} is the mobility of DNA. The free solution mobility of 1kbp DNA from gel electrophoresis measurement is $3.75 \times 10^{-8}\ m^2V^{-1}s^{-1}$, which is larger than the μ_{EO} within the same order of magnitudes.[59] However, when DNA is captured into the relatively small sized pore, DNA could become less mobile, since the electrophoretic force only drags a small part of a long DNA chain. These findings suggest that the EOF on polyurea nanopores inhibit the electrophoretic capture of DNA at 1 M KCl, in addition to the entropic barrier.[60-62]

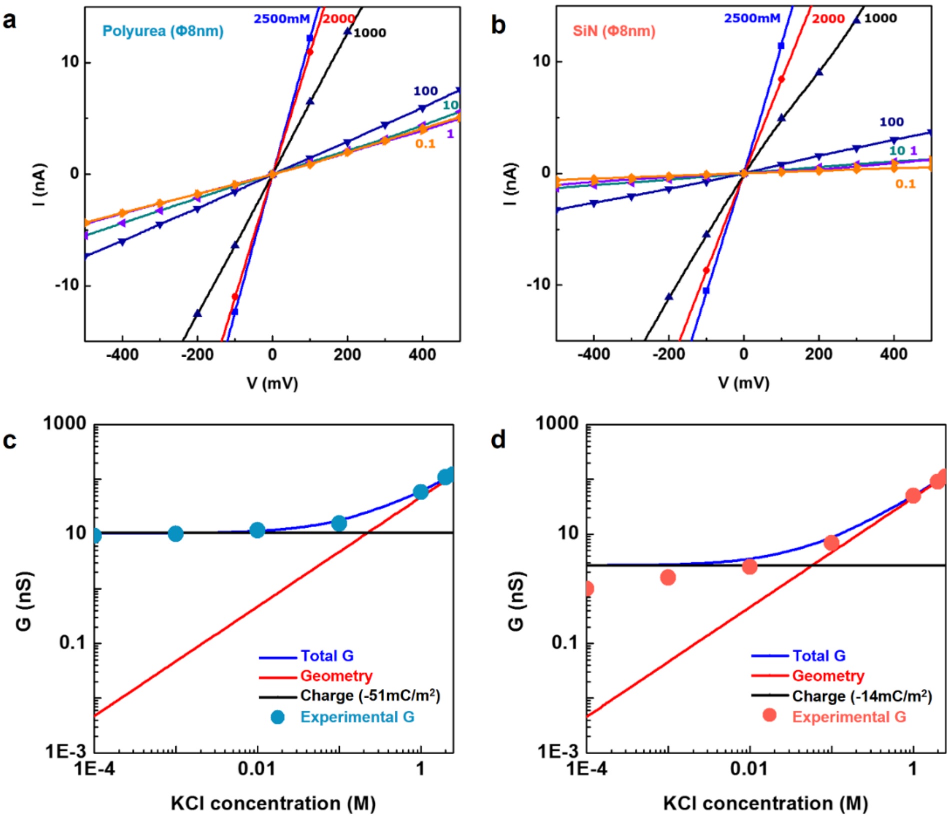

Figure 4-11 (a) I-V plots on a. polyurea nanopore (a, d=8nm, h=9nm) and b. SiN nanopore (d=8nm, h=10nm) at 0.1, 1, 10, 100, 1000, 2000 and 2500 mM KCl electrolyte with TE buffer (pH=8). The experimental conductance value were fitted with the conductance equation. (c, d) The point is experimental conductance and blue line is calculated total conductance, which is a sum of geometry term and surface charge density term. The surface charge of polyurea nanopore (c) is in -50 ± 5 mC/m^2 and SiN nanopore (d) is ranging from -5.2 to -13 mC/m^2 at 0.1mM ~ 2.5 M KCl electrolyte.

4.3.4 Protein detection

In order to confirm the EOF effect, we tested the translocation of positively charged MDM2 protein (net charge at pH 7.4 = +2.9e, PI = 9.02), which is opposite to the charge on DNA. In this case, since the EOF and electrophoretic force acted in the same direction, we expected a higher translocation frequency. Due to the relatively low surface charge density of protein than that of DNA, EOF could be the major driving force for capture than the electrophoretic force in both solid-state nanopores[39, 42, 63] and biological nanopores.[64-66] For instance, Frinkes *et al* observed that EOF can enhance, suppress, and even reverse electrophoretic transport, depending on the zeta potential difference between pore surface and protein (avidin) by varying the pH at ±150 mV applied bias.[39] In addition, translocation frequency of streptavidin was reported to be higher in the EOF direction (36 s^{-1}) than in the electrophoretic direction (0.7 s^{-1}), despite the higher zeta potential of streptavidin (+20 mV) compared to that of pore surface (+8 mV).[39] Furthermore, Waduge *et al* demonstrated that capture of 10 different kinds of proteins are dominated by EOF, irrespective of the protein charge (range of −26 to +7), through negatively charged SiN and hafnium oxide nanopores.[42]

To characterize the MDM2 translocation behavior, a comparison of current-time trace for the translocation of 100 nM MDM2 at −100, −125, and −150 mV, using both polyurea nanopore (d_p = 10 nm and h_{eff} = 8 nm) and SiN nanopore (d_p = 9.5 nm and h_{eff} = 9 nm) in 1 M KCl with 1x PBS buffer (pH 7.4) is shown in Fig. 4-12a. The most noticeable difference between polyurea and SiN nanopores was the event frequency, plotted as a function of voltage (Fig. 4-12c). The MDM2 event frequency was 3.7, 4.3, and 6.4 events/s on the polyurea nanopore and 1.12, 1.20, and 1.43 events/s on the SiN nanopore at −100, −125, and −150 mV, respectively. Since the dimensions of SiN and polyurea pores were similar, these pores exhibited comparable electrophoretic field under the same applied voltage. Hence, the improved capture rate in the polyurea nanopore should be attributed to the drag by EOF (v_{EO}), exhibited by the higher surface charge density of polyurea (−51 mC/m^2) than of SiN (−14 mC/m^2). At the same applied voltage, the ratio of v_{EO} between polyurea and SiN nanopores ($v_{EO,PU}/v_{EO,SiN}$) in cis- chamber is 3.64. The event frequency of MDM2 on polyurea and SiN nanopores were linearly fitted with respect to the applied voltage, using $Frequency = A \times V$ (Fig. 4-12c), to investigate the relation between event frequency and v_{EO}. The fitting result of A was 38.81 and 9.93 for polyurea and SiN nanopores, respectively. We found that the ratio of A (A_{PU}/A_{SiN} = 3.91) was comparable to the ratio of v_{EO} (3.64). Together, the findings suggest that EOF is the primary source of MDM2 capture for nanopores. Therefore, we conclude that the high negative charge of polyurea nanopore induces high throughput MDM2 detection by EOF.

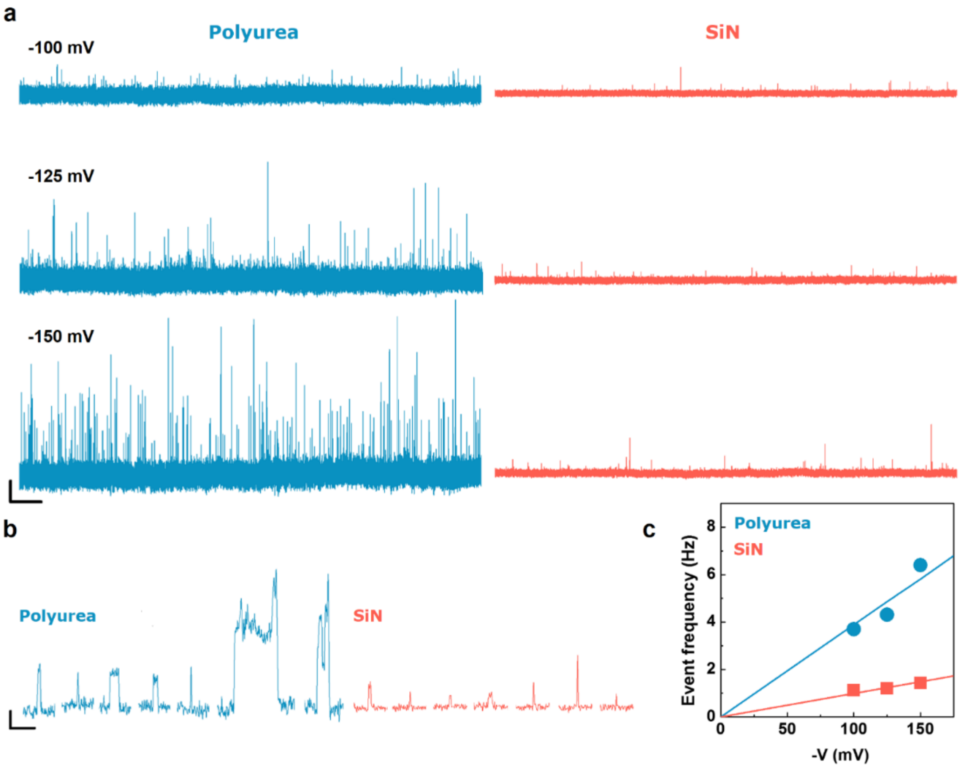

Figure 4-12 (a) Continuous 30-s ionic current traces for 100 nM MDM2 translocation at –100, –125, and –150 mV voltage through polyurea nanopore (Φ 10 nm, 8 nm thick) and SiN nanopore (Φ 9.5 nm, 9 nm thick) in buffered 1 M KCl (pH 7.4) (scale bar: 0.5 nA, 2 s). (b) Selected translocation events of MDM2 from (top) 150 mV current trace on SiN and polyurea pores (scale bar: 0.2 nA, 250 μs). (c) Event frequency versus voltage for SiN and polyurea pores. Each event frequency was fitted to y = Ax.

From the current traces, MDM2 translocation events were collected to extract the mean fractional current blockade ($\Delta I/I_0$) and the dwell time (t_D). The scatter plots for $\Delta I/I_0$ *vs* t_D with applied voltages of −100, −125, and −150 mV on SiN and polyurea nanopores for 5 min are summarized in Fig. 4-13a. The number of total events at each applied voltage for 5 min was 336 (−100 mV), 359 (−125 mV), and 428 (−150 mV) on SiN nanopore, and 1096 (−100 mV), 1301 (−125 mV), and 1928 (−150 mV) on polyurea nanopore, respectively. First of all, we observed a difference in dwell times between polyurea and SiN nanopores at all applied voltages. For instance, Fig. 4-13b shows the dwell-time (t_D) distribution for MDM2 both on polyurea and SiN nanopores and these data were fitted to a 1D drift diffusion model[67],

$$\mathrm{P(t)} = (h_{eff}/4\pi D_p t^3)^{1/2} e^{-(h_{eff}-v_d t)^2/4D_p t}$$

where h_{eff} is the effective pore thickness, D_{p} is the protein diffusion coefficient inside the pore, and v_{d} is the protein drift velocity during nanopore traversing. The extracted free parameters D_{p} and v_{d} for polyurea and SiN nanopores are shown in Fig. 4-14. We found slower v_{d} (0.36 ± 0.04 nm/μs) of MDM2 for polyurea nanopore than that (0.60±0.07 nm/μs) for SiN nanopore. The slower v_{d} for polyurea nanopore suggests that increase in EOF is not directly related to the translocation speed of biomolecules. Rather, this could be attributed to protein-pore interaction during translocation. We suspect that the higher surface charge density of the polyurea nanopore (−51 mC/m^2), compared to that of the SiN nanopore (-14 mC/m^2), would promote electrostatic interaction between the positively charged MDM2 and negatively charged pore surface. In addition, the calculated value of D_p (0.85 ± 0.23 nm^2/μs for polyurea nanopore and 1.51 ± 0.22 nm^2/μs for SiN nanopore) indicates an additional drag force acting on MDM2 when it is translocated through polyurea nanopore. A few studies had shown that DNA translocation through the nanopore is affected by the electrostatic interaction with positively charged surface, such as organically coated nanopores[11, 68], Al_2O_3 (points-of-zero-charge of pH 9.1)[69-70], ZnO nanopores (points-of-zero-charge of pH 9.1)[6], and positive-biased nanochannels[10, 71-72]. However, the effect of electrostatic interaction has not yet been studied in case of protein analytes, due to its fast translocation speed and heterogeneous charge profiles.[42, 73]

Fig. 4-14 shows the fractional current blockade ($\Delta I/I_0$) distribution for MDM2 both on polyurea and SiN nanopores and these histogram were fitted into the Gaussian distribution. The mean fractional current blockade shows 0.021 ± 0.002 for polyurea nanopore, and 0.015 ± 0.001 for SiN nanopore in the voltage range from -100 to -150 mV. With the fractional current blockade values and geometry of nanopore, hydrodynamic diameters of protein (d_H) was estimated by,[42, 74]

$$d_H = [(\Delta I/I_0)(h_{eff}+0.8d_p){d_p}^2]^{1/3}.$$

The obtained d_H of MDM2 is 3.23 ± 0.11 nm for polyurea nanopore, and

2.81 ± 0.03 nm for SiN nanopore. The x-ray crystallographic structure of MDM2 ($2.4\times2.6\times4.1$ nm^3) was provided by Protein Data Bank (PDB code: 1YCR), which shows the good correlation with the d_H for polyurea nanopore. The findings suggest that the polyurea nanopore successfully resolved the MDM2, and SiN nanopore could not sufficiently resolved the MDM2, due to fast translocation speed. Owing to their dimension controllability and unique high negative surface charge characteristics, polyurea nanopore is applicable to high-throughput detection with greater extent of slowing down of small proteins (< 20 kDa).

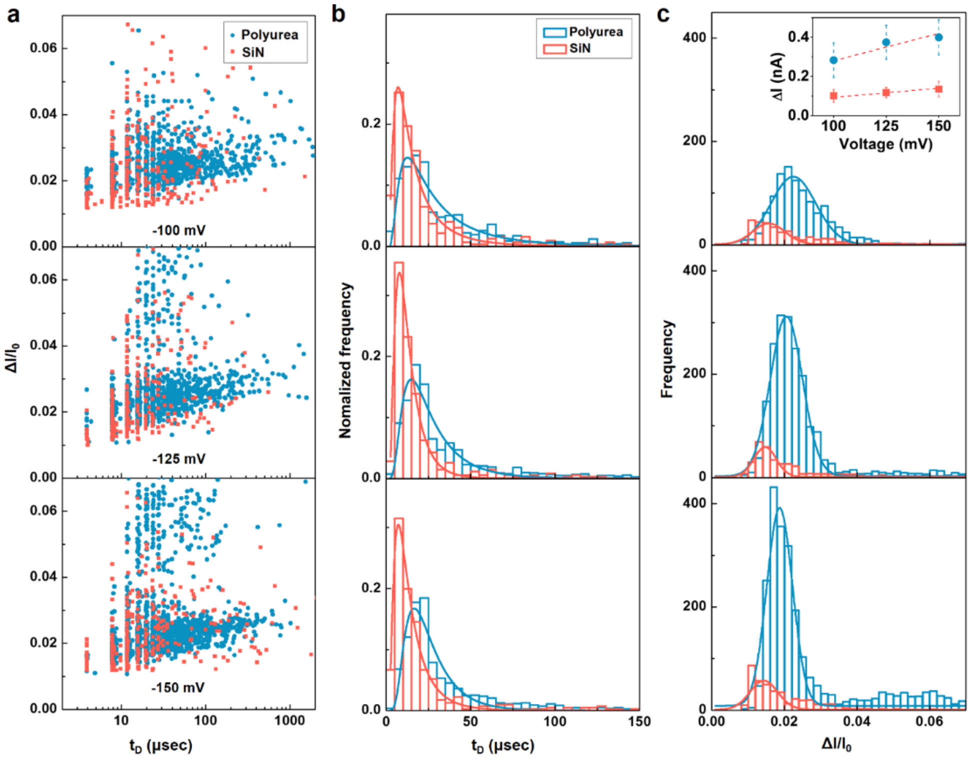

Figure 4-13 (a) Scatter plots of $\Delta I/I_0$ *vs* t_D for MDM2 translocation events over 5 min through polyurea and SiN nanopores in the range V = –100 to –150 mV. Due to the difference in translocation throughput, the number of total events at each applied voltage was 248 (–100 mV), 303 (–125 mV), and 347 (–150 mV) on SiN nanopore and 1096 (–100 mV), 1301 (–125 mV), and 1928 (–150 mV) on polyurea nanopore, respectively. (b) Histograms of t_D in the range V = –100 to –150 mV. The data were fitted to a 1D diffusion-drift model. (c) Histograms of $\Delta I/I_0$ in the range V = –100 to –150 mV. The data were fitted to Gaussian distribution. The inset shows the mean values of $\Delta I/I_0$ with respect to applied voltage. The dashed line represents the linear fit of data

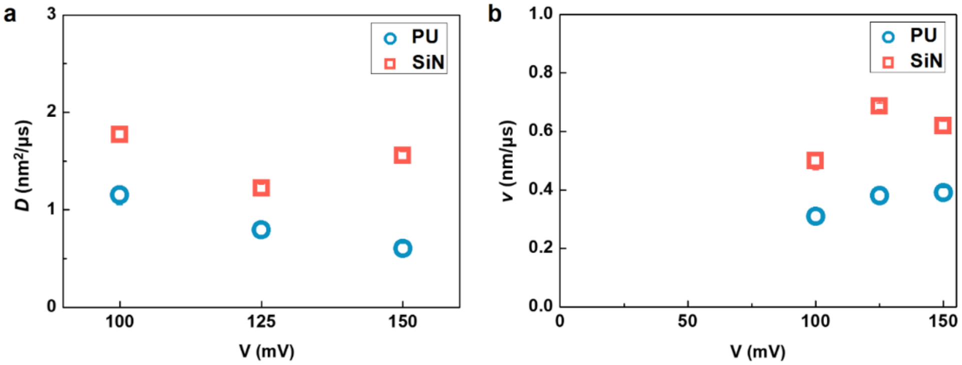

Figure 4-14 Diffusion coefficients (*D*) and drift velocities (*v*) for MDM2 transport through polyurea and SiN nanopore used in Fig. 4-13, obtained from fitting dwell times to 1D diffusion-drift model treating *D* and *v* as free parameters.

4.4 Summary

We have presented a process of fabricating polymer membrane on low-noise pyrex substrate using molecular layer deposition with controllable thickness, molecular composition, and orientation. This platform has potential application in the exploration of various biomolecule/polymer interfaces. We have demonstrated the formation of polyurea nanopores with 4–10 nm diameter and sub-10 nm thickness, using a TEM perforation method that induces a highly negative surface charge. We have shown that polyurea nanopores can successfully detect single-molecule translocation events of negatively charged dsDNA at a high ionic strength of 2.5 M KCl, as along with that of positively charged MDM2 protein. Comparing with SiN nanopore and by numerical analysis of EOF, we suggest that EOF suppresses the capture of negatively charged DNA and enhances the capture of positively charged MDM2. In addition, a longer dwell time of MDM2 in the polyurea nanopore, compared to that in the SiN nanopore, was observed as a result of electrostatic interaction. The polyurea nanopore exhibits an advantage of improved detection efficiency of positively charged proteins, in terms of event frequency and slow-down of molecular transport, relative to SiN nanopores. Further work will be to investigate the translocation of various analytes through polyurea nanopore and we expect to demonstrate the influence of the analytes' properties on their translocation.

References

1. Dekker, C., Solid-state nanopores. *Nature Nanotechnology* **2007,** *2*, 209.

2. Shi, W.; Friedman, A. K.; Baker, L. A., Nanopore Sensing. *Analytical Chemistry* **2017,** *89* (1), 157-188.

3. Wanunu, M., Nanopores: A journey towards DNA sequencing. *Physics of life reviews* **2012,** *9* (2), 125-158.

4. Schneider, G. F.; Dekker, C., DNA sequencing with nanopores. *Nature Biotechnology* **2012,** *30,* 326.

5. Branton, D.; Deamer, D. W.; Marziali, A.; Bayley, H.; Benner, S. A.; Butler, T.; Di Ventra, M.; Garaj, S.; Hibbs, A.; Huang, X.; Jovanovich, S. B.; Krstic, P. S.; Lindsay, S.; Ling, X. S.; Mastrangelo, C. H.; Meller, A.; Oliver, J. S.; Pershin, Y. V.; Ramsey, J. M.; Riehn, R.; Soni, G. V.; Tabard-Cossa, V.; Wanunu, M.; Wiggin, M.; Schloss, J. A., The potential and challenges of nanopore sequencing. *Nature Biotechnology* **2008,** *26*, 1146.

6. Park, K.-B.; Kim, H.-J.; Kang, Y.-H.; Yu, J.-S.; Chae, H.; Lee, K.; Kim, H.-M.; Kim, K.-B., Highly reliable and low-noise solid-state nanopores with an atomic layer deposited ZnO membrane on a quartz substrate. *Nanoscale* **2017,** *9* (47), 18772-18780.

7. Larkin, J.; Henley, R.; Bell, D. C.; Cohen-Karni, T.; Rosenstein, J. K.; Wanunu, M., Slow DNA Transport through Nanopores in Hafnium Oxide Membranes. *ACS Nano* **2013,** *7* (11), 10121-10128.

8. Banerjee, S.; Wilson, J.; Shim, J.; Shankla, M.; Corbin, E. A.; Aksimentiev, A.; Bashir, R., Slowing DNA Transport Using Graphene–DNA

Interactions. *Advanced Functional Materials* **2015,** *25* (6), 936-946.

9. Yusko, E. C.; Johnson, J. M.; Majd, S.; Prangkio, P.; Rollings, R. C.; Li, J.; Yang, J.; Mayer, M., Controlling protein translocation through nanopores with bio-inspired fluid walls. *Nat Nano* **2011,** *6* (4), 253-260.

10. Ren, R.; Zhang, Y.; Nadappuram, B. P.; Akpinar, B.; Klenerman, D.; Ivanov, A. P.; Edel, J. B.; Korchev, Y., Nanopore extended field-effect transistor for selective single-molecule biosensing. *Nature Communications* **2017,** *8* (1), 586.

11. Anderson, B. N.; Muthukumar, M.; Meller, A., pH Tuning of DNA Translocation Time through Organically Functionalized Nanopores. *ACS nano* **2013,** *7* (2), 1408-1414.

12. He, Y.; Tsutsui, M.; Fan, C.; Taniguchi, M.; Kawai, T., Gate Manipulation of DNA Capture into Nanopores. *ACS Nano* **2011,** *5* (10), 8391-8397.

13. Wong, C. T. A.; Muthukumar, M., Polymer capture by electro-osmotic flow of oppositely charged nanopores. *The Journal of Chemical Physics* **2007,** *126* (16), 164903.

14. Teles, F. R. R.; Fonseca, L. P., Applications of polymers for biomolecule immobilization in electrochemical biosensors. *Materials Science and Engineering: C* **2008,** *28* (8), 1530-1543.

15. Ahuja, T.; Mir, I. A.; Kumar, D.; Rajesh, Biomolecular immobilization on conducting polymers for biosensing applications. *Biomaterials* **2007,** *28* (5), 791-805.

16. Becker, H.; Locascio, L. E., Polymer microfluidic devices. *Talanta* **2002,** *56* (2), 267-287.

17. Wanunu, M.; Meller, A., Chemically Modified Solid-State Nanopores. *Nano Letters* **2007,** *7* (6), 1580-1585.

18. Shah, S., The nanomaterial toolkit for neuroengineering. *Nano Convergence* **2016,** *3* (1), 25.

19. Navya, P. N.; Daima, H. K., Rational engineering of physicochemical properties of nanomaterials for biomedical applications with nanotoxicological perspectives. *Nano Convergence* **2016,** *3* (1), 1.

20. Nagamune, T., Biomolecular engineering for nanobio/bionanotechnology. *Nano Convergence* **2017,** *4* (1), 9.

21. Harrell, C. C.; Siwy, Z. S.; Martin, C. R., Conical Nanopore Membranes: Controlling the Nanopore Shape. *Small* **2006,** *2* (2), 194-198.

22. Wu, S.; Park, S. R.; Ling, X. S., Lithography-Free Formation of Nanopores in Plastic Membranes Using Laser Heating. *Nano Letters* **2006,** *6* (11), 2571-2576.

23. Mara, A.; Siwy, Z.; Trautmann, C.; Wan, J.; Kamme, F., An Asymmetric Polymer Nanopore for Single Molecule Detection. *Nano Letters* **2004,** *4* (3), 497-501.

24. Liebes-Peer, Y.; Rapaport, H.; Ashkenasy, N., Amplification of Single Molecule Translocation Signal Using β-Strand Peptide Functionalized Nanopores. *ACS Nano* **2014,** *8* (7), 6822-6832.

25. Wang, D.; Harrer, S.; Luan, B.; Stolovitzky, G.; Peng, H.; Afzali-Ardakani, A., Regulating the transport of DNA through biofriendly nanochannels in a thin solid membrane. *Sci Rep* **2014,** *4*, 3985.

26. Kowalczyk, S. W.; Kapinos, L.; Blosser, T. R.; Magalhaes, T.; van

Nies, P.; LimRoderick, Y. H.; Dekker, C., Single-molecule transport across an individual biomimetic nuclear pore complex. *Nat Nano* **2011,** *6* (7), 433-438.

27. Yusko, E. C.; Prangkio, P.; Sept, D.; Rollings, R. C.; Li, J.; Mayer, M., Single-Particle Characterization of Aβ Oligomers in Solution. *ACS Nano* **2012,** *6* (7), 5909-5919.

28. Tang, Z.; Lu, B.; Zhao, Q.; Wang, J.; Luo, K.; Yu, D., Surface Modification of Solid-State Nanopores for Sticky-Free Translocation of Single-Stranded DNA. *Small* **2014,** *10* (21), 4332-4339.

29. Schneider, G. F.; Xu, Q.; Hage, S.; Luik, S.; Spoor, J. N. H.; Malladi, S.; Zandbergen, H.; Dekker, C., Tailoring the hydrophobicity of graphene for its use as nanopores for DNA translocation. *Nat Commun* **2013,** *4*.

30. Toader, G.; Rusen, E.; Teodorescu, M.; Diacon, A.; Stanescu, P. O.; Rotariu, T.; Rotariu, A., Novel polyurea polymers with enhanced mechanical properties. *Journal of Applied Polymer Science* **2016,** *133* (38).

31. Park, Y.-S.; Choi, S.-E.; Kim, H.; Lee, J. S., Fine-Tunable Absorption of Uniformly Aligned Polyurea Thin Films for Optical Filters Using Sequentially Self-Limited Molecular Layer Deposition. *ACS Applied Materials & Interfaces* **2016,** *8* (18), 11788-11795.

32. Park, Y.-S.; Kim, H.; Cho, B.; Lee, C.; Choi, S.-E.; Sung, M. M.; Lee, J. S., Intramolecular and Intermolecular Interactions in Hybrid Organic–Inorganic Alucone Films Grown by Molecular Layer Deposition. *ACS Applied Materials & Interfaces* **2016,** *8* (27), 17489-17498.

33. Choi, U.-J.; Kim, H.; Park, Y.-S.; Lee, H.; Lee, J. S., Molecular interaction-dependent surface potentials of sequentially polymerized alucone films. *Chemical Communications* **2018,** *54* (26), 3286-3289.

34. Lee, J. S.; Lee, Y.-J.; Tae, E. L.; Park, Y. S.; Yoon, K. B., Synthesis of Zeolite As Ordered Multicrystal Arrays. *Science* **2003,** *301* (5634), 818-821.

35. Abdulagatov, A. I.; Hall, R. A.; Sutherland, J. L.; Lee, B. H.; Cavanagh, A. S.; George, S. M., Molecular Layer Deposition of Titanicone Films using TiCl4 and Ethylene Glycol or Glycerol: Growth and Properties. *Chemistry of Materials* **2012,** *24* (15), 2854-2863.

36. Loscutoff, P. W.; Zhou, H.; Clendenning, S. B.; Bent, S. F., Formation of Organic Nanoscale Laminates and Blends by Molecular Layer Deposition. *ACS Nano* **2010,** *4* (1), 331-341.

37. Zhou, H.; Bent, S. F., Molecular Layer Deposition of Functional Thin Films for Advanced Lithographic Patterning. *ACS Applied Materials & Interfaces* **2011,** *3* (2), 505-511.

38. Abd, E. M.; Brigitte, V.; Bernd, B.; Klaus-Jochen, E.; Karina, G.; C., B., Structural and end-group effects on bulk and surface properties of hyperbranched poly(urea urethane)s. *Journal of Polymer Science Part A: Polymer Chemistry* **2005,** *43* (15), 3376-3393.

39. Firnkes, M.; Pedone, D.; Knezevic, J.; Döblinger, M.; Rant, U., Electrically Facilitated Translocations of Proteins through Silicon Nitride Nanopores: Conjoint and Competitive Action of Diffusion, Electrophoresis, and Electroosmosis. *Nano Letters* **2010,** *10* (6), 2162-2167.

40. Lee, M.-H.; Kumar, A.; Park, K.-B.; Cho, S.-Y.; Kim, H.-M.; Lim, M.-C.; Kim, Y.-R.; Kim, K.-B., A Low-Noise Solid-State Nanopore Platform Based on a Highly Insulating Substrate. *Scientific reports* **2014,** *4,* 7448.

41. Kwak, D.-K.; Chae, H.; Lee, M.-K.; Ha, J.-H.; Goyal, G.; Kim, M.

J.; Kim, K.-B.; Chi, S.-W., Probing the Small-Molecule Inhibition of an Anticancer Therapeutic Protein-Protein Interaction Using a Solid-State Nanopore. *Angewandte Chemie International Edition* **2016,** *55* (19), 5713-5717.

42. Waduge, P.; Hu, R.; Bandarkar, P.; Yamazaki, H.; Cressiot, B.; Zhao, Q.; Whitford, P. C.; Wanunu, M., Nanopore-Based Measurements of Protein Size, Fluctuations, and Conformational Changes. *ACS Nano* **2017,** *11* (6), 5706-5716.

43. Smeets, R. M. M.; Keyser, U. F.; Krapf, D.; Wu, M.-Y.; Dekker, N. H.; Dekker, C., Salt Dependence of Ion Transport and DNA Translocation through Solid-State Nanopores. *Nano Letters* **2006,** *6* (1), 89-95.

44. Di Fiori, N.; Squires, A.; Bar, D.; Gilboa, T.; Moustakas, T. D.; Meller, A., Optoelectronic control of surface charge and translocation dynamics in solid-state nanopores. *Nature nanotechnology* **2013,** *8* (12), 946-951.

45. Pitchford, W. H.; Kim, H.-J.; Ivanov, A. P.; Kim, H.-M.; Yu, J.-S.; Leatherbarrow, R. J.; Albrecht, T.; Kim, K.-B.; Edel, J. B., Synchronized Optical and Electronic Detection of Biomolecules Using a Low Noise Nanopore Platform. *ACS Nano* **2015,** *9* (2), 1740-1748.

46. Park, K.-B.; Kim, H.-J.; Kim, H.-M.; Han, S. A.; Lee, K. H.; Kim, S.-W.; Kim, K.-B., Noise and sensitivity characteristics of solid-state nanopores with a boron nitride 2-D membrane on a pyrex substrate. *Nanoscale* **2016,** *8* (10), 5755-5763.

47. Radenovic, A.; Trepagnier, E.; Csencsits, R.; Downing, K. H.; Liphardt, J., Fabrication of 10 nm diameter hydrocarbon nanopores. *Applied Physics Letters* **2008,** *93* (18), 183101.

48. Eric, B.; Harold, K.; Vincent, T.-C.; Michel, G., Precise control of the size and noise of solid-state nanopores using high electric fields. *Nanotechnology* **2012,** *23* (40), 405301.

49. Vincent, T.-C.; Dhruti, T.; Matthew, W.; Nahid, N. J.; Andre, M., Noise analysis and reduction in solid-state nanopores. *Nanotechnology* **2007,** *18* (30), 305505.

50. Ashvani, K.; Kyeong-Beom, P.; Hyun-Mi, K.; Ki-Bum, K., Noise and its reduction in graphene based nanopore devices. *Nanotechnology* **2013,** *24* (49), 495503.

51. Zhou, Z.; Hu, Y.; Wang, H.; Xu, Z.; Wang, W.; Bai, X.; Shan, X.; Lu, X., DNA Translocation through Hydrophilic Nanopore in Hexagonal Boron Nitride. *Scientific Reports* **2013,** *3*, 3287.

52. Garaj, S.; Liu, S.; Golovchenko, J. A.; Branton, D., Molecule-hugging graphene nanopores. *Proceedings of the National Academy of Sciences* **2013,** *110* (30), 12192.

53. Maglia, G.; Henricus, M.; Wyss, R.; Li, Q.; Cheley, S.; Bayley, H., DNA Strands from Denatured Duplexes are Translocated through Engineered Protein Nanopores at Alkaline pH. *Nano Letters* **2009,** *9* (11), 3831-3836.

54. Franceschini, L.; Brouns, T.; Willems, K.; Carlon, E.; Maglia, G., DNA Translocation through Nanopores at Physiological Ionic Strengths Requires Precise Nanoscale Engineering. *ACS Nano* **2016,** *10* (9), 8394-8402.

55. Maglia, G.; Restrepo, M. R.; Mikhailova, E.; Bayley, H., Enhanced translocation of single DNA molecules through α-hemolysin nanopores by manipulation of internal charge. *Proceedings of the National Academy of Sciences* **2008,** *105* (50), 19720.

56. Wanunu, M.; Morrison, W.; Rabin, Y.; Grosberg, A. Y.; Meller, A., Electrostatic focusing of unlabelled DNA into nanoscale pores using a salt gradient. *Nature Nanotechnology* **2009,** *5*, 160.

57. Franceschini, L.; Soskine, M.; Biesemans, A.; Maglia, G., A nanopore machine promotes the vectorial transport of DNA across membranes. *Nature Communications* **2013,** *4*, 2415.

58. Stefan, W. K.; Alexander, Y. G.; Yitzhak, R.; Cees, D., Modeling the conductance and DNA blockade of solid-state nanopores. *Nanotechnology* **2011,** *22* (31), 315101.

59. Stellwagen, N. C.; Gelfi, C.; Righetti, P. G., The free solution mobility of DNA. *Biopolymers* **1997,** *42* (6), 687-703.

60. Wanunu, M.; Morrison, W.; Rabin, Y.; Grosberg, A. Y.; Meller, A., Electrostatic focusing of unlabelled DNA into nanoscale pores using a salt gradient. *Nature nanotechnology* **2010,** *5* (2), 160-165.

61. Muthukumar, M., Theory of capture rate in polymer translocation. *The Journal of Chemical Physics* **2010,** *132* (19), 195101.

62. Bell, N. A. W.; Muthukumar, M.; Keyser, U. F., Translocation frequency of double-stranded DNA through a solid-state nanopore. *Physical review. E* **2016,** *93* (2), 022401-022401.

63. Restrepo-Perez, L.; John, S.; Aksimentiev, A.; Joo, C.; Dekker, C., SDS-assisted protein transport through solid-state nanopores. *Nanoscale* **2017,** *9* (32), 11685-11693.

64. Piguet, F.; Discala, F.; Breton, M.-F.; Pelta, J.; Bacri, L.; Oukhaled, A., Electroosmosis through α-Hemolysin That Depends on Alkali Cation Type. *The Journal of Physical Chemistry Letters* **2014,** *5* (24), 4362-4367.

65. Asandei, A.; Schiopu, I.; Chinappi, M.; Seo, C. H.; Park, Y.; Luchian, T., Electroosmotic Trap Against the Electrophoretic Force Near a Protein Nanopore Reveals Peptide Dynamics During Capture and Translocation. *ACS Applied Materials & Interfaces* **2016,** *8* (20), 13166-13179.

66. Boukhet, M.; Piguet, F.; Ouldali, H.; Pastoriza-Gallego, M.; Pelta, J.; Oukhaled, A., Probing driving forces in aerolysin and α-hemolysin biological nanopores: electrophoresis versus electroosmosis. *Nanoscale* **2016,** *8* (43), 18352-18359.

67. Talaga, D. S.; Li, J., Single-Molecule Protein Unfolding in Solid State Nanopores. *Journal of the American Chemical Society* **2009,** *131* (26), 9287-9297.

68. Kim, Y.-R.; Min, J.; Lee, I.-H.; Kim, S.; Kim, A.-G.; Kim, K.; Namkoong, K.; Ko, C., Nanopore sensor for fast label-free detection of short double-stranded DNAs. *Biosensors and Bioelectronics* **2007,** *22* (12), 2926-2931.

69. Venkatesan, B. M.; Shah, A. B.; Zuo, J.-M.; Bashir, R., DNA Sensing Using Nanocrystalline Surface-Enhanced Al2O3 Nanopore Sensors. *Advanced Functional Materials* **2010,** *20* (8), 1266-1275.

70. Venkatesan, B. M.; Dorvel, B.; Yemenicioglu, S.; Watkins, N.; Petrov, I.; Bashir, R., Highly Sensitive, Mechanically Stable Nanopore Sensors for DNA Analysis. *Advanced materials (Deerfield Beach, Fla.)* **2009,** *21* (27), 2771-2776.

71. Liu, Y.; Yobas, L., Slowing DNA Translocation in a Nanofluidic Field-Effect Transistor. *ACS Nano* **2016,** *10* (4), 3985-3994.

72. Tsutsui, M.; He, Y.; Furuhashi, M.; Rahong, S.; Taniguchi, M.; Kawai,

T., Transverse electric field dragging of DNA in a nanochannel. *Scientific reports* **2012,** *2*, 394.

73. Plesa, C.; Kowalczyk, S. W.; Zinsmeester, R.; Grosberg, A. Y.; Rabin, Y.; Dekker, C., Fast Translocation of Proteins through Solid State Nanopores. *Nano Letters* **2013,** *13* (2), 658-663.

74. Larkin, J.; Henley, R. Y.; Muthukumar, M.; Rosenstein, Jacob K.; Wanunu, M., High-Bandwidth Protein Analysis Using Solid-State Nanopores. *Biophysical Journal 106* (3), 696-704.

Chapter 5.

Summary and conclusion

Nanopore is an emerging technology for sensing the passage of molecules in aqueous solution, and controlling and optimizing the movement of molecules is a key issue. In this dissertation, the effect of surface charge characteristics of nanopores on the passage of molecules through electro-osmotic flow or electrostatic interaction has been studied, in order to optimize the movement of molecules.

In chapter 3, a study to increase the negative charge on silicon nitride nanopore by illuminating the laser beam has been conducted. For this purpose, we analyzed the origin of photo-induced noise in conventional Si substrate based nanopores, and showed the excellent noise characteristics of glass substrate based nanopores. In low noise nanopore platform, linearly increasing negative surface charge according to laser power was characterized. The photo-induced electro-osmotic flow in the direction opposite to the direction of the passage of DNA resulted in a 70 % reduction in DNA capture, whereas the translocation speed of DNA was not changed.

In chapter 4, we firstly proposed a polyurea nanopore by using the molecular layer deposition technique. The polyurea nanopore exhibits four times higher negative charge than conventional silicon nitride nanopore with a nanopore volume of few nanometers in all dimensions. We confirmed that dsDNA capture was inhibited by electro-osmotic flow in polyurea nanopore, and we could observed the dsDNA translocation through polyurea nanopore through reducing electro-osmotic flow by increasing the molar concentration. In case of translocation of mouse double minute 2 (MDM2) protein, which has opposite charge of DNA at pH 7.4, the capture rate was increased by the electro-osmotic flow with the same direction of electrophoretic force. The translocation speed was slowed down by the electrostatic interaction.

In our experiments, the effect of electro-osmotic flow on the capture of molecules into nanopores was well observed. This can be explained that the capture probability of molecule depends on the force balance between electro-osmotic and electrophoretic, and the other factor, such as diffusion, become minor around the nanopore. On the other hand, when the molecules pass through the nanopore, the effect of electro-osmotic flow seems to be hard to observe for the following reasons. 1) The electro-osmotic flow generated by dragging the fluid in the nanopore is not fully expressed as the internal space is blocked by the passing molecule. 2) In addition to electrophoretic and electro-osmotic, other drag forces act, for instances, surface friction force due to the interaction between molecule and pore wall, drag force from viscosity of solution, and stretched drag for long chain conformation of DNA. Indeed, the measured electrophoretic mobility of dsDNA was reported to be around 10^{-9} $m^2v^{-1}s^{-1}$, which was reduced by ~2 orders than that in the free solution. In particular, studies that attempt to slow the translocation speed by increasing the interaction between molecules and pore wall have shown meaningful outcomes in various directions: a) narrowing the pore diameter, b) electrostatic interaction, c) hydrophobic interaction, and d) specific binding affinity of biomolecules. Therefore, the use of nanopores that have charge opposite to that of biomolecules enables the efficient detection, in terms of event frequency and slowing down of molecule transport.

요약 (국문초록)

나노포어 센싱 기술은 생체분자가 나노포어를 통과할 때 발생하는 이온 흐름의 감소를 통해, 분자의 물리적인 크기나 전하 상태를 단분자 수준에서 분석하는 기술이다. 이러한 나노포어의 종류로는 구멍이 존재하는 구조의 단백질을 사용하는 바이올로지컬 나노포어와, 인위적으로 형성된 멤브레인에 구멍 구조를 형성하여 사용하는 솔리드 스테이트 나노포어가 있다. 바이올로지컬 나노포어는 1.4 nm 수준의 일정한 구멍 구조과 이로 인한 비교적 높은 감도를 바탕으로, 염기서열 분석 기술 분야에서 많은 주목을 받고 있다. 반면, 솔리드 스테이트 나노포어는 구멍의 크기와 구조를 조절할 수 있다는 점이나 멤브레인이 기계적 화학적으로 안정하다는 점을 바탕으로, 적용 가능한 분석물의 범위가 넓다는 장점을 보인다. 이에 다양한 종류의 생체분자들과 그 복합체들의 크기 검출을 통해 약물 스크리닝과 같은 생물학적인 의미를 가지는 응용분야에서 활용 가치가 높다. 현재 이러한 솔리드 스테이트 나노포어 기술을 발전시키기 위하여 감도 향상과 분자의 움직임 최적화 측면에서 많은 노력이 이루어지고 있다. 본 학위논문에서는 분자의 움직임 최적화를 위하여 나노포어의 표면전하 특성을 활용하고자 하였다. 표면전하 특성은 전기삼투유동이나 정전기적 간섭을 통해 분자의 움직임에 영향을 미치며, 이러한 관점에서 진행되었던 연구들을 제 2장에서 정리하였다. 또한, 표면전하를 조절하기 위하여 이 학위논문에서 활용된 접근 방식에 대하여 설명하였다.

제 3장에서는 실리콘 나이트라이드 나노포어에 레이저 빔을 조사함으로써 음전하를 유도하고, 레이저 파워의 조절에 따른 DNA의 움직임 변화를 관찰하였다. 음전하의 조절과 함께 생체분자의 통과를 고감도로 검출하기 위해서는, 보편적으로 사용되는 실리콘 기판

소자에서 보고되었된 레이저에 의한 전기적 잡음을 낮출 필요가 있었다. 이에 먼저 기존 실리콘 기판 소자와 유리 기판 소자의 잡음 특성 비교 분석을 통해, 잡음의 원인이 실리콘과 전해질의 계면에서 발생하는 수소의 환원반응임을 밝혀냈으며, 유리 기판 소자의 저잡음 특성을 발표하였다. 이후 유리기판 소자에서 레이저 파워에 따른 음전하의 증가를 이온 전류 측정을 통해 계산하였다. 증가된 음전하로 인해 DNA의 통과방향과 반대방향으로 발생하는 전기삼투유동은 DNA 포획 빈도를 감소시키는 반면, 통과 속도에는 영향을 주지 못했다. 또한, 저잡음 기판과 금속층이 결합된 멤브레인을 결합하여 플랫폼 소자를 개발하였고, 높은 신호대 잡음비로 생체분자의 전기적/광학적 동시 측정 결과를 보고하였다. 개발된 플랫폼 소자를 이용한 동시 측정은, 분자 움직임의 추가적인 확인이 가능하다는 점, 두 가지 측정 방법의 장점을 결합시킬 수 있다는 점에서 가치가 크다.

제 4장에서는 유기분자층을 층층이 기상 증착하는 분자층 증착법을 이용하여 강한 음전하를 띄는 폴리우레아 나노포어를 제작하고, DNA와 단백질의 통과 움직임을 관찰하였다. 폴리우레아 물질의 경우 기계적 안정성과 화학적 저항성을 갖추어, 전사 공정을 통하여 10 nm 이하 두께의 멤브레인 제작이 가능했고, 투과전자현미경을 이용하여 수 nm 수준에서 나노포어의 직경을 조절할 수 있었다. 폴리우레아 나노포어는 기존 실리콘 나이트라이드 나노포어와 비교하여 4배 이상의 강한 음전하 특성을 보였다. 이로 인해 발생한 강한 전기삼투유동은 음전하를 띄는 DNA의 전기영동 포획을 억제하였으며, 반대로 양전하를 띄는 MDM2 단백질의 전기영동 포획 빈도를 높였다. 제 3장에서의 DNA 측정결과와 마찬가지로, 전기삼투유동은 두 생체분자의 통과속도에는 영향을 주지 못했다. 오히려 정전기적 간섭으로 인해 폴리우레아 나노포어에서 MDM2의 통과속도가 늦춰지는 것을 확인하였다.

이 학위논문에서는 나노포어의 표면전하 특성이 생체분자의 움직임에

미치는 영향에 대해 논의하였다. 두 가지 방식의 접근을 통해 전기삼투유동이 생체분자의 나노포어 포획에 주된 구동력임을 밝혔으며, 단백질의 통과 속도를 정전기적 인력이 늦출 수 있음을 처음으로 보고하였다. 최종적으로, 분석물과 반대의 전하를 띄는 나노포어의 활용이, 첫째, 포획 빈도를 높여 분석 효율과 처리량을 증가시키고, 둘째, 통과속도를 늦추어 시간적 분해능 요구를 낮춤으로써, 검출 효율을 향상 시킬 수 있음을 제시하였다.

주요어: nanopore sensing, solid-state nanopore, single molecule sensing, surface charge, electro-osmotic flow, optical detection, polyurea

학번: 2012-24159

List of publications

Papers

- William H. Pitchford,# Hyung-Jun Kim,# Aleksandar P. Ivanov, Hyun-Mi Kim, Jae-Seok Yu, Robin J. Leatherbarrow, Tim Albrecht, Ki-Bum Kim, and Joshua B. Edel, “Synchronized optical and electronic detection of biomolecules using low noise nanopore platform”, *ACS NANO*, 2015, *9* (2): 1740–1748.

- Hyung-Jun Kim,# Ui-Jin Choi, # Hyein Kim, Kidan Lee, Kyeong-Beom Park, Hyun-Mi Kim, Dong-Kyu Kwak, Seung-Wook Chi, Jin Seok Lee, and Ki-Bum Kim, “Translocation of DNA and Protein through Sequentially Polymerized Polyurea Nanopore”, *Nanoscale*, DOI: 10.1039/c8nr06229c, 2018, (*inside front cover*)

- Hyung-Jun Kim, Kyeong-Bum Park, Jae-Hyun Kang, Kidan Lee, Hyun-Mi Kim, and Ki-Bum Kim, “Detection of metal corrosion characteristics in chlorine solution using solid-state nanopore”, (*Under revision on Nanotechnology)*

- Jae-Seok Yu,# Min-Cheol Lim,# Duyen Huynh, Hyung-Jun Kim, Hyun-Mi Kim, Young-Rok Kim, and Ki-Bum Kim, “Identifying the Location of a Single Protein along the DNA Strand Using Solid-State Nanopores”, *ACS NANO*, 2015, 9 (5): 5289–5298

- Kyeong-Beom Park, Hyung-Jun Kim, Hyun-Mi Kim, Sang A. Han, Kang Hyuck Lee, Sang-Woo Kim, and Ki-Bum Kim, “Noise and sensitivity characteristics of solid-state nanopores with a boron nitride

2-D membrane on a pyrex substrate", *Nanoscale*, 2016. 8(10): 5755-5763.

- Colin Crick, Albella Pablo, Hyung-Jun Kim , Aleksandar Ivanov , Ki-Bum Kim , Stefan Maier and Joshua Edel, "Low-noise Plasmonic Nanopore Biosensors for Single Molecule Detection at Elevated Temperatures", *ACS Photonics*, 2017, 4: 2835-3842

- Kyeong-Bum Park, Hyung-Jun Kim, Yun-Ho Kang, Jae-Seok Yu, Hongsik Chae, Kidan Lee, Hyun-Mi Kim, and Ki-Bum Kim, "Highly reliable and low-noise solid-state nanopores with an atomic layer deposited ZnO membrane on a quartz substrate", *Nanoscale*, 2017. 9: 187772-18780

- Kidan Lee, Kyeong-Beom Park, Hyung-Jun Kim, Jae-Seok Yu, Hongsik Chae, Hyun-Mi Kim, and Ki-Bum Kim, "Recent Progress in Solid-State Nanopores", *Adv. Mater.*, 2018. 1704680

Patents

- 김기범, 유재석, 김형준, 나노포어 구조체, 나노포어 구조를 이용한 이온소자 및 나노멤브레인 구조체 제조방법, 대한민국, 10-2015-0094159 (PCT/KR2015/007399),
- Ki-Bum Kim, Jae-Seok Yu, Hyung-Jun Kim, NANOPORE STRUCTURE, IONIC DEVICE USING NANOPORE STRUCTURE AND METHOD OF MANUFACTURING NANOMEMBRANE STRUCTURE,

  US20170138925A1 / EP3305722A1 / WO2017003006A1

Conferences

- Hyung-Jun Kim, Nanofluidic diode through gold nanoparticles trapped into the conical nanochannel system, Nano Korea, (2013)
- Kyeong Beom Park, Ashvani Kumar, Hyungjun Kim, Hyun-Mi Kim, Ki-Bum Kim, "h-Born Nitride Nanopore Treated by Flicker Noise Reduction Process for High Signal to Noise Ratio" 2014 Materials Research Society spring meeting (MRS), (2014, USA)
- Hyung-Jun Kim, Synchronized optical and electronic detection of biomolecules using a low noise nanopore platform, Nano Korea, (2015)
- Hyung-Jun Kim, Light induced ionic noise in Si and Pyrex based solid-state nanopore device, ENGE, (2014)

- Hyung-Jun Kim, William H. Pitchford, Kyeong-Beom Park, Hyun-Mi Kim, Joshua B. Edel, Ki-Bum Kim, Photo-induced ionic noise in Si and pyrex based solid-state nanopore device, 230th ECS meating (2016, USA)

- Hyung-Jun Kim, Ui-Jin Choi, Hyein Kim, Kyeong-Beom Park, Hyun-Mi Kim, and Jin Seok Lee, Ki-Bum Kim, Chemical functionalization of solid state nanopores using molecular layer deposition, 648th WE-Heraeus-Seminar (2017, Germany)